Molten-Lithium/Water Interaction Experiments: Explosive Reactions and Reaction Rate Measurements

S.W. Lomperski

May 1991

UWFDM-851

Ph.D. thesis.

FUSION TECHNOLOGY INSTITUTE

UNIVERSITY OF WISCONSIN

MADISON WISCONSIN

Molten-Lithium/Water Interaction Experiments: Explosive Reactions and Reaction Rate Measurements

S.W. Lomperski

Fusion Technology Institute
University of Wisconsin
1500 Engineering Drive
Madison, WI 53706

http://fti.neep.wisc.edu

May 1991

UWFDM-851

Ph.D. thesis.

MOLTEN-LITHIUM/WATER INTERACTION EXPERIMENTS: EXPLOSIVE REACTIONS AND REACTION RATE MEASUREMENTS

by

STEPHEN W. LOMPERSKI

Under the Supervision of

MICHAEL L. CORRADINI

A thesis submitted in partial fulfillment of the

requirements for the degree of

Doctor of Philosophy

Nuclear Engineering and Engineering Physics

at the

UNIVERSITY OF WISCONSIN-MADISON

1991

ABSTRACT

The interaction of molten lithium droplets with water has been studied through experiments and mathematical modeling. The experiments were divided into two test series. The first involved injecting a molten lithium droplet into the bottom of a reaction vessel filled with water, and making qualitative observations of the reaction. The drop diameter was approximately 10 mm, and initial metal temperature ranged from 200 C to 500 C. Water temperature was varied between 20 C and 70 C. It was found that when reactant temperatures are high, an explosive reaction often occurs. When the initial lithium temperature is above 400 C and the water is above 30 C, the explosive reactions become much more probable. Pressures at the reaction vessel wall were measured during these violent reactions, and peaks were as high as 4 MPa.

The second test series was used to make rate measurements of the lithium/water reaction. These were measurements of nonexplosive reactions. The reaction geometry paralleled that of the first test series. Measured reaction rates ranged from about 10 to 40 moles/s m^2. The experimental data did not show any significant variation in the reaction rate as a function of either water or initial lithium temperature.

In addition to these experiments, a mathematical model of the lithium/water reaction was developed to examine and explain experimental findings. Through this model, it was learned that chemical energy released by the lithium/water reaction is capable of heating the metal droplet surface to its saturation temperature in less than one-half second. Results of parametric tests with this model strongly suggested that this vaporization is responsible for the explosive reactions observed in the first test series.

ACKNOWLEDGEMENT

I would like to convey my thanks to Professor Corradini, who encouraged me throughout this work and expressed faith in my abilities despite some early setbacks in the experiments. Thanks to Sol Walsh, who machined most of the components designed for the experiment. Also, I appreciate the assistance and suggestions I received from Jim Barry, Ilpo Huhtiniemi, Bill Hamilton, and Joe Krueger. Most notably, I wish to thank Joe for all his help and advice. Many of the ideas that made this experimental work a success are attributed to him.

Thanks also to Lee Cadwallader and Steve Piet, who took the time to proof-read an early draft of this work. I gratefully acknowledge the financial support of the DOE Office of Fusion Energy and the EG&G Fusion Safety Program.

Finally, a special thanks to the Madison Fire Department, and its unique contribution to the completion of this work.

CONTENTS

List of Figures

Nomenclature

a = Absorption coefficient (m^{-1})

A = Area of radiating body (m^2)

b = Pyrometer calibration constant

Bo= Bond number

c = Heat capacity (J/g C)

$\mathbf{C_1}$= Radiation constant ($1.19x10^8$W $um^4m^{-2}sr^{-1}$)

$\mathbf{C_2}$= Radiation constant ($1.44x10^4$um K)

d = Lithium drop diameter (m)

$\mathbf{D_{vg}}$=Diffusion coefficient of hydrogen in water vapor (m^2/s)

E = Heat of Reaction (J/g-mole)

f = Signal frequency (Hz)

F = Fraction of radiation falling on active detector area

Fo= Fourier number

$\mathbf{g_o}$= Gravitational acceleration (980. m/s^2)

G = Mass transfer coefficient (m/s) [Chpt. 4]

G = Gain of amplification and filtering circuitry (volts/amp) [Chpt. 5]

h = Heat transfer coefficient (W/m^2)

$\mathbf{h_{fv}}$= Heat of vaporization of Water (J/g C)

i = Spectral intensity (W/m^2 um sr)

$\mathbf{i_{fv}}$=Heat of vaporization for water (J/g)

J = Molar flux (g-moles/m^2 s)

k = Thermal conductivity (W/m C)

K = Reaction rate (moles Li/m^2s)

m = Slope of line in calibration of pyrometer in water

M = Molecular weight (g/g-mole)

N = Moles of gas [Chpt. 4] **or** Number of data samples [Chpt. 5]

n = Total molar concentration (g-moles/m^3)

Nu= Nusselt number (**hd/k**)

P = Pressure (N/m^2)

Pr= Prandtl number ($\mathbf{c_p u/k}$)

Q = Power (Watts)

r = Radial distance from drop center (m) [Chpt. 4]

r = Path length between a point on the radiating source and a point on the input to the fiber optic cable (m) [Chpt. 5]

R = Radius of lithium drop (m) [Chpt. 4]

R = Photodiode response (amps/watt) [Chpt. 5]

$\Re$ = Gas Constant (8.31 J/g-mole K) [Chpt. 4]

$\Re$ = Ratio of output voltages from two pyrometer channels [Chpt. 5]

Re= Reynolds number (ρ**vd/u**)

Sc= Schmidt number (**u/D**ρ)

T = Temperature (K)

v = Velocity (m/s)

V = Lithium drop volume (ml) [Chpt. 4] **or** Signal output (volts) [Chpt. 5]

x = Distance between lithium drop and fiber optic cable input (m) [Chpt. 5]

x = Molar concentration fraction [Chpt. 4]

z = Spatial coordinate perpendicular to metal surface

GREEK

ρ = Density (g/ml)

δ = Film thickness; Diffusion layer thickness (m)

α = Thermal diffusivity (m^2/s)

θ = Time (s)

u = Viscosity (g/m s)

ε = Emissivity

λ = Radiation wavelength (um)

ϖ = Solid angle

σ = Stefan-Boltzmann Constant [Chpt. 4] **or** Measurement uncertainty [Chpt. 5]

τ = Combined transmittance of acrylic window, fiber optic cable, and narrow band pass filter

Ψ = Calibrated instrument constant

ξ = Residual in regression equation

Δ = Change or difference

SUBSCRIPTS / SUPERSCRIPTS

b = Black body or y-intercept of regression equation

f = Liquid water

g = Hydrogen gas

i = Film/Water interface [Chpt. 3] **or** Pyrometer channel number [Chpt. 4] **or** i'th data point [Chpt. 5]

j = Time step index [Chpt. 3] **or** Pyrometer channel number [Chpt. 4]

k = nodal mesh point

m = metal

t = Total, combined

o = Evaluate parameter at 273 K

v = Water vapor

s = Surface of lithium drop

y = Exponent for temperature distribution

I INTRODUCTION

Fusion reactors that derive their power from a deuterium-tritium reaction must produce their own tritium if they are to be economically feasible. It has been determined that bombarding lithium with neutrons is the most practical way to breed tritium in a power reactor. Consequently, lithium must be included in the reactor design in one form or another and it is found that, generally, lithium is incorporated into the reactor as a 'breeding blanket' layer and/or primary coolant. In the early stages of fusion research, lithium was extensively studied as a reactor coolant and breeder [1,2]. Currently, a wide variety of materials are under consideration to serve as the reactor blanket and coolant in conceptual fusion energy devices. Materials that are solid at reactor operating temperatures, such as Li_2O and $LiAlO_2$, could serve as breeders while liquids such as $Li_{17}Pb_{83}$ and pure lithium could play the role of both breeder and coolant [3,4]. One of the fusion community's latest conceptual design efforts, the TIBER II reactor design, utilizes water as a coolant with a lithium salt such as $LiNO_3$ or LiOH dissolved in the water for breeding tritium [5].

Choosing the best blanket material is difficult because of the various characteristics it must possess. The material must: **a)** provide adequate tritium breeding and recovery, **b)** be compatible with other reactor materials, **c)** be economically competitive, and **d)** not cause undue safety and reliability problems. Liquid lithium is promising because of its excellent heat-transfer characteristics, good breeding capability, and the likelihood of maintaining low tritium inventories by continuously processing the flowing lithium [6,7].

Detailed studies of the relative merits of various blanket materials have been performed previously [3,7,8].

Despite the numerous benefits of using lithium as a coolant and blanket material, there remains a reluctance to incorporate it into fusion reactor designs because of its great chemical reactivity. In particular, lithium creates safety concerns in designs which intend to incorporate both liquid lithium and water [7,8]. During the course of a reactor accident, the integrity of structures intended to keep these materials separated may be compromised. Considerable equipment damage could result because the lithium/water reaction is highly exothermic and is expected to be self-sustaining. In addition, hydrogen generated by the reaction may prove to be a safety hazard due to combustion with oxygen, or from system over-pressures due to the hydrogen production alone. Only a thorough understanding of lithium/water reactions will enable one to better predict the consequences of such a mishap, and prevent its likelihood by improved designs.

It may be mentioned that interest in lithium/water reactions can be found outside the fusion community. Lithium rates favorably as a high performance propellant in underwater vehicles, e.g. torpedoes, and it is found in certain aerospace alloys. In one propellant system, lithium is preheated and then pumped into a combustion chamber where it is mixed with seawater [9]. Since the oxidizer is taken from the environment rather than carried along, lithium makes an efficient fuel. Tests with both lithium and sodium have been conducted by using small rocket-motor test cells [10]. Lithium and sodium were compared in a performance study which involved thermodynamic calculations on the reactions of the metals with water. It was found that the lithium system produced five times as much energy per pound as the sodium system. Though

alkali metal propellants have some inherent disadvantages, it was felt that systems demanding low specific fuel consumption could make use of lithium as a water-reactive fuel.

In many ways, lithium is an ideal coolant for high temperature systems. It is a liquid over a wide temperature range (melting point at 180 C, boiling point at 1347 C) and has a low vapor pressure so that high temperature systems need not be operated at high pressure. Furthermore, the large thermal conductivity and heat capacity of lithium make it a very efficient coolant. These factors alone have made lithium a prime candidate for high performance space-nuclear power systems [11]. For a fusion reactor system, the appeal of lithium stems from its ability to produce tritium. Neutrons produced by fusion reactions in the plasma travel through the blanket where they may combine with lithium, creating helium and tritium:

$$Li^6 + n \Rightarrow He^4 + T$$

Tritium is removed from the blanket, combined with deuterium, and then used as additional fuel for the plasma.

The physical properties and breeding ability of lithium combine to make it a nearly ideal coolant and blanket material for a fusion device. Unfortunately, lithium is similar to the other alkali metals in that it is quite chemically reactive. When lithium is in the molten state it is extremely corrosive and reacts with all molecular gases [12]. Molten lithium attacks most metals, largely due to impurities in the lithium or containment material. Refractory metals are seen to be the most likely candidates for a containment material in a lithium system though compatibility is highly dependent upon specific system conditions such as lithium purity, flow-rate, and treatment of the alloy [12]. When

reacting with water, lithium produces hydrogen and more energy per gram of metal than any of the other alkali metals [13]. Because of this last point, lithium/water reactions are being investigated so that the safety of new reactor designs may be better evaluated.

There is a vast body of literature pertaining to molten metal/water reactions. This is largely due to a longstanding concern over vapor explosions in the metal industry [14,15] and, more recently, it has been suggested that it may be possible for a large vapor explosion to occur during the course of a nuclear reactor accident [16]. In a severe loss of coolant accident (LOCA), cooling water in the reactor core may be lost because of structural failure in the pressure vessel. If the water is not replenished, decay heat and metal-water reactions in the fuel rods begin to boil off the remaining coolant. Portions of the core could melt, possibly falling into the remaining pool of water. The sudden combination of molten metal and water may result in a vapor explosion, which has the potential to do further damage to the reactor vessel.

For the most part, these metal/water reaction studies focus on the mechanisms which transfer heat from the hot metal to a more volatile coolant, usually water. If the molten metal can cool fast enough, generating a large amount of steam in a brief period, a rapid heat transfer event or vapor explosion may occur. This physical explosion is distinctly different from a chemical explosion. The thermal energy, rather than chemical energy, of the system is converted into destructive work [14]. Because most of the studies pertain to somewhat inert metals, or metals that generate a small amount of energy when oxidized, chemical reaction of the metal with water is regarded as a relatively unimportant process in most vapor explosions. It will become apparent that this is not the case for a lithium/water reaction.

When lithium comes into contact with water, heat is generated by one or more of the following reactions [12]:

$$Li_{(c)} + H_2O_{(l)} \Rightarrow LiOH_{(c)} + .5\ H_{2(g)} \quad \textbf{- 0.20 MJ/Mole Li} \quad (1.1)$$

$$2Li_{(c)} + H_2O_{(l)} \Rightarrow Li_2O_{(c)} + H_2 \quad \textbf{- 0.16 MJ/Mole Li} \quad (1.2)$$

$$Li_{(c)} + LiOH_{(c)} \Rightarrow Li_2O_{(c)} + .5\ H_{2(g)} \quad \textbf{- 0.11 MJ/Mole Li} \quad (1.3)$$

$$Li_{(c)} + .5\ H_{2(g)} \Rightarrow LiH_{(c)} \quad \textbf{- 0.09 MJ/Mole Li} \quad (1.4)$$

These heats of reaction were evaluated at 25 C. It should be noted that the last reaction reverses when LiH reaches its dissociation temperature of 997 C [17]. If this temperature is attained, it is possible for a sudden, profuse generation of hydrogen gas to occur which, in a closed system, may be destructive. It is for this reason that reactor designers are reluctant to incorporate lithium-to-water heat exchangers in conceptual fusion reactor designs [17].

The difference in character between the conventional metal/water reaction and a lithium/water reaction may be seen by comparing the chemical and thermal energy released from a molten lithium droplet reacting in water. When lithium metal is in the presence of excess water, Equation 1.1 is the dominant reaction [18]. Only one lithium atom is required for the first reaction while the second needs two lithium atoms to proceed. If any Li_2O forms, the excess water generates the following reaction:

$$Li_2O_{(c)} + H_2O_{(l)} \Rightarrow 2\ LiOH_{(c)} \quad \textbf{- 0.069 MJ/Mole } Li_2O \quad (1.5)$$

where the heat of reaction of the above equation has been evaluated at 25 C. Using the heat of reaction from Equation 1.1, it is computed that one gram of lithium produces about 28 kJ of energy. This can be compared with the thermal energy released when one gram of lithium is cooled from 600 C to room temperature. This temperature is chosen because it is an approximate upper bound to expected lithium temperatures when used as a fusion reactor coolant. The energy released, about 2.6 kJ, is less than ten percent of the chemical energy available from the lithium/water reaction. It is evident that the chemical reaction has a great potential for energy release.

Vigorous exothermic chemical reaction coupled with hydrogen generation makes lithium-water reactions somewhat different from the standard metal-water reaction. The purpose of this study is to more carefully characterize the rate of molten lithium/water reactions as an aid to safety studies concerned with the use of liquid lithium. A more complete understanding of the lithium/water reaction is necessary before lithium metal is put into service in a fusion power reactor.

II PREVIOUS INVESTIGATIONS

Relatively few experiments have been performed with molten lithium and water. The first portion of this section is devoted to these past experiments. This is followed by a review of investigations with solid lithium and water. These experiments identified reaction mechanisms, rates, and products of the lithium/water reaction under a variety of conditions. The findings add insight into the chemistry of the reactions, which is not found in experiments with molten lithium. The review also includes investigations of sodium/water reactions; the physical and chemical similarities between lithium and sodium suggest that reaction mechanisms of one may be applicable to the other. Moreover, some studies with sodium parallel the experiments to be conducted with lithium and water. Also included in this section is an examination of zirconium/water interaction experiments and a study of the fragmentation of molten-metal jets in water. Though the study of metal jets does not include chemical reactions, the observed physical phenomena are pertinent to the lithium/water experiments.

II.I Molten-Lithium/Water Experiments

The most pertinent experiments that have been performed are those of Finn, et al. [19] with lithium and lithium-lead alloys. Each sample of metal was heated in an inert atmosphere furnace and then dropped into a tank of water while a high speed camera recorded the reaction. The tank of water was open to the atmosphere during each experiment. The initial conditions of each experiment and a brief characterization of the reactions are listed in Figure 2.1. For case 7, the lithium was dropped onto the water

Case	Sample Composition	State[a]	Temp (K)	Water Temp (K)	Reaction
1	Li_7Pb_2	s	773	298	Modest
2	Li_7Pb_2	s	773	369	Vigorous
3	Li_7Pb_2	s	873	368	Vigorous
4	Li_7Pb_2	l	1103	368	Very Vigorous
5	$Li_{62}Pb_{38}$	l	773	368	Vigorous
6	$Li_{17}Pb_{83}$	l	773	368	Very Modest
7	Li	l	773	368	H_2 Detonation
8	Li[b]	l	773	368	Detonation

a) s = solid, l = liquid

b) injected under water

Figure 2.1

Reactions of Li-Pb Alloys and Lithium With Water [19].

surface. The lithium floated on top of the water, reacting vigorously, and after 1.8 s, an explosion resulted, producing a pressure spike of 0.27 MPa. In case 8, an injector was used to force the lithium below the water surface. A pressure spike of over 2 MPa was recorded 513 ms after the injection, and the water tank was destroyed. Following these tests, there was some disagreement as to whether the pressure spikes were caused by rapid production of hydrogen or ignition of the hydrogen and atmospheric oxygen [20]. To resolve this question, another test was performed with the injector, though this time an argon cover was maintained above the water. Again, an explosion resulted, and it is estimated that about 2.5 ml of lithium was injected before the explosion occurred [20].

Jeppson and Keogh [21] have completed experiments in which prospective blanket materials were added to excess water in open containers (initial scoping tests) and closed containers (for quantitative measurements of the reaction). The scoping tests consisted of dropping a liner filled with blanket material at 600 C into 300 ml of water at 98 C. The water and blanket material were in an argon atmosphere. Some parameters and observations of these tests are given in Figure 2.2. The descriptions of interactions indicate that reactions of lithium and lithium-lead appeared to be the most exothermic. The lithium-lead eutectics, which contain larger percentages of lithium, were found to react more vigorously. The Li_7Pb_2 alloys became red hot during the reaction and generated steam, hydrogen, and a black aerosol. The lithium samples also generated steam and hydrogen but they glowed white hot and released a white aerosol.

To make quantitative comparisons among blanket/water reactions, it was necessary to perform tests in a closed system. The new tests consisted of filling the same liner used in scoping tests with blanket material (.9 g of Li, 10 g of Li_7Pb_2, and 26 g of $Li_{17}Pb_{83}$) and

Test Material	Mass (g)	Interaction	Aerosol Observed
Empty Liner	-	Rapid boiling (2 sec)	None
Sand	5	Rapid boiling	None
Li_2ZrO_2	5	Rapid boiling (3 sec)	None
$LiAlO_2$	5	Rapid boiling (3 sec)	None
Li_2SiO_3	5	Slower boiling (4 sec) powder floated on surface	None
Li_2O	5*	Boiling for 3 min. then slowed down	None
$Li_{17}Pb_{83}$	20	8 sec Rapid off-gassing then 1 min. slow reaction	None
Li_7Pb_2	2	Crimson glowing underwater with some sparking for about 5 sec	Black aerosol emitted
Li_7Pb_2	6	" " "	" "
Li	0.15	Bright glowing mass under water**	White aerosol
Li	0.4	" " "	" "

* Formed sintered solid on heating
** Lithium remained in liner

Figure 2.2

Scoping Tests for the Addition of Blanket Material to Water [21].

dropping it into four liters of water under an argon atmosphere. The blanket material and water were again at 600 C and 98 C, respectively. The water temperature and vessel pressure were monitored during the reaction and results with lithium-lead alloys and lithium are shown in Figure 2.3. It can be seen that even though the lithium sample was much smaller than either of the lithium-lead samples, the peak pressure generated by lithium was the greatest of all three tests. From this plot, it is observed that the lithium has reacted completely after about 30 seconds. Considering how reactive molten lithium is expected to be, this may seem peculiar. However, it should be noted that the lithium remained within the liner (which was at the bottom of the beaker of water) during the reaction so that only a limited amount of surface area was available for reaction.

Further tests were conducted in which water was added to excess blanket material within an enclosed system using argon as a cover gas. For these tests, the initial blanket and water temperatures were the same as in the previously described tests. The apparatus used for these tests consisted of a water injector mounted on top of a cylinder, above a heated pool of blanket material. An 8.8 liter chamber was attached to permit the collection of gaseous reaction products. Additional parameters for each test and results are tabulated in Figure 2.4. It was found that the lithium metal reached its peak temperature faster than any of the other blanket materials, in about ten seconds, and that the peak temperature was highest for lithium.

Medium scale lithium/steam reaction tests have been performed in the Liquid Metal Fire Facility at HEDL [22]. These tests were intended to characterize the interaction of steam with lithium in a configuration that portrays a potential system failure. A schematic of the reaction vessel is provided in Figure 2.5. Steam was forced through a

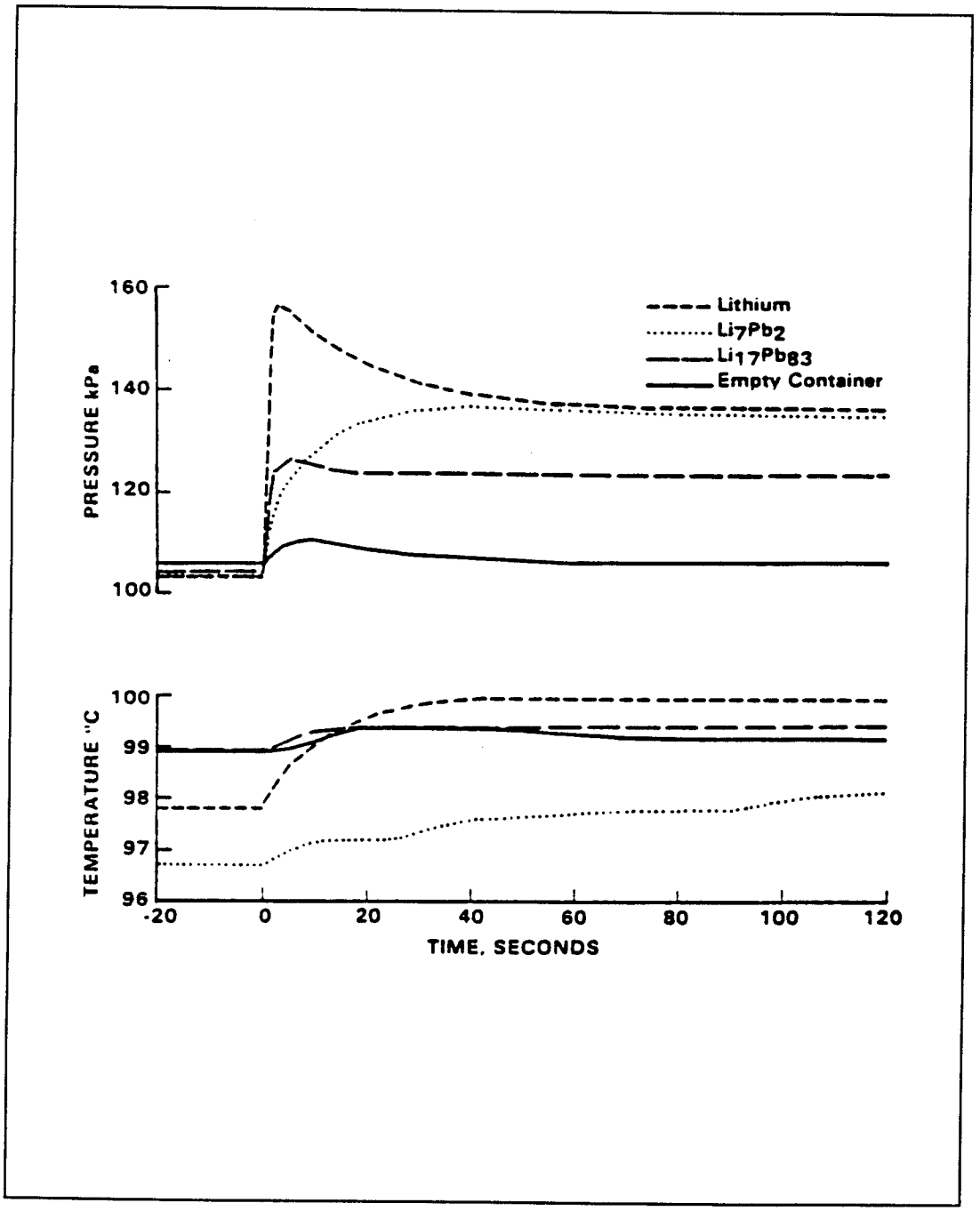

Figure 2.3

Water Temperature and Vessel Atmosphere for

Lithium and Lithium-Lead Alloy Addition to Water [21]

Blanket Material	Mass Water/ Mass Blanket	Peak Temp.	Gas Released Moles/ Mole H_2O	H_2 Released Moles/ Mole H_2O	Time to Peak Temp.
$LiAlO_2$	3.3/3.1 g/g	600 C	1.0	0	--
Li_2ZrO_3	3.1/50	600	1.0	0	--
Li_2SiO_3	3.0/50	600	1.0	0	--
Li_2O	3.0/50	625	0.275	0	50 s
Li_7Pb_2	2.8/40	770	0.8	0.13	20
$Li_{17}Pb_{83}$	3.0/50	630	0.8	0.09	60
Li	3.0/20	900	0.37	0.16	10

Figure 2.4

Test Results for the Addition of Water to

Blanket Material in an Enclosed System [21].

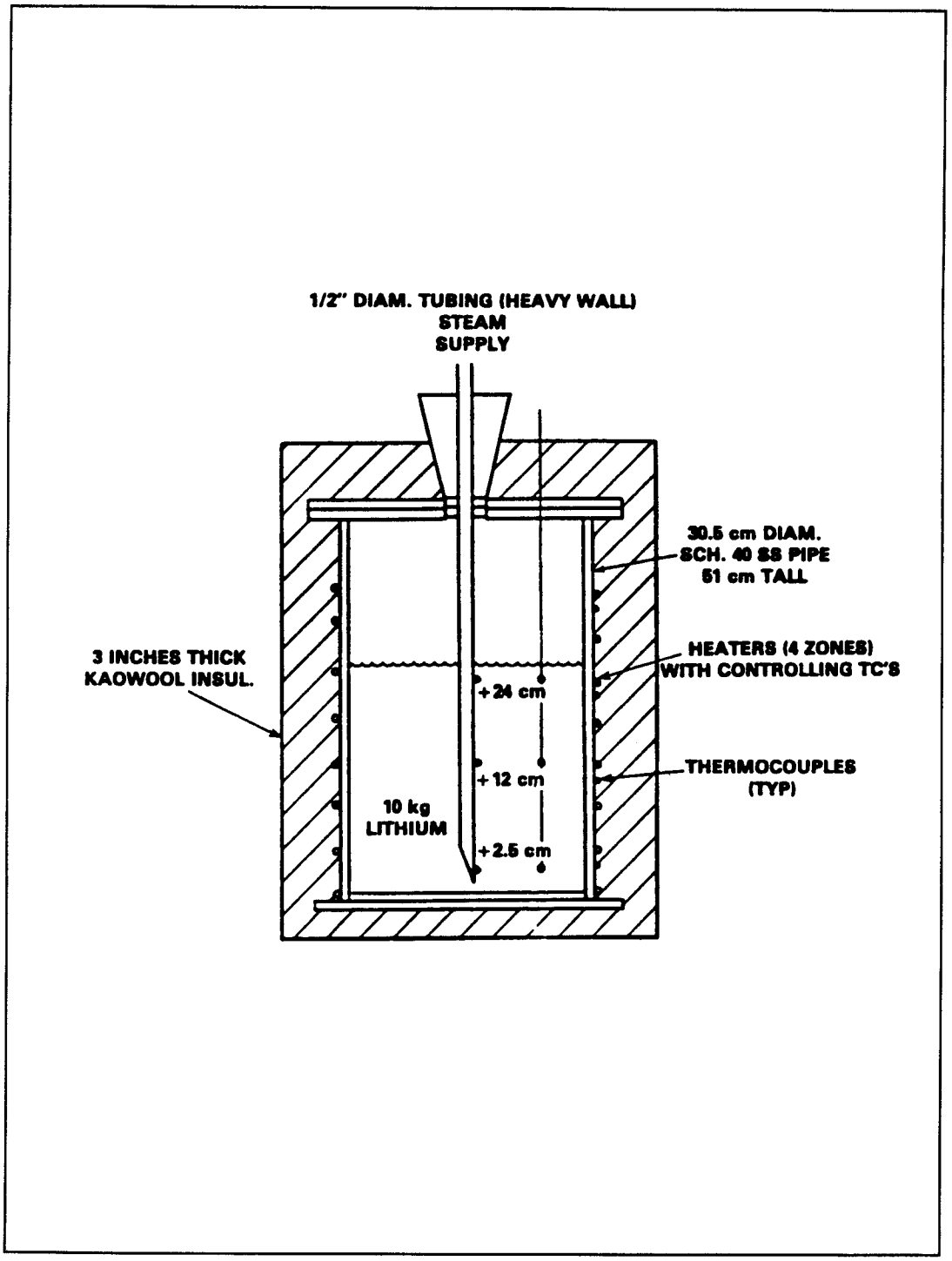

Figure 2.5

Reaction Vessel for Steam Injection into Lithium Pool [22]

12.7 mm (1/2") diameter pipe which extends nearly to the bottom of the reaction vessel. Temperature was monitored with three thermocouples along the centerline of the vessel and three that were 100 mm off the centerline. An argon atmosphere was maintained within the reaction vessel to prevent the reaction of lithium and hydrogen with air.

The first test involved the injection of superheated steam at 320 C into a pool of lithium at 580 C. The steam was injected at 2.6 g/s and the pool consisted of 10 kg of lithium. Figure 2.6 shows the lithium pool temperatures at the vessel centerline during the course of steam injection. The temperature at the point of steam injection was higher than at other points in the vessel, sometimes by as much as 100 C. Steam injection was discontinued when pool temperatures approached 1000 C to avoid containment corrosion, volatilization of reaction products, and the dissociation of lithium hydride. Subsequent chemical analysis of the pool determined the reaction products to be lithium monoxide and lithium hydride. Lithium hydroxide formation was suppressed because the reaction took place in the presence of excess lithium. In addition, it was found that the reaction released 124 kcal of energy per g-mole of water consumed.

The Massachusetts Institute of Technology is involved in research of lithium/water and lithium/gas reactions that is closely related to the previously outlined studies [23]. Barnett and Kazimi have investigated the kinetics of lithium reactions with mixtures of oxygen, nitrogen, and steam for various gas compositions and lithium temperatures. The gas mixtures were created by combining gases in a four liter tank, which was heated and insulated to maintain the proper temperature and prevent steam condensation. A controlled flow of this gas mixture passed over a pool of lithium, which had been heated in a stainless steel combustion chamber. The pool was about 15 mm deep, 100 mm long,

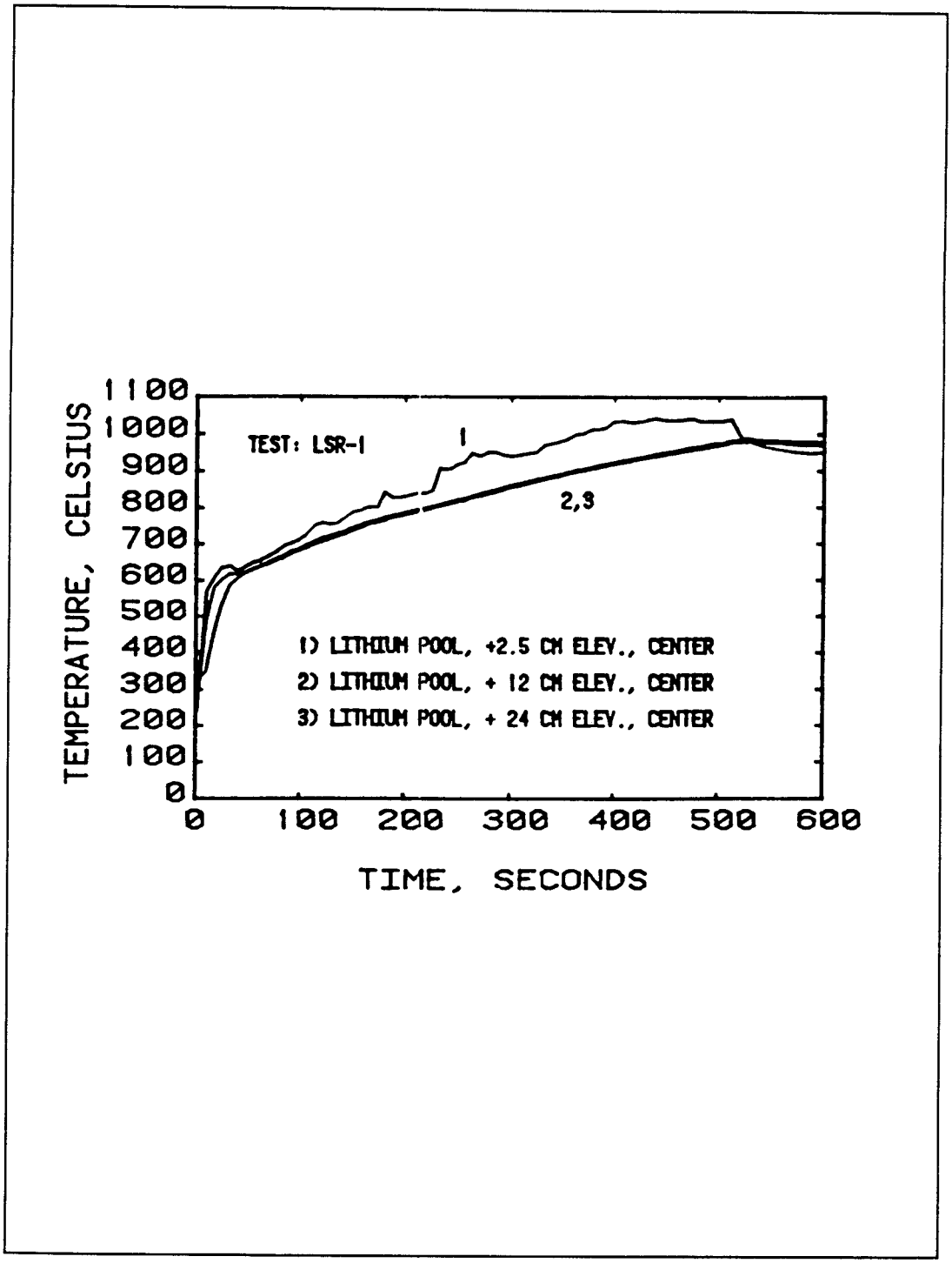

Figure 2.6

Pool Temperatures at Reaction Vessel Centerline [22]

and 20 mm wide. The gas flow continued through the combustion chamber and, after being filtered to remove aerosol reaction products, was collected in a second tank. The gas in this tank was analyzed at the end of each test to determine the new composition so that reaction rates may be calculated. Numerous experiments were carried out with varying fractions of oxygen, nitrogen, and steam, in addition to different lithium temperatures. Figure 2.7a shows the reaction rate of lithium and nitrogen with varying amounts of steam in the gas mixture. The reaction rate with 15% steam increased with lithium temperature, but seems to be approximately constant for 5% and 30% steam.

Test results also showed that reaction rates in the presence of steam were higher than for dry nitrogen and that this effect increased as the lithium temperature was decreased. The test results that demonstrate this effect are shown in Figure 2.7b. Overall, the fraction of steam in the gas seemed to have very little effect on the reaction rate for the fractions studied.

Experiments that measure the reaction rate of lithium and pure steam would be of more interest for comparison with the experimental results of this study, given in chapter 5. We are unaware, though, of any studies of this nature.

The final study to be reviewed in this section is a small scale experiment designed to investigate the kinetics of lithium-lead/water reactions [24,25]. The study was conducted at the University of Wisconsin as part of the same program in fusion reactor blanket technology that prompts this investigation of lithium/water reactions. The goal of these experiments was to quantify the reaction rate when water comes in contact with a particular eutectic of lithium-lead ($Li_{17}Pb_{83}$). The apparatus shown in Figure 2.8 was designed and constructed to achieve this goal. In essence, the device dropped one liter

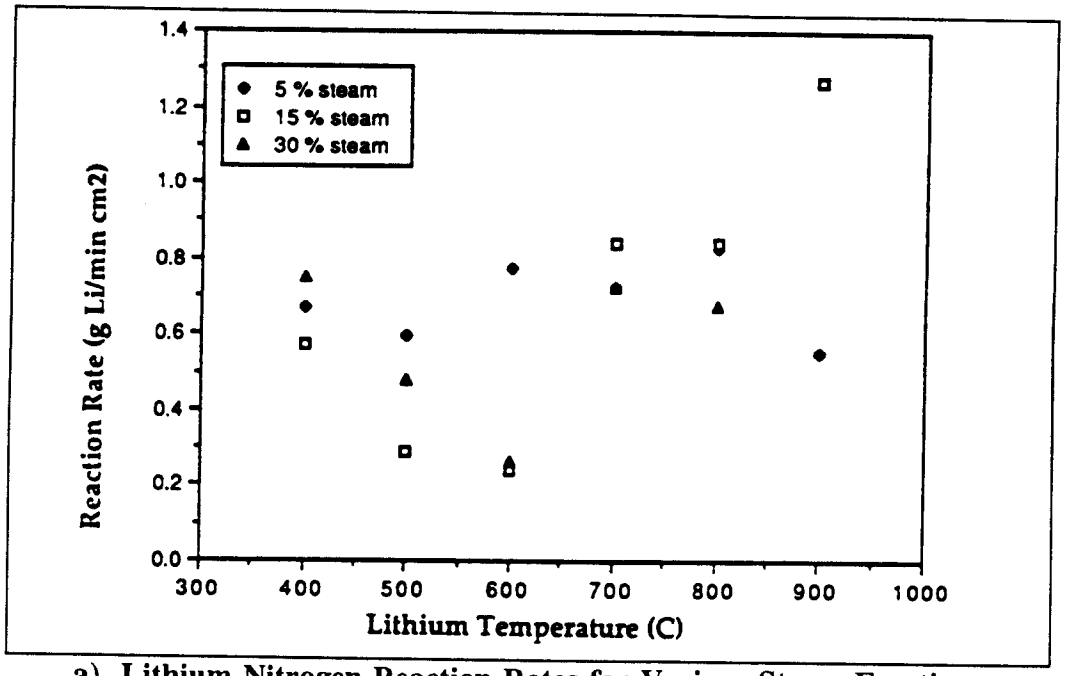

a) Lithium-Nitrogen Reaction Rates for Various Steam Fractions

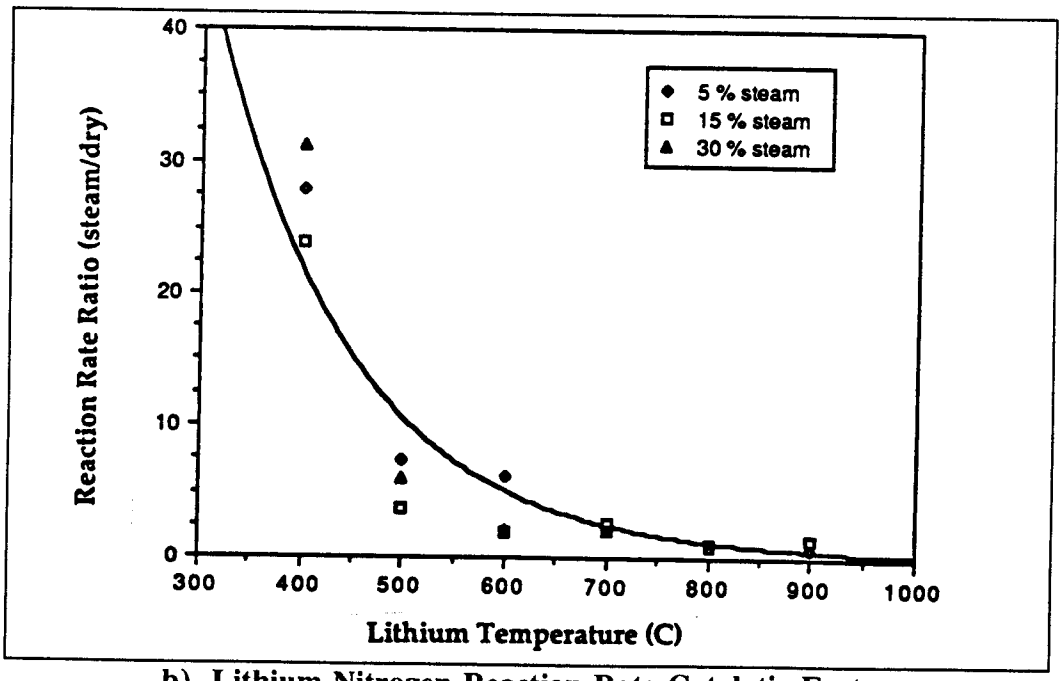

b) Lithium-Nitrogen Reaction Rate Catalytic Factor

Figure 2.7

Lithium-Nitrogen Reaction Rate Data [23]

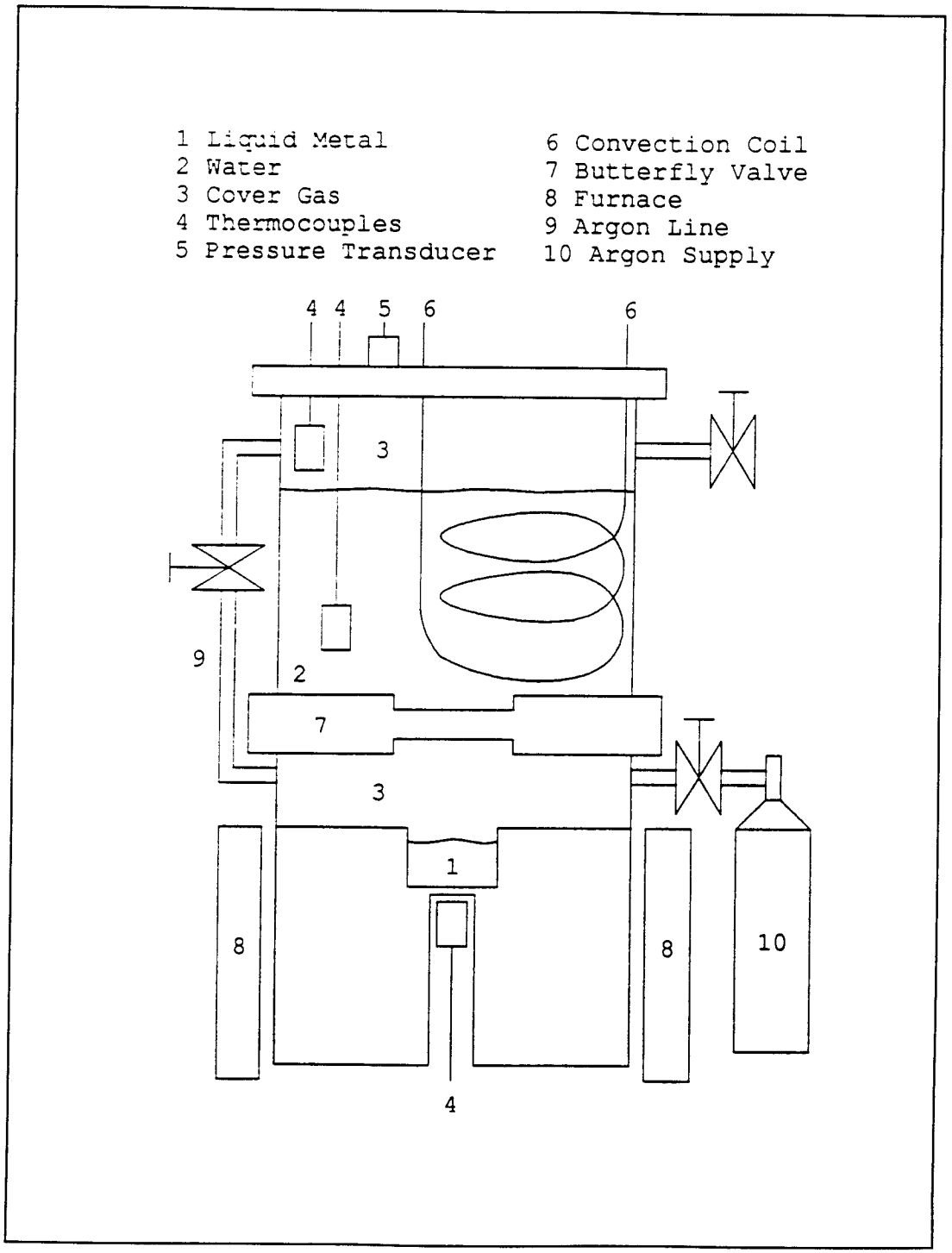

Figure 2.8

Schematic for Lithium-Lead/Water Kinetics Experiments [24]

of heated water onto a 25 mm diameter by 32 mm deep pool of molten lithium-lead. The reaction took place in a closed volume so that the pressure increase during the reaction would be used to indicate hydrogen and steam production as a function of time. The water was held in a length of steel pipe and its temperature was controlled by pumping water through a hollow copper convection coil. Water in the coil did not mix with water that was to be dropped on the molten metal. The lithium/lead sat in a well was drilled into a solid steel cylinder. This cylinder fit into an annular, electrically heated furnace, which was capable of raising the metal temperature to 600 C.

During the heating process, the separation between water and lithium-lead was maintained with a stainless steel butterfly valve. When the desired conditions were achieved, the butterfly valve was manually opened and the water dropped down onto the pool of molten metal. A number of thermocouples were positioned so that temperatures of the metal, water, and gas layer above the water could be measured. In addition, a pressure transducer measured static pressure in the gas layer.

After opening the butterfly valve to release the water and initiate the reaction, it took some 100-150 seconds to establish liquid-vapor equilibrium in the gas layer. Equilibrium is necessary to calculate the hydrogen produced and so it was found that hydrogen production as a function of time could not, in fact, be determined. Alternatively, results of the experiment were viewed in terms of the extent of reaction after 200 seconds, a period long enough to ensure equilibrium and an essentially completed reaction. These results, shown in Figure 2.9, include the original findings given in reference [24] as well as subsequent findings, which were made after some slight modifications to the original apparatus [25]. The early data suggested that the extent of

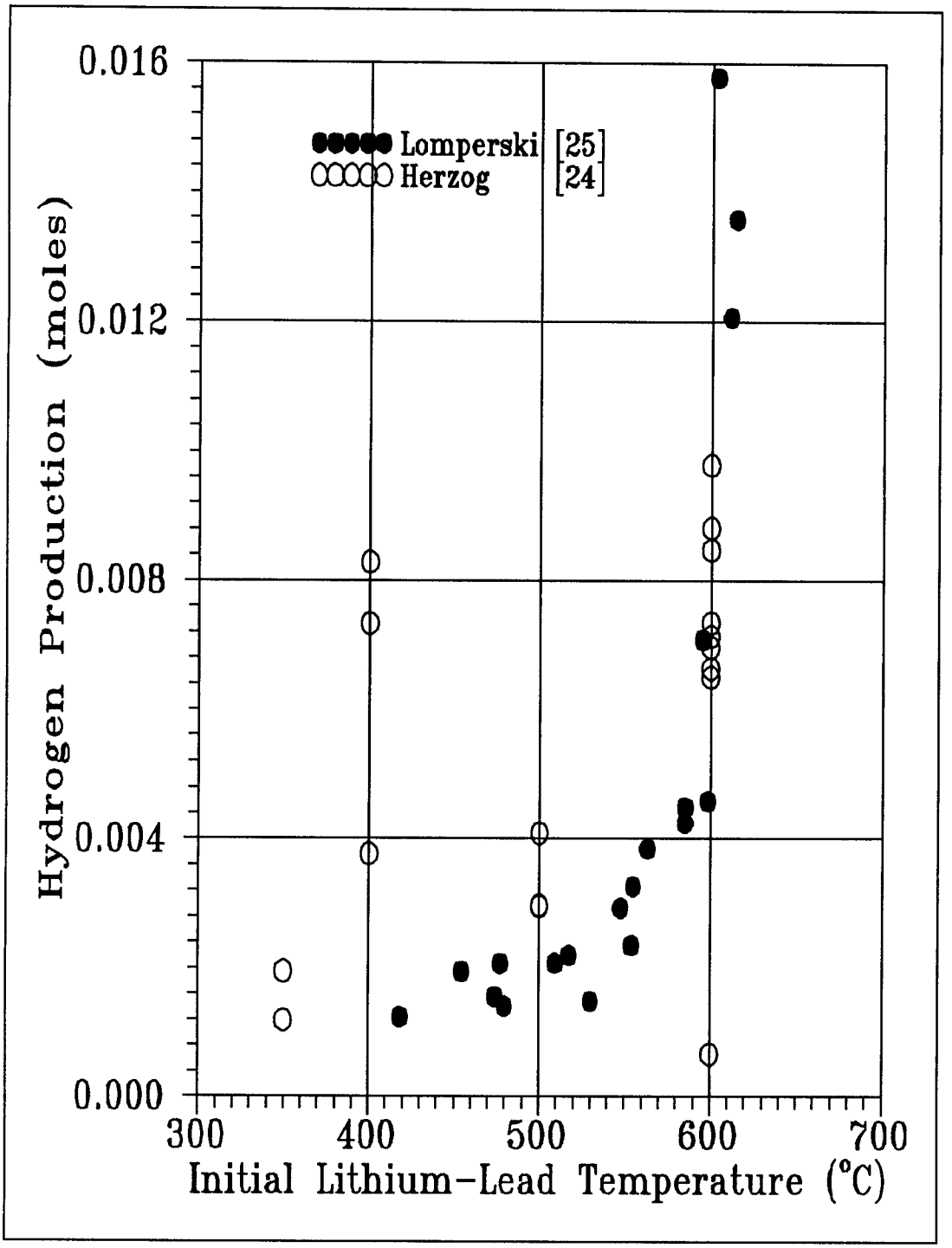

Figure 2.9

Hydrogen Production at 200 seconds versus Initial Lithium-Lead Temperature [24,25]

reaction may have a maximum in the initial lithium temperature range of 350 C to 500 C. The succeeding tests, indicated by filled circles in Figure 2.9, were unable to replicate this and, instead, showed a clear trend of greater extent of reaction as the initial temperature of the lithium-lead was increased. The difference might be attributed to difficulties encountered by Lomperski in ensuring that the metal was melted before initiation of the reaction when initial metal temperatures were below 400 C. A number of tests with initial metal temperatures near or below 400 C were thrown out (considered to be failed tests) because, upon disassembly of the apparatus, it was found that the lithium-lead had melted partially or not at all. It is unclear whether this was caused by the presence of impurities in the test sample, or if a portion of the sample was a eutectic other than $Li_{17}Pb_{83}$, which has the lowest melting point of all the lithium-lead eutectics. Thus it was not possible to compare the results of Herzog and Lomperski for initial metal temperatures below about 400 C. Finally, it is noted that in Herzog's original work, hydrogen production was not found to be a function of initial water temperature.

II.II Early Solid Lithium/Water Experiments

The chemical reactivity of lithium was studied long before fusion reactor designs were envisioned. However, experimenters did not generally concern themselves with reactions involving molten lithium. Instead, these early experiments involved solid lithium and were intended to identify the reaction products of a lithium/water reaction along with their production rate. This section details investigations in which samples of solid lithium were exposed to water and steam.

An early experiment by Deal and Svec [26] measured the reaction rate of water

vapor with lithium by suspending a cylinder of pure lithium within a reaction vessel and monitoring the pressure change as a function of time. Soon after water vapor was introduced into the reaction vessel, a glossy black coating appeared on the metal. This coating then slowly changed to a white material. Analysis suggested that both coatings were lithium hydroxide.

Deal and Svec found that the reaction rate data fit a logarithmic rate law. In general, the reaction rate increased with water vapor pressure and temperature, though it was independent of pressure when the vapor pressure was below 50 mm Hg. Tests were performed with vapor pressures as low as 20 mm Hg, but no lower limit to this pressure independence was found.

Ten years later, Lund and Irvine [27] reexamined lithium/water vapor reactions by observing the weight change of thin lithium wafers. X-ray diffraction analysis indicated that the glossy black coating observed by Deal and Svec was indeed lithium hydroxide but that the white coating was actually lithium hydroxide monohydrate ($LiOH{\cdot}H_2O$). These findings, along with reaction rate data, suggested a multi-step reaction mechanism. Initially, the lithium reacts with water vapor to form a thin lithium hydroxide coating, which acts as a protective layer. This hydroxide layer then becomes hydrated (there is some question as to whether the hydration occurs along with initial formation of the hydroxide layer) so that two separate layers of reaction products exist. At this point in the reaction, the rate is determined by transport processes through the two reaction product films. Water vapor must find its way through a porous layer of $LiOH{\cdot}H_2O$ and then diffuse across the LiOH layer before coming in contact with pure metal.

Meyer Markowitz studied lithium/water reactions by introducing solid pieces of

lithium to water under a variety of conditions [13]. It was found that irregularly shaped pieces of lithium retain their original shape while reacting in water. This is because the melting point of lithium is above that of water and the heat sink provided by the surrounding liquid is sufficient to prevent melting. Data from preliminary kinetics studies with lithium spheres (in 25 C water under argon) produced the following integrated rate law :

$$r(t) = r_0 - .0036\ t \qquad (2.1)$$

Where **r** is the sphere radius in centimeters and **t** is the time in seconds. Unfortunately, the author did not supply details on the experiments used to obtain this rate law or the conditions under which this relation may be used.

Markowitz also studied a different type of lithium reaction by placing samples in flowing steam [13]. Soon after exposure to the steam, a white coating of LiOH, $LiOH{\cdot}H_2O$, and possibly some Li_2O covers the sample. The coating begins to glow after about five minutes and liquid lithium flows through cracks on the surface. The liquid lithium burns brightly as it begins to react with steam. Markowitz explained that the hydroxide coating acts as an insulator so that heat from the reaction melts the sample. As the reaction proceeds the coating thickens and cracks. The hydroxide coating retains enough of the heat of reaction so that the lithium reaches the ignition temperature and an alkali metal-steam flame develops.

The same study notes that lithium need not be molten to be highly reactive. If the surface-to-volume ratio of the lithium substantially increases, the lithium reactivity also increases. This point is illustrated by an experiment that places a gelatin capsule, filled with a lithium dispersion, into a flask of water. The atmosphere within the capsule and

flask is argon, and the average lithium particle size is 22 microns. The gelatin capsule is placed in water under an argon atmosphere and after the capsule dissolves, flames can be seen under the water. Hot hydrogen gas was seen to ignite near the mouth of the flask as it mixed with air.

The previous studies demonstrate the great reactivity of lithium in water. Under the proper conditions, the reactions of both solid and molten lithium with water generate enough heat to produce flames. Though we see that the reactivity of lithium increases with exposed surface area, the previous studies give no certain indication of when the chemical reaction may become explosive in nature. Jeppson has suggested that an explosion resulting from the chemical reaction of molten lithium is not possible even if a dispersion mechanism exists to increase the exposed surface area [12]. To achieve a violent chemical reaction, it is more important for each atom of the reacting metal to quickly displace two hydrogen atoms from the water molecule. Lithium displaces only one hydrogen atom with lithium hydroxide forming from the remainder of the water molecule, and so the hydrogen production rate is limited. Thus it was suggested that the chemical reaction alone should not be able to generate high, explosive pressures.

Since only a few lithium/water experiments relevant to the above discussion have been performed, it is worthwhile to examine related experiments with sodium and water. A number of these experiments explore the (sometimes) explosive nature of alkali-metal/water reactions.

II.III Sodium/Water Experiments

One might expect similarities in the behavior of lithium and sodium since they are both alkali metals, and so some information may be garnered from looking at studies of sodium/water reactions. One such study was performed by Newman, et al. [28] who placed samples of solid sodium, weighing between 2 and 15 grams, inside a wire mesh cage that was subsequently lowered into cold water. A thermocouple was embedded in the sodium sample, and a microphone beside the water container monitored the explosion. Figure 2.10 shows the experimental arrangement, and Figure 2.11 gives a typical response for the thermocouple and microphone. Note that they used both sheathed and unsheathed thermocouples. The majority of these tests resulted in an explosion shortly after the sodium was lowered into the water. Peak temperatures measured by the unsheathed thermocouple during the explosion were nearly 1000 C.

In these tests, a delay between immersion of the wire cage and the explosion was always observed. During this time, the sample bubbled vigorously, producing smoke and flashes of light. For samples over 4 grams, the delay time averaged about 4 seconds. For smaller samples, there was either no explosion or very long delays, upwards of 20 seconds. When the explosion occurred, there was a more prominent flash of light that extended several centimeters from the cage. The most intense light emission was found to be outside the cage, away from the sodium sample.

Newman, et al. performed another series of experiments with similar conditions except that the water was at 95 C [28]. They found that no explosions occurred though the rate of hydrogen generation increased. From these results, they postulated that a dispersion mechanism was necessary for an explosive production of hydrogen and steam.

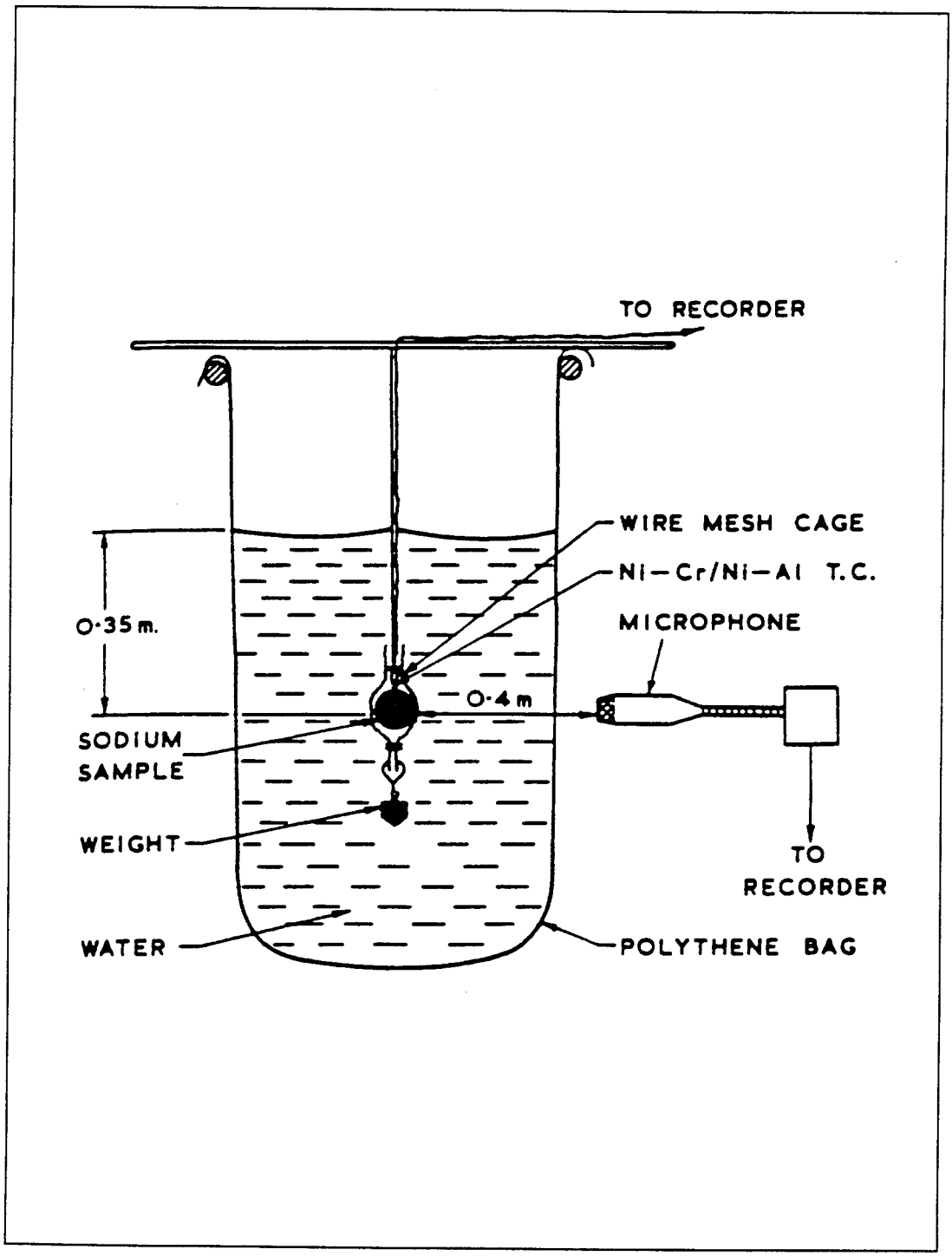

Figure 2.10

Apparatus for Small Scale Sodium/Water Experiment [28]

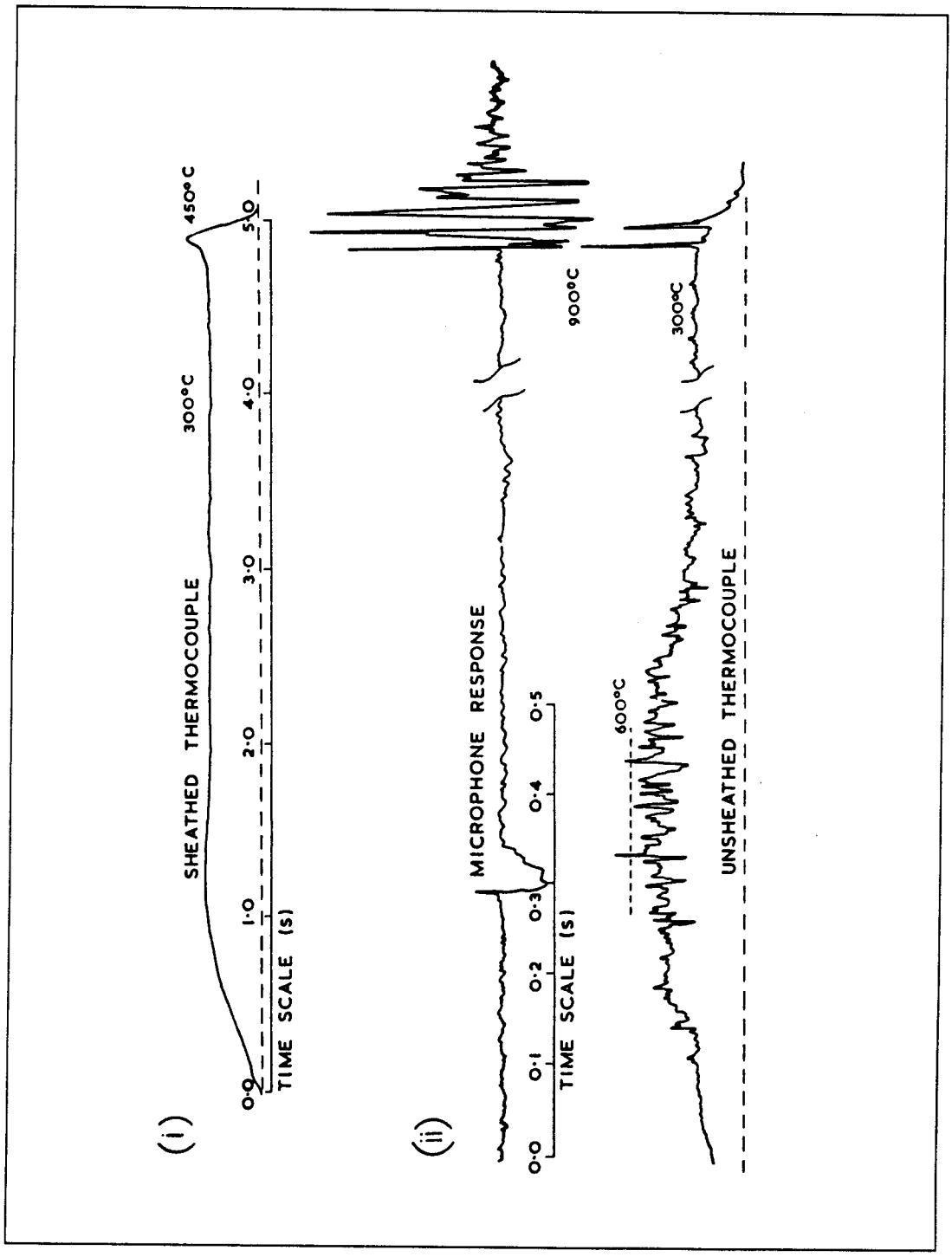

Figure 2.11

Thermocouple and Microphone Response During Sodium/Water Explosion [28]

Two different dispersion mechanisms were considered. One dispersion mechanism involves the growth and collapse of the vapor blanket around the drop [29,30]. At some point in the oscillations, jets of water penetrate into the drop and precipitate an explosion. This occurs when there is violent transition boiling around the drop, but when the water is above 95 C, stable film boiling exists and explosions do not take place. The lack of explosions with sodium drops reacting in the film boiling regime lends credence to the idea that the penetration of liquid jets is the dispersion mechanism that makes the explosion possible. However, Newman noticed that the microphone response (see Fig. 2.11) did not give evidence of a series of oscillations that grow and precipitate the explosion.

The second dispersion mechanism suggested by Newman, et al. involves super-heating the sodium so that rapid growth of metal vapor bubbles violently disperse the drop and initiate the explosive generation of hydrogen and steam [31]. With this in mind, they estimated the time necessary to bring the drop to the boiling point. This was calculated by considering a spherical drop separated from the surrounding water by a saturated vapor film at 100 C. A portion of the heat of reaction is assumed to vaporize water (to replace what has been consumed), and the remainder heats the droplet. The reaction rate is assumed to be the rate at which water arrives at the sodium surface, and this is calculated from kinetic theory. Diffusion through reaction product films, including the hydrogen that surrounds the drop, is neglected. This calculation supplies an absolute maximum reaction rate. With these assumptions, the resulting time necessary to heat the drop to boiling is given by:

$$\theta = 0.05 \frac{d}{K} \tag{2.2}$$

where **K** is given by:

$$K = \frac{23\rho_w}{9\rho_s} \sqrt{\frac{\Re T}{2\pi M}} \tag{2.3}$$

and where $\mathbf{d_0}$ is the initial diameter of the droplet, $\Re$ is the gas constant, **T** is the temperature, **M** is the molecular weight of water, and finally ρ_w and ρ_s are the densities of water and sodium, respectively. This model predicts that a sodium sample weighing a few grams may reach the boiling point in milliseconds. Newman conceded, however, that the production and dissipation of reaction products would play a major role in determining the actual reaction rate. The above calculation is meant to demonstrate that when conditions near the droplet surface are favorable, if only momentarily, the metal may rapidly heat beyond its boiling point.

Newman and Smith have studied the burning of sodium in water vapor [32]. Disks of sodium, with a radius of 22.5 mm and thickness of 6 mm, were heated in an insulated container. Steam was passed over the surface of the disks at a velocity of 3 m/s. Ignition of the sodium occurred when the metal attained a temperature of 98 C. The pool surface acquired an incandescent glow while the metal temperature rose rapidly. There was no apparent accumulation of solid products on the pool surface at this time. While the pool temperature climbed, small droplets of sodium were ejected, burning brightly and producing smoke in the water vapor atmosphere. Newman and Smith believe the ejection of droplets is caused by the rapid release of hydrogen within the surface layers. When the boiling point was reached, the flame region lifted from the surface of the pool,

generating a profuse amount of smoke. Temperature measurements of the flame were made with an automatic recording pyrometer and a conventional optical pyrometer. These instruments indicated that the flame temperature was approximately 1300 C, though measurements were difficult due to the smoke formation and transmission limitations of windows in the reaction vessel.

Experiments in which molten sodium (and NaK) was injected into water have been performed at the University of Nottingham [33]. These studies are part of an ongoing effort to better understand the sodium/water reactions that occur when leaks in the secondary heat exchanger of a fast breeder reactor arise. The experiment consisted of a glass cylinder filled with water and a syringe that injected the metal, as shown in Figure 2.12. High speed photography of the injections was made possible by flattening an area of the glass near the injection point. Pressurized argon was used to force molten metal through the syringe, which can be fitted with glass capillaries of 0.1 to 0.3 mm diameters. Unlike NaK, pure sodium is solid at room temperature and so a jacket that contains circulating hot oil was fitted around the injector for tests with sodium.

In a typical test, the metal left the capillary in the form of a jet and then broke up into numerous droplets with diameters of about 0.5 mm. The droplets rose through the water at approximately 280 mm/s and then became trapped in a layer of oil floating on the water surface. After injection, the water was drawn off and analyzed for metal concentration. Also, droplets trapped in the oil were removed, hydrolysed, and similarly analyzed. These analyses were then used to determine the amount of reacted and unreacted metal.

In experiments with NaK, the water column height and temperature were varied.

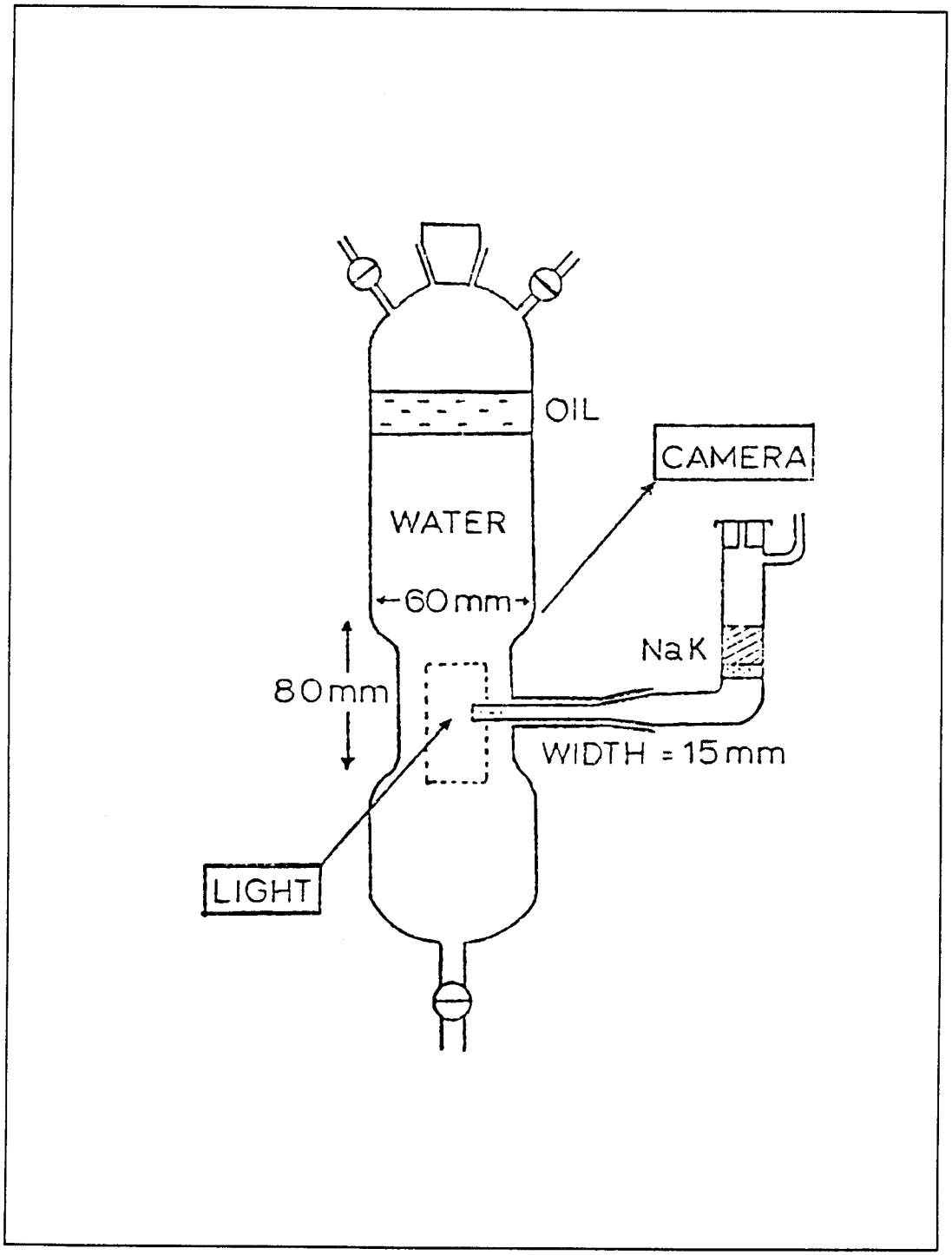

Figure 2.12

Apparatus for Sodium and NaK Injections Into Water [33]

The extent of reaction versus water column height for water at 20 C is shown in Figure 2.13 (the NaK was injected at room temperature). It is seen that the extent of reaction increased linearly as the water column height was increased for heights up to 100 mm. Beyond this the increase leveled off, presumably because the metal droplet became surrounded by an increasingly large hydrogen bubble which interfered with the reaction. The y-intercept of the best fit line is used to determine the amount of reaction that occurred at the nozzle, where the metal is in the form of a jet and has not yet broken up into droplets. Calculating the residence time of metal at the nozzle and the rate of bubble ascension permitted the calculation of reaction rates in the jet and bubble. From these calculations, shown in Figure 2.14, it was found that the reaction rate at the jet was about 100 times the rate in the bubble.

For tests with pure sodium, the initial sodium and water temperatures were approximately 130 C and 20 C, respectively (only the water depth was varied). It was found that the extent of reaction increased linearly for the water column heights investigated (25-75 mm) and that reaction rates for pure sodium were of the same order as those for sodium in NaK.

The review of experiments with sodium and water provided a necessary addition to the previous studies with lithium. The configurations of these experiments are more analogous to the lithium/water experiments conducted for the present study. They also include more pertinent observations and measurements. Most notably, data from the small-scale experiment which injected NaK into water resulted in determination of a reaction rate for sodium over a small water temperature range. Quantitative findings such as these were completely lacking for molten lithium, and provide a useful starting point

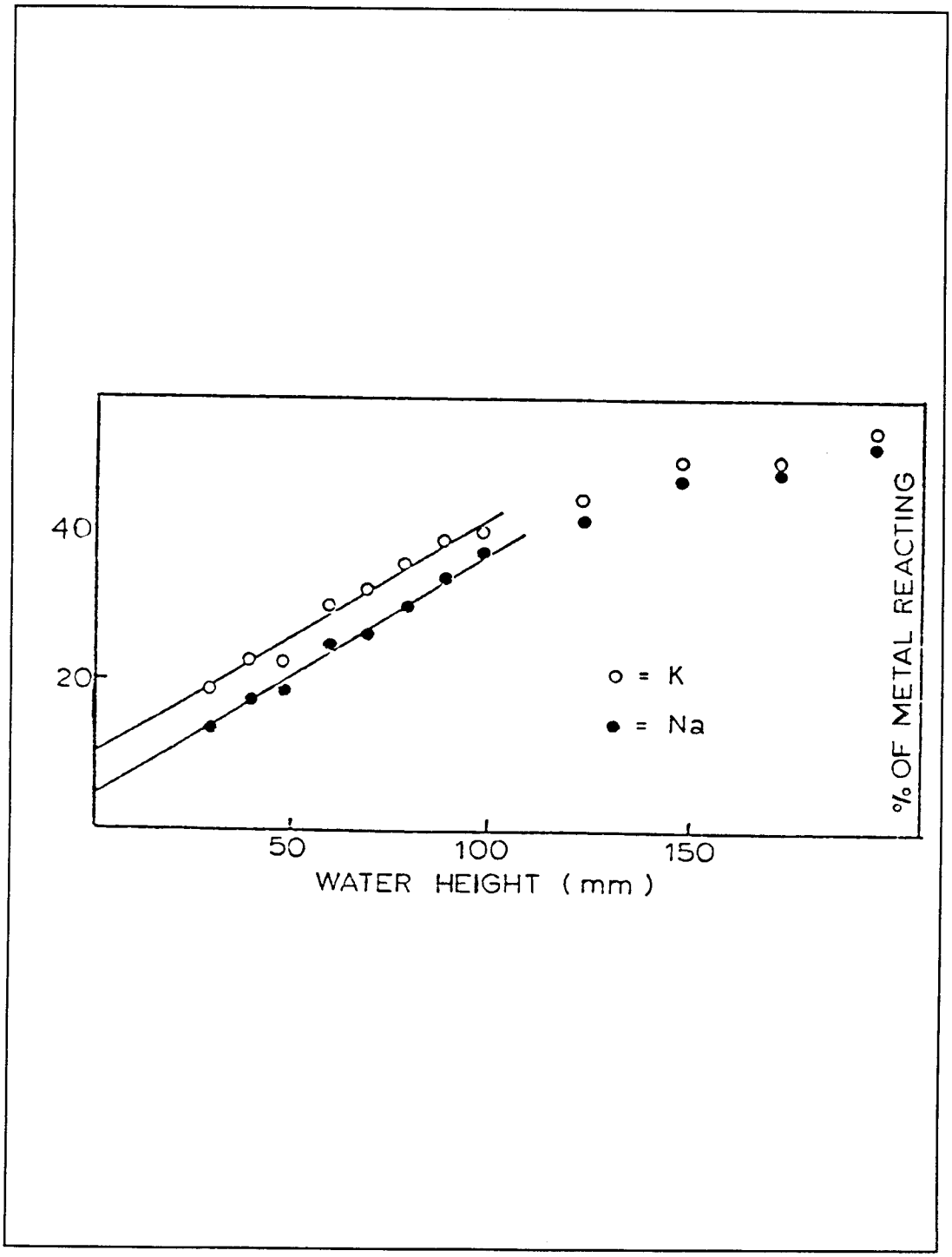

Figure 2.13

Extent of Reaction of NaK With Water at 293 K [33]

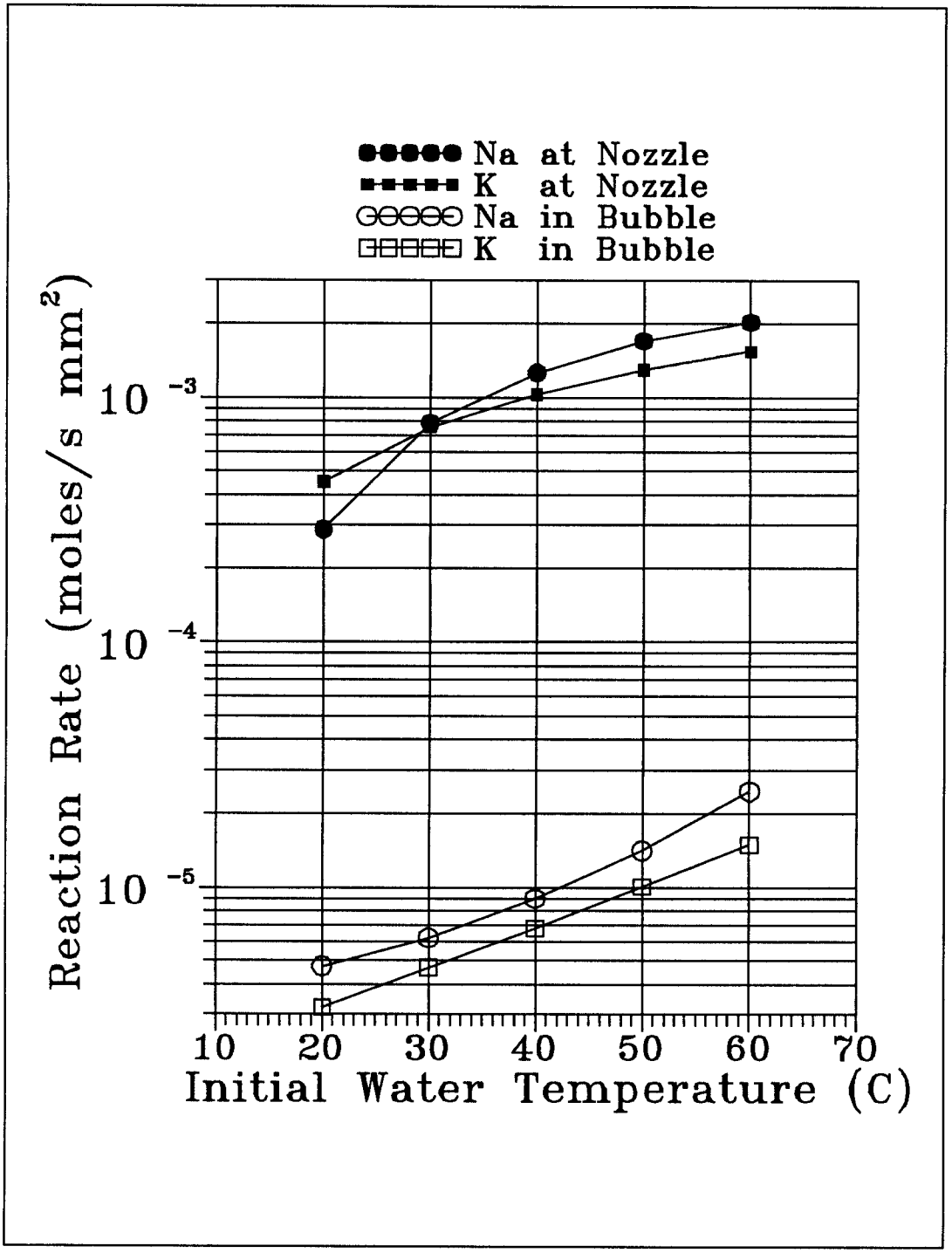

Figure 2.14

Reaction Rate of NaK and Water versus Water Temperature [33]

for comparison of the lithium/water test results in this study.

The observations of Newman, et al. indicated the explosive potential of an alkali-metal/water reaction. However, the mechanism(s) responsible for precipitating such an explosion were not clear. Two distinctly different mechanisms were suggested. First, the metal may be brought to its boiling point by the heat of reaction. Vaporization of the metal greatly increases the reaction rate because the reaction is no longer limited to the drop surface. Second, violent transition boiling may fragment the drop, increasing the surface area available for reaction and precipitating an explosion. These ideas will be considered in some detail when the results of lithium/water tests are analyzed.

II.IV Zirconium/Water Reactions

Since previous experimentation with liquid lithium droplets in water is lacking, it is necessary to refer to related work to find examples of metal-droplet/water reactions. Some studies of sodium/water reactions are useful, but these proved to be limited in scope. It is beneficial to review studies that include analytical modelling and the geometry of interest even though these are not for an alkali metal. One such study is an investigation of high temperature zirconium/water reactions by Baker and Just [34]. In these experiments, zirconium wire was suspended under water and melted by discharging a capacitor bank across the wire. Upon heating, the wire broke up into hot droplets which were oxidized by the surrounding water. The initial temperature of the droplets was calculated by assuming that uniform and adiabatic heat-up of the wire occurs. The degree of metal oxidation was determined by collecting hydrogen generated by the reaction, and from examination of specimen residue.

The first test series was performed with 0.76 and 1.5 mm (30 and 60 mils) diameter wires in room temperature water. Figure 2.15 shows the extent of reaction for a range of initial metal temperatures. The sharp break in the curve, near an initial metal temperature of 2500 C, marks a transition from reactions with a slow pressure rise, lasting a few tenths of a second, to explosive pressure rises that reach a final value in milliseconds. Peak pressures in these tests were on the order of 50 kPa.

Reactions in heated water were performed within a high pressure reaction cell containing degassed water. The test conditions ranged from 90 C water with a vapor pressure of 68 kPa to 315 C water at 10 MPa. These tests also exhibited a transition from slow pressure rises to explosive pressure rises, though the temperature for this transition was lower, about 1900 C. Peak pressures in these tests were about 10-20 times higher than in the tests with room temperature water. These reactions were much more extensive than those in room temperature water; however, there was no difference between runs with 90 C water and 315 C water. It appeared that beyond a certain point, the initial water temperature has no effect on the extent of the reaction.

To emphasize that initial metal temperature is not the sole determinant of the extent of reaction, Figure 2.16 has been included. The extent of the reaction is plotted versus mean particle diameter without accounting for initial metal temperature. Note that there is no abrupt transition in the curve where the extent of reaction rises sharply and the reactions become explosive. Baker and Just suggest that ignition of the explosion is a critical size phenomenon as well as a critical temperature phenomenon.

Besides performing experiments, Baker and Just developed a mathematical model to describe the reaction of a droplet of zirconium with water [34]. Their model consists

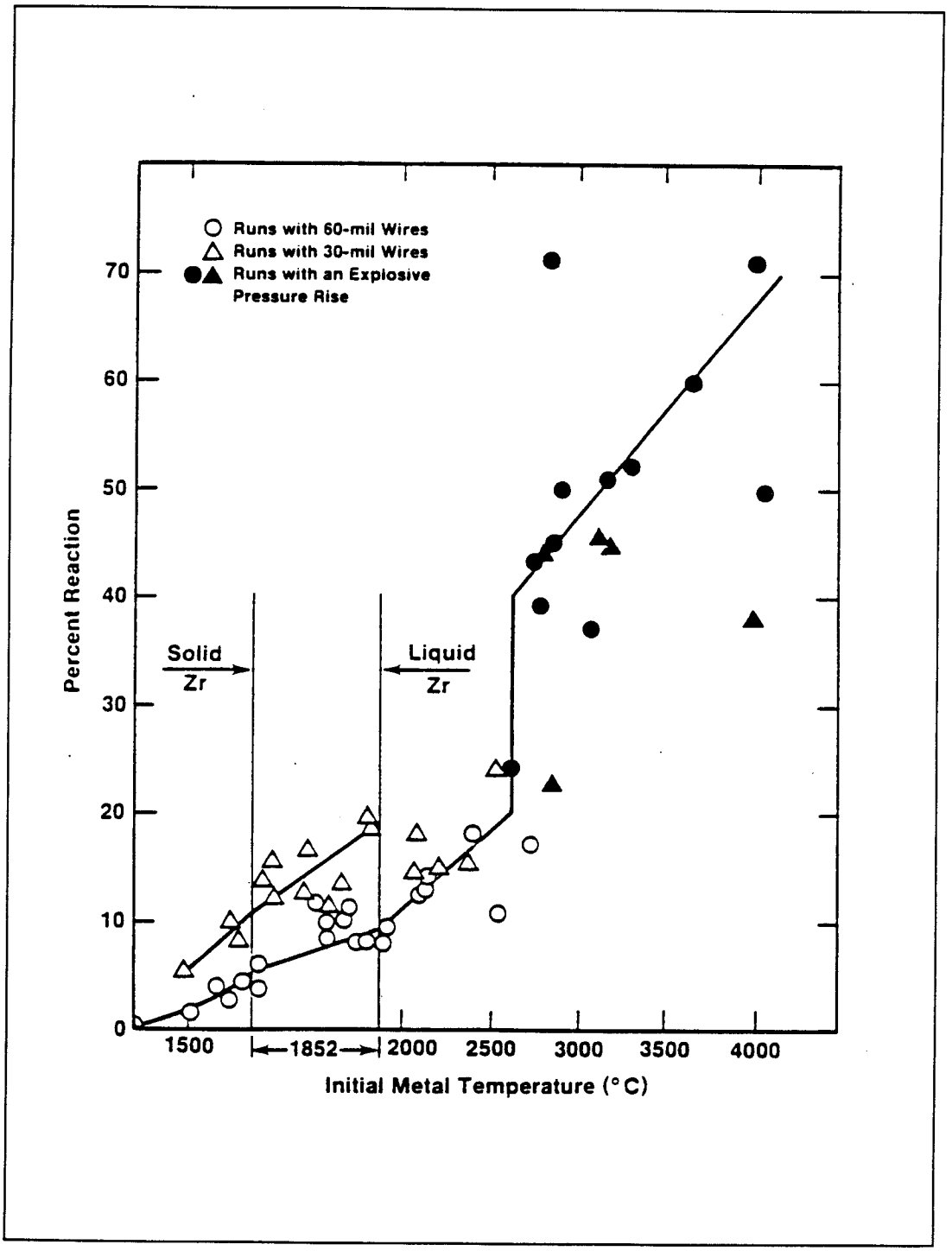

Figure 2.15

Percent Reaction of Zirconium in Room Temperature Water versus Initial Metal Temperature [34]

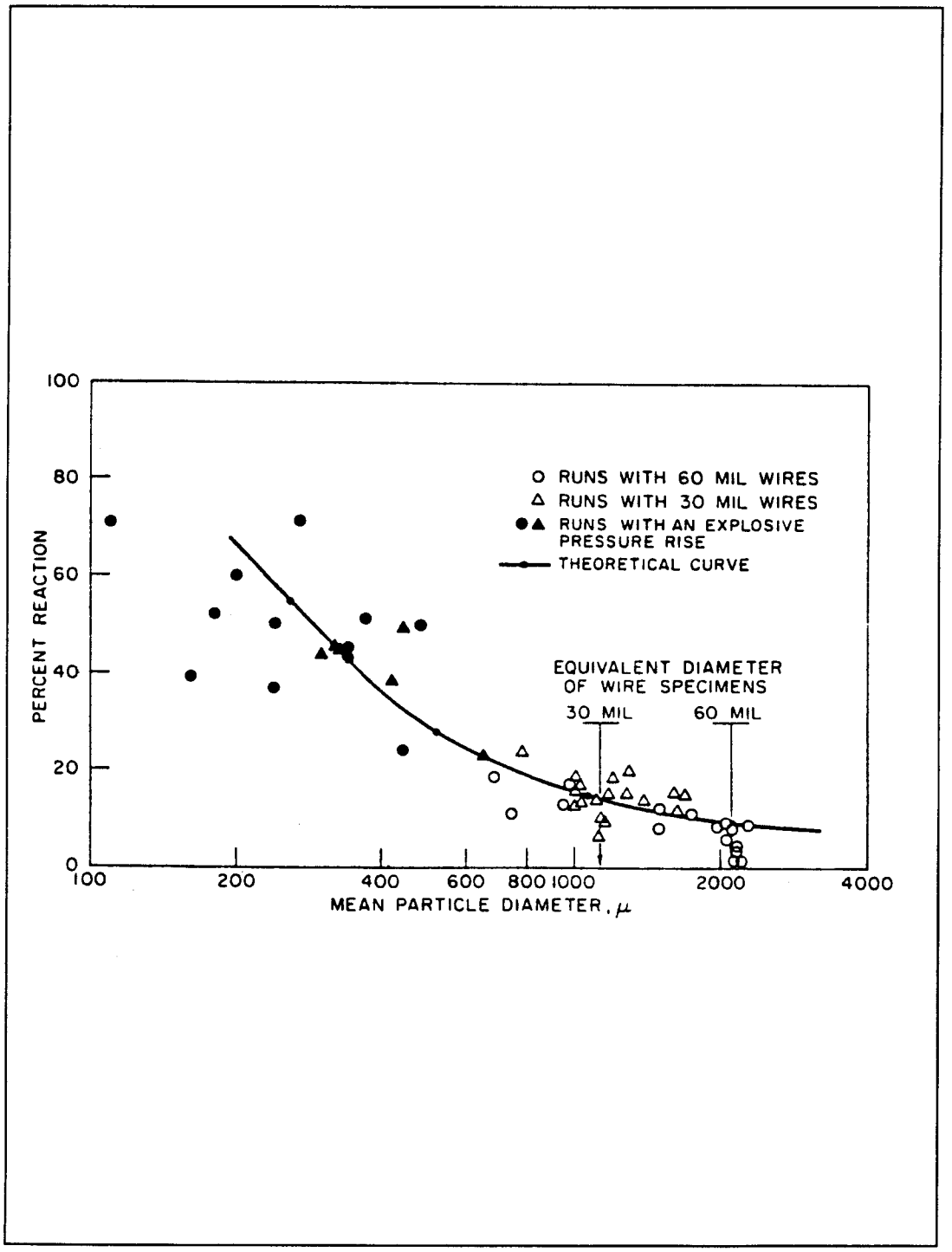

Figure 2.16

Percent Reaction of Zirconium in Room Temperature Water versus Mean Particle Diameter [34]

of a spherical drop separated from the surrounding water by a steam-hydrogen film. The drop consists of pure zirconium metal surrounded by a growing oxide layer. An energy balance on the drop produces the following:

$$\rho c \left[\frac{4\pi R^3}{3}\right] \frac{dT_m}{d\theta} = Q_{reac} - Q_{conv} - Q_{rad} \qquad (2.4)$$

where Q_{reac} is the heat from reaction, Q_{conv} is heat loss due to convection, and Q_{rad} is heat loss due to radiation. The radius, specific heat, and density of the sphere are **R**, **c**, and ρ, respectively. The rate of heat generation is governed by the rate at which water vapor reaches pure metal. This in turn depends upon two processes: **1)** the rate at which water vapor diffuses through the steam-hydrogen film towards the droplet surface while hydrogen diffuses away from the surface, and **2)** the rate at which water molecules diffuse through the oxide layer that coats the surface. To calculate the zirconium reaction rate, the diffusion rate through the film and oxide layer were calculated separately, and the reaction was assumed to proceed at the slower rate. At an early stage in the reaction, the rate is limited by diffusion through the gaseous film. Later on, diffusion through the oxide layer is the limiting process. Baker and Just used the model to calculate the percentage of metal which reacts, and this was found to be in general agreement with experimental findings. However, the model was unable to reproduce the experimental pressure-time curves for molten drops. The calculated gas diffusion reaction rate early in the transient resulted in a pressure rise that was considerably slower than that found experimentally. It was suggested that droplet motion played a role in removing the hydrogen blanket around the drop and that this resulted in a higher reaction rate. Evidence of this was found in high-speed films of the tests. In tests with a rapid pressure

rise, rapid particle motion was noted and velocities ranged between 6 and 15 m/s.

The experiments with zirconium and water suggested that a temperature threshold (for the metal) may exist beyond which the metal/water reaction rate increases sharply. It was found that increasing the water temperature lowered the metal temperature threshold for explosions, in addition to increasing peak explosion pressure. This contrasts with Newman's study of sodium and water where increased water temperature suppressed explosions. Though plausible explanations were given for the findings in each study, it is unclear why these trends are so different. Additional experimental and theoretical research in the area of molten-metal/water interactions with chemical reactions are necessary to clarify this issue.

II.V Molten-Metal Fragmentation Experiment

The final study to be discussed is a rather extensive investigation of heat transfer and fragmentation of a molten metal jet injected into water [35]. Several different metals were used: mercury, Asarcolo-158 (a bismuth, lead, tin, and cadmium alloy), a lead-tin alloy, and pure tin. The experiment consisted of an injector, a tank of distilled water at room temperature, high-speed camera, and pressure transducer. The main body of the injector was a stainless steel pressure chamber wrapped with resistance heaters. Metal was heated in this container and injected horizontally into the tank by actuating a solenoid on a gate-valve. A 1.6 mm inner diameter nozzle was drilled through an extension on the gate and this produced 1.6 mm diameter jets. The interactions were filmed through a glass window in the tank using a Fastax WF 3 camera with typical framing rates between 4000 and 5000 frames per second. The jet velocity was measured from the high speed

film and found to be near 2.3 m/sec for a typical test. The pressure transducer, located 18 mm below and 25 mm downstream of the end of the injection nozzle, measured over-pressures and had an input range of up to 6.8 MPa. Metal temperatures at injection were varied between about 90 C and 315 C.

Tests with mercury at 290 C resulted in explosions at a distance of about 2.5 mm from the nozzle. The resultant particles were ejected from the jet to a radius of about 2.5 mm. The film shows this particle distribution remaining stable for a few frames, then dispersing and moving downstream a few frames later. The diameters of the majority of these particles were less than 0.05 mm. The duration of the actual explosion was usually one frame, or less than 0.25 ms. Over-pressures generated by the explosions were high enough to momentarily stop the flow of metal from the nozzle (back pressure in the injector is 68 kPa).

Test results with the remaining three metals were similar to those with mercury. Some of the important conclusions drawn from these tests are:

- Solidification stresses are not necessary for explosion of the metal jet, as evidenced by tests with mercury.
- The over-pressure generated is a function of the explosion-expanded jet size, material properties, and ignition temperature.
- Explosions occur more readily when the vapor layer collapses or the jet encounters a very thin vapor layer.
- Explosive intensity is highly sensitive to the jet surface temperature and the explosive potential decreases as the surface temperature decreases. The bulk temperature of the jet seemed to be less important.

This last finding was determined by changing the injector gate and nozzle from stainless steel to yellow brass. The higher thermal diffusivity of brass enhanced cooling of the metal jet during injection. However, the injection time is short enough that only the outer surface of the jet was affected and the bulk temperature of the jet was largely unchanged. It was found that injections with the brass nozzle resulted in less frequent and less violent explosions.

Tests with Asarcolo-158 spanned the widest temperature range and received the most analysis. One finding was that explosions occurred closer to the nozzle as the injection temperature increased. Moreover, as this temperature was increased, the average diameter of the exploded jet increased. These trends are shown in Figure 2.17a. The data points at each temperature represent averaged values from several tests.

The fragments produced by the explosions were collected and sifted through screens of known mesh sizes to determine the particle size distribution. This, in turn, was used to determine the total particle surface area. Figure 2.17b shows the percent increase in area between the jet and solidified particles. As one might expect, the area change was quite large and increased with injection temperature.

The investigators believed that established theories concerning vapor explosions do not adequately explain the observed behavior. Their brief summaries of each theory are included here for reference:

Violent Boiling Theory: The violence of transition-nucleate boiling overcomes surface tension and the molten material is torn apart.

Weber Number Effect: This is a form of hydrodynamic instability, where the inertial forces overcome surface tension forces and breakup occurs.

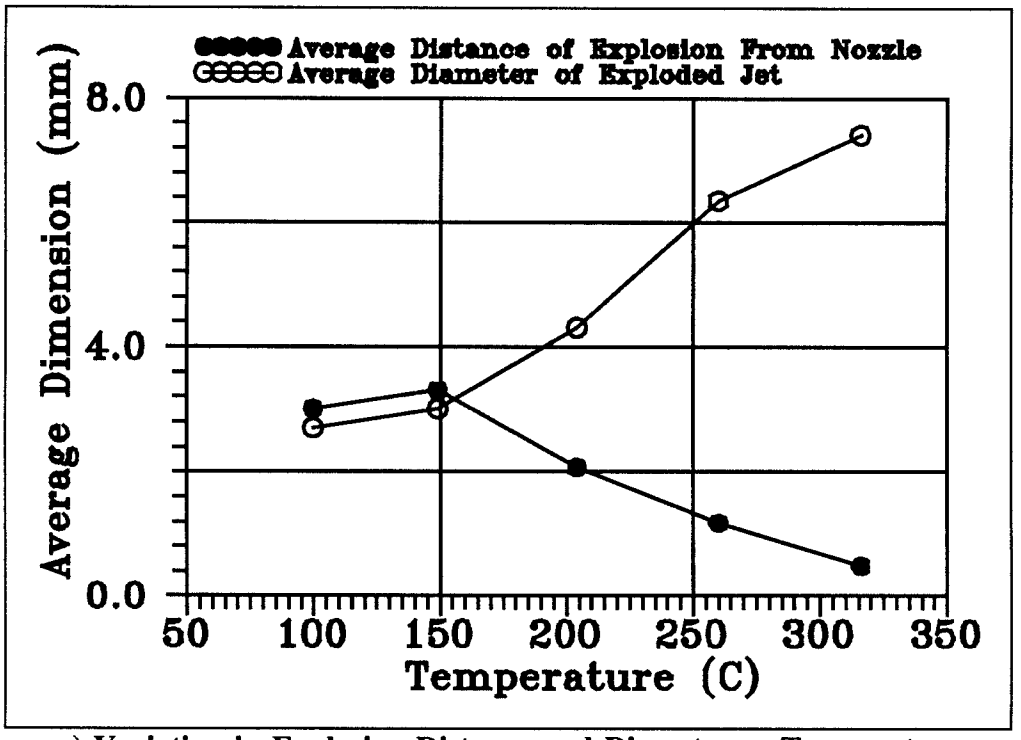

a) Variation in Explosion Distance and Diameter vs Temperature

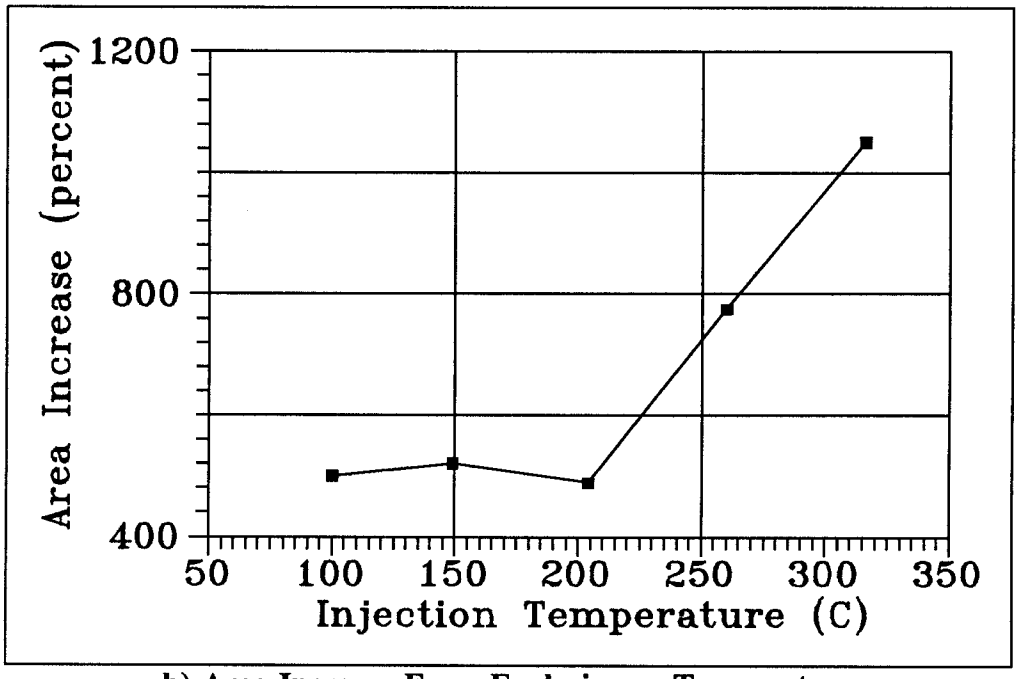

b) Area Increase From Explosion vs Temperature

Figure 2.17

Explosion Trends for Asarcolo-158 [35]

Shell Theory: A shell of solidified material forms, the molten interior is pressurized and breakup occurs.

Liquid Entrainment: Liquid is entrained in the interior of molten sample, rapidly vaporized, and the resulting pressure increase tears the drop apart.

Another theory postulated by Witte et al. [36] suggests the explosions are triggered by a thermal phenomenon in which the sudden collapse of the vapor film is accompanied by a corresponding increase in heat transfer. The thinning film offers a decreasing resistance to conduction heat transfer, resulting in outer regions of the metal cooling rapidly enough to experience 'thermal shock'. The quick temperature change produces a compressive stress wave which travels into the sample, focuses in the center, and then travels outward as a tensile stress wave. Once the wave reaches the surface again, tensile forces overcome surface tension forces and the sample explodes.

The principal motivation for including this last investigation is to emphasize that small-scale metal/water interactions can be explosive in nature even when chemical reactions are absent or insignificant. In this particular study the system geometry parallels that of the lithium/water experiments conducted for the present study. The primary message from these tests is that a metal jet injected into water may, through some mechanism, undergo sudden fragmentation. The sudden area increase that accompanies this fragmentation may lead to an explosive release of thermal energy from the metal. Since energy generation from chemical reaction is negligible, the explosive reaction must be preceded by a sudden area change. This contrasts with earlier studies in which temperature transients at the metal surface were postulated to precipitate explosions.

III SCOPING TESTS

The primary goal of this study is to examine the reaction of molten lithium with liquid water. Our intention is to observe the nature of the reaction and quantify the chemical reaction rate of these materials under controlled conditions. This chapter is devoted to a set of experiments in which droplets of molten lithium are injected into water. These are termed 'scoping tests' because the experiments consist mainly of qualitative observations without reaction rate measurements. Rate measurements were made in a second series of tests, which are discussed in chapter five. This chapter begins by describing the apparatus used to conduct the experiments, then outlines the procedure used to carry out these experiments. This is followed by a presentation and discussion of experimental results. The final section of this chapter pertains to measurement errors.

III.I Experimental Apparatus

The main features of the experimental design arise from a few strict requirements for the experiment. First, it is necessary to bring the lithium into contact with the water in a time that is relatively short compared to the reaction time to be measured. Secondly, it is essential to characterize accurately the surface area of lithium that is available for reaction. Since the density of lithium is only half that of water, dropping lithium into water from above would not result in a well defined droplet falling through the water. In view of this, a device was constructed that injects a drop of lithium into

the bottom of a water-filled container. As the drop rises through the water, measurements are made to determine the total hydrogen produced after a specified interval.

Figure 3.1 is a schematic that shows the major components employed in the experiment. A personal computer and a *Keithley System 570* brand data acquisition system (Keithley Inc.) obtain and store thermocouple measurements, control processes through relays, and trigger pressure measurements. Pressure signals, generated with quartz pressure transducers, are amplified and then stored in a digital oscilloscope. Water temperature is controlled by a Haake brand circulator, which is capable of both heating and cooling. A pump circulates distilled water in a closed loop between the Haake and reaction vessel. The oven is a piece of stainless steel pipe, 80 mm long and 40 mm in diameter, surrounded by a band heater. Oven temperature is set by manipulating input voltage to the heater, and thus setting output power, with a variable transformer. In the following paragraphs, additional details are provided for the more important components.

Injector

The most critical element of the experimental apparatus is the injection system. This system consists of an oven to heat the lithium, an argon line to maintain an inert atmosphere and lithium purity before injection, and a pneumatic cylinder to push the 'injector' upwards. The main components of the injector are illustrated in Figure 3.2. It is comprised of a 12 mm diameter stainless steel piston which attaches to the piston on the pneumatic cylinder. A steel sleeve, 50 mm long with an outer diameter of

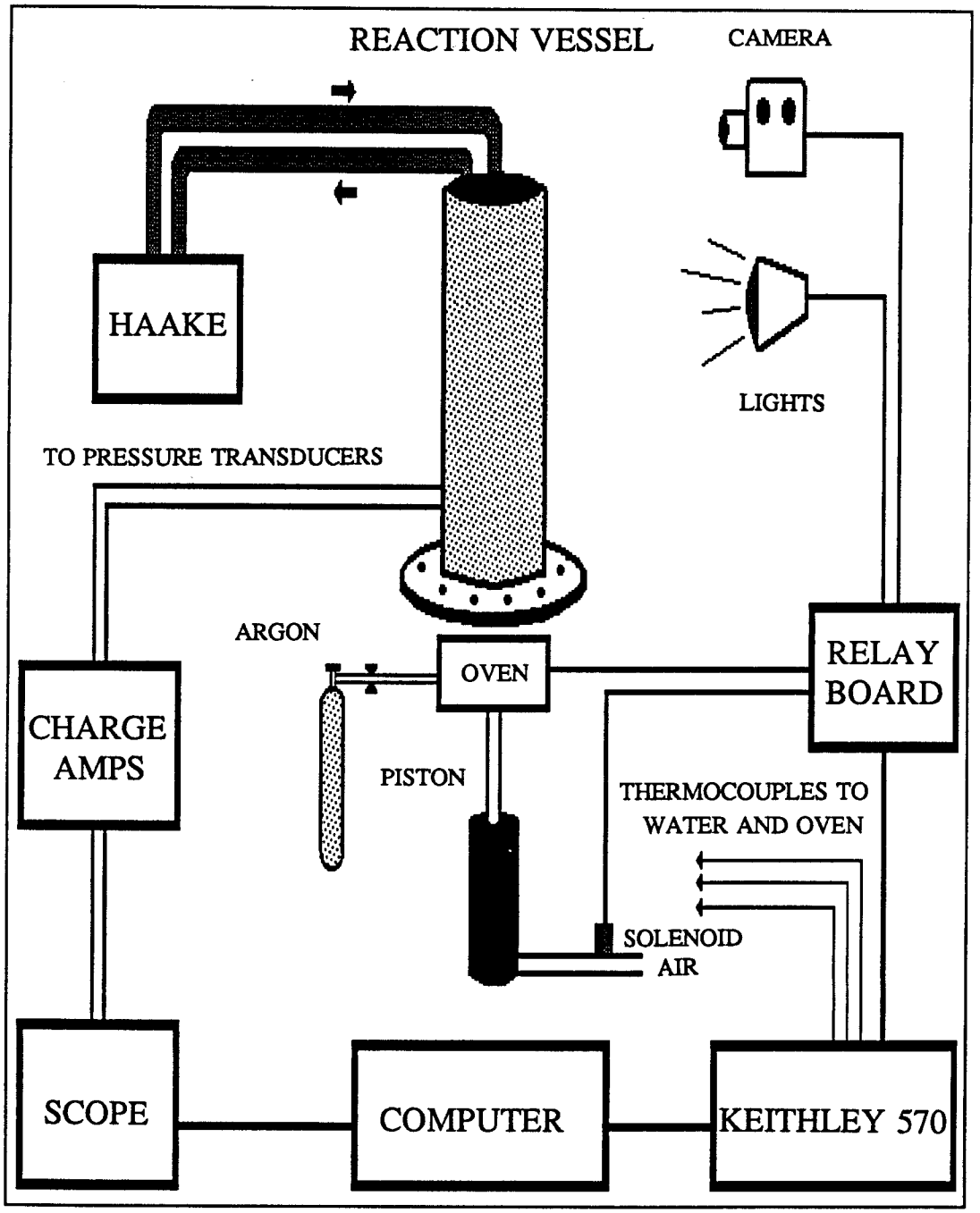

Figure 3.1

Lithium/Water Interaction Experiment

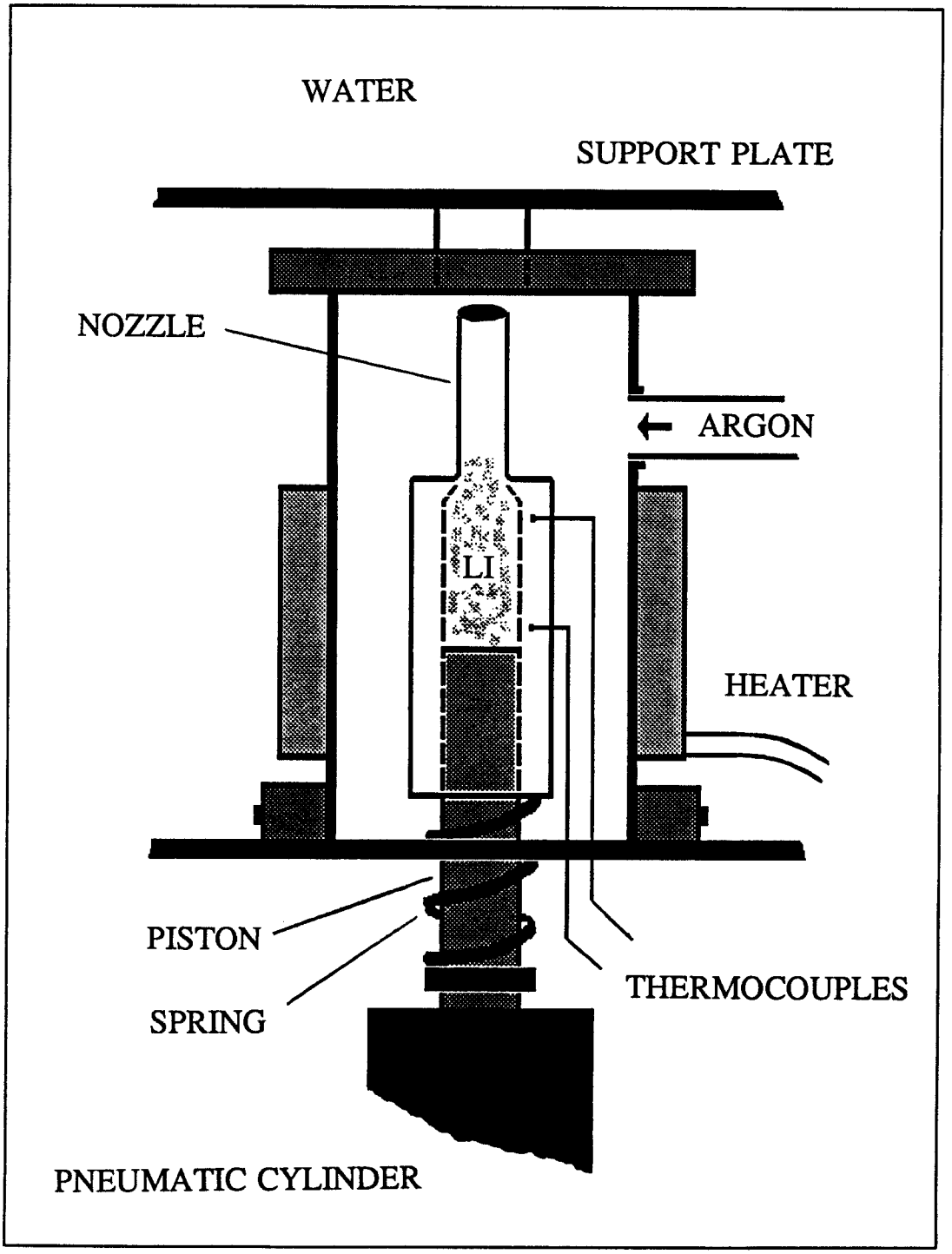

Figure 3.2

Lithium Injection System

25 mm, fits around the piston. Lithium is held within this sleeve in the volume just above the top of the piston. The sleeve reduces to a nozzle that is 26 mm long and has an inner diameter of 6 mm. The sleeve and nozzle are machined from a single piece of stainless steel. A seal between the sleeve and piston is provided by a stainless steel piston ring. Eight thermocouple wells have been bored into the outside of the sleeve for monitoring the lithium temperature. The bottoms of these wells are about 2 mm from the inside surface of the sleeve.

There is a hole in the oven lid and support plate to allow the nozzle to travel upwards where it may tear through a sheet of aluminum foil that serves as a rupture disk, covering the hole in the support plate. The injector travels upward until it hits the oven lid whereupon the sleeve stops moving and the piston continues up. This displaces the lithium and forces it into the water. The spring below the sleeve is intended to prevent lithium injection while the nozzle is tearing through the aluminum foil.

It is noted that early tests employed a somewhat different injector than that described above. It operated in essentially the same manner as the new injector but the lithium was stored in a stainless steel bellows. This bellows is 40 mm long, has an outside diameter of 30 mm, and a volume that varies between about 11 ml and 17 ml (a stainless steel slug was put into the bellows with the lithium to minimize lithium inventory). The wall is thin, 0.1 mm thick, to give the bellows considerable flexibility. Steel flanges are welded to each end of the bellows so that the pneumatic piston may be screwed into the bottom and a nozzle bolted to the top.

This steel bellows was abandoned for two reasons. First, sporadic explosions

were experienced during initial scoping tests and these occasionally damaged the bellows; repair and/or replacement became too costly and time consuming. Secondly, it was difficult to control the amount of lithium injected by the bellows. The convolutions in the bellows made it impossible to fill completely. Argon became trapped within the convolutions because of lithium's high surface tension and poor wetting characteristics. In practice, the bellows was usually filled to about 50% of full capacity. It was also found that, from one test to another, the total amount of lithium in the bellows before injection varied by one-half gram or more. This, in turn, varied the amount of lithium injected in each test. After two bellows were irreparably damaged, the injector shown in Figure 3.2 was introduced.

Glovebox

Pure lithium metal, when molten, is extremely reactive. Gases such as nitrogen, oxygen, and especially water vapor must not contact the molten lithium or the formation of more stable lithium compounds will result. A glovebox from Vacuum/Atmospheres Co. was purchased so that the lithium could be handled in an inert argon atmosphere. A purification system recirculates the argon, removing water vapor and oxygen until the concentration is less than 5 ppm by volume. All handling of lithium, except transportation of the injector and its solid lithium sample to the experiment, is done within the glovebox.

The lithium used in these studies was purchased from Alfa Products, a division of Morton Thiokol, Inc. It arrives in the form of pellets, about 2 mm in diameter, packed in argon. These pellets are delivered with less than 0.5% metallic impurities.

Pressure Transducers

Pressure recordings are made with two miniature, quartz, charge mode pressure transducers produced by PCB Piezotronics. These are high sensitivity transducers that have a rise time of two microseconds. The active components are encased in stainless steel and have the ability to measure pressure transients up to 68 MPa. They also can operate at elevated temperatures, up to 200 C. The minute current outputs of the transducers are converted to voltage signals by charge amplifiers and then stored in a Nicolet 4094 digital oscilloscope. The transducers are located 100 mm above the injection point, at opposite sides of the reaction vessel. In a typical test, one charge amplifier is set to record high pressure transients, up to 6.8 MPa, and the other for lower pressure transients, up to .34 MPa.

Data acquisition and Process Control

All thermocouple data is obtained through the Keithley System 570. This is a general purpose data acquisition and control device, which is used as an interface between components of the experiment and a personal computer. All process control is performed by computer via the System 570 and a relay board. The relays are solid state, powering devices that require 120V AC and can provide up to 3 amps of current. They are controlled by digital logic, and the relay board is optoisolated from the line voltage. The computer executes a program (written by the experimenter) that triggers the oscilloscope, operates relays, and acquires thermocouple data. Because the lithium-water reaction is a rapid transient, it is essential that triggering of the oscilloscope,

injector, and camera are carefully timed. Also, the potentially hazardous nature of the experiment encourages one to operate the equipment remotely. The Keithley system has been able to fulfill both these criteria.

III.II Experimental Procedure

The experimental procedure has two distinct phases. The first phase is preparation of the lithium for injection. The components of the injector (piston, piston ring, and sleeve) are scrubbed, rinsed with distilled water, and allowed to dry. They are then placed in a glovebox and assembled. The injector is now wrapped in heating tape and lithium pellets are dropped down through the nozzle as the injector heats up. The maximum temperatures used to melt the lithium never exceed about 250 C. Lithium is added until the level reaches the lower end of the nozzle. The assembly is now allowed to cool down to room temperature and then weighed to find the total inventory of lithium, typically about one gram.

The final preparation is made by readying the reaction vessel. A sheet of aluminum foil covers the hole in the aluminum support plate, with silicon rubber providing a seal to prevent water that seeps underneath the foil from entering the oven (see Fig. 3.2). The reaction vessel is bolted to the support plate and filled with distilled water to a depth of about 600 mm.

At this point, all equipment is checked to ensure proper operation. The relays, computer activated triggers, and all recording devices are tested. When this is completed, the injector is removed from the glovebox (a small plastic cap covers the

nozzle to prevent air from contacting the lithium) and thermocouples are attached. A valve is opened to permit argon flow into the oven, the cap covering the nozzle is removed, and the injector is placed within the oven and attached to the pneumatic cylinder. Power is switched on to the band heater that surrounds the oven, and the lithium begins to heat up while argon flows through the oven at the rate of about two liters per minute. The Haake circulates water between a constant temperature bath and the reaction vessel to maintain the desired water temperature. During this period, the computer monitors the temperatures of the injector and the water within the reaction vessel.

Once the lithium and water have attained the desired temperature, the second phase of the experiment begins. In contrast to the first phase, the experiment is now controlled exclusively by the computer. When the operator is ready, the computer turns the heater off, turns the tungsten lighting on, and begins a twenty second countdown. The operator then begins recording with the video camera. During these twenty seconds, readings are taken from all thermocouples every one-half second to establish the initial conditions of the test.

When the countdown reaches zero, the oscilloscope, high-speed camera (not always used), and solenoid on the high pressure line are triggered simultaneously. The piston travels upwards and the nozzle splits the aluminum foil diaphragm covering the hole at the bottom of the water tank. The nozzle continues to travel upwards until the sleeve of the injector hits the underside of the oven lid. This occurs about 40 milliseconds after the solenoid is triggered. Though the sleeve hits the oven lid, the

piston continues up and displaces the lithium within the injector, forcing lithium into the water. One drop with a diameter of about 5-10 mm is usually produced, but occasionally there may be several drops of varying size. Camera(s) and pressure transducers record the reaction.

A wire mesh has been positioned near the top of the reaction vessel, about 20 mm below the water surface. The mesh is intended to prevent the lithium drops from igniting hydrogen when they reach the top of the reaction vessel and mix with air. In addition, droplets that reach the surface tend to react violently, often sending small flaming drops of lithium out of the reaction vessel.

Four seconds after the injection is initiated, the computer turns off the lighting and activates a solenoid valve that allows water to drain from the tank. The lithium drop(s), caught in this mesh during their initial ascent, are still stuck to the wire as the water recedes. The reaction slows soon after the water is drained, so a visual check of the number of drops produced by the injection can be made. After waiting a few minutes, the injector is cool enough to detach from the pneumatic piston. It is placed in a bucket of water to react any remaining lithium.

III.III Experimental Results

Initial tests with lithium and room temperature water were conducted in a transparent acrylic reaction vessel so that the reactions could be readily observed. As noted earlier, the stainless steel bellows was employed in these early tests. Films and pressure transducer recordings indicated relatively benign reactions. Lithium droplets

rose from the bottom of the reaction vessel while a hydrogen bubble formed around the droplet, growing as the lithium traveled upward. During some tests, the lithium was seen to be glowing orange after it had risen some 250 mm through the water.

Later tests were intended to observe qualitative differences in the lithium/water reaction when the water is above room temperature. It was discovered that, under these new conditions, the reaction may become explosive. This finding initiated a series of tests intended to discover the lithium-water temperature combinations conducive to explosions. The acrylic reaction vessel, used in early tests and destroyed by an explosive reaction, was replaced with an aluminum reaction vessel. This limited visual observation of the reaction to views from the top of the vessel. With these limitations, it was not possible to make appropriate measurements permitting determination of the rate of hydrogen production. Measurements were limited to initial temperatures of the reactants and peak pressures in the event of an explosion. The video camera recorded the reaction by viewing down into the reaction vessel with the aid of a mirror. The photography is rather poor in this configuration, and so the films were used only to establish whether the injection had proceeded properly.

Figure 3.3 gives test results in terms of the initial water and lithium temperatures. The circular symbols indicate tests performed with the stainless steel bellows while square symbols are for tests with the injector shown in Figure 3.2. The open symbols in this plot indicate tests where lithium reacted in a relatively benign manner, with the lithium droplet(s) reaching the water surface intact. The solid symbols signify tests where the lithium exploded soon after injection. Finally, the three asterisks

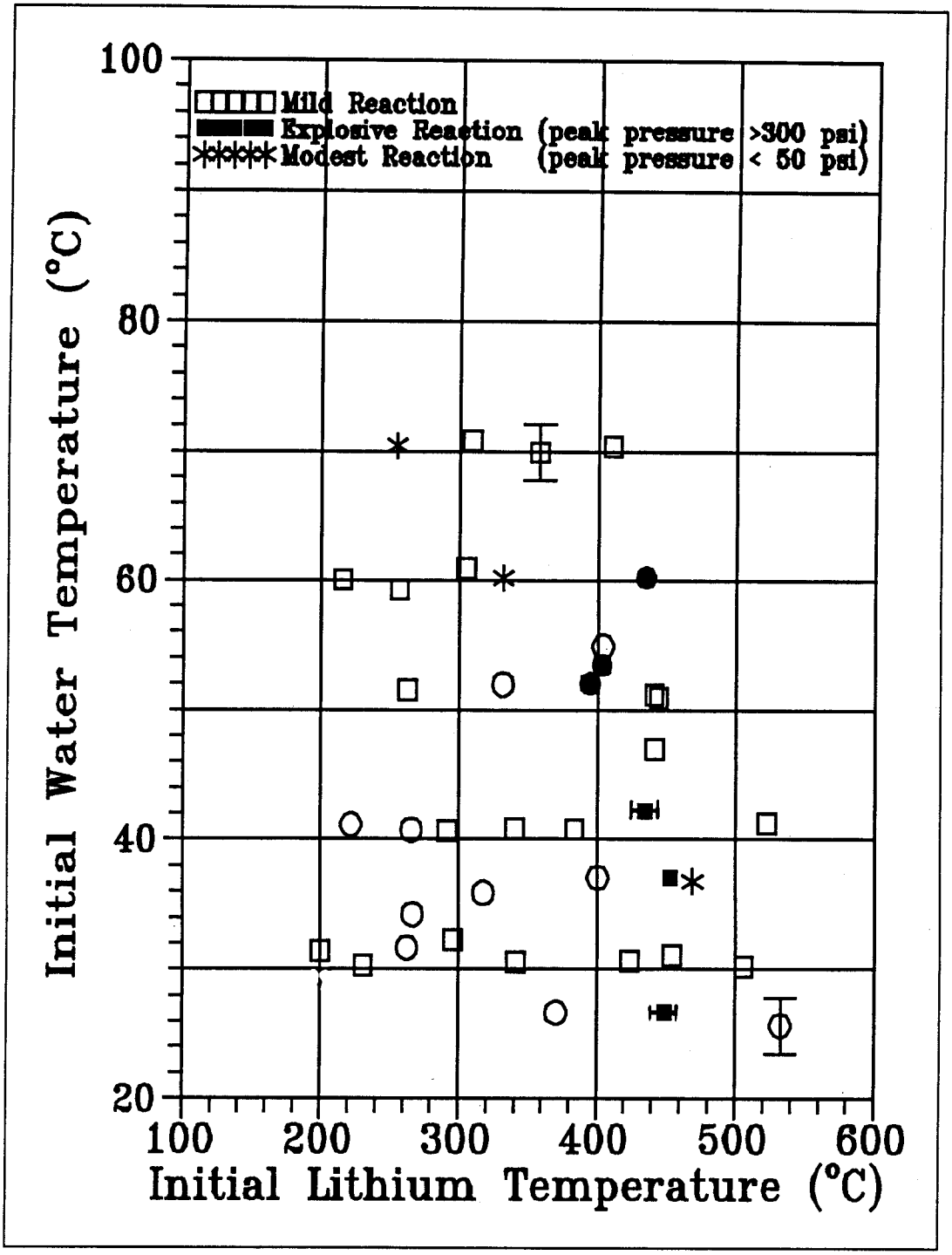

Figure 3.3

The Reaction of Molten Lithium Droplets in Water at Various Initial Lithium and Water Temperatures

in Figure 3.3 indicate tests that resulted in measurable pressure transients, though these transients were a full order of magnitude smaller than those identified as explosive. A plot of peak pressure versus initial lithium temperature for the explosive and modestly reactive tests is given in Figure 3.4. The data shown in these figures has been tabulated in Appendix A for reference. Error bars are included on selected data points that have uncertainty values typical of these measurements. Uncertainties in the initial reactant temperatures and pressure measurements are listed in Appendix A. Calculation of these uncertainties are discussed in section 3.5.

Figure 3.3 shows that a temperature threshold exists above which ignition (an explosive reaction) becomes more likely. This threshold is a function of both water and lithium temperature. As the initial lithium temperature increases, the water temperature necessary to initiate ignition decreases. Crossing the threshold increases the probability of ignition but does not ensure it. Figure 3.4 shows a clear trend toward increasing peak pressure as the initial lithium temperature is increased. It is suggested that the higher temperatures correspond to greater vaporization of the metal during ignition and this results in greater work output (impulse).

A footnote to the data presented is necessary: some tests with explosive reactions have been excluded from Figures 3.3 and 3.4. For a few tests, the experimental apparatus failed to function correctly, and this often resulted in an explosion. Experience has shown that if the lithium is not injected properly, an explosion may result regardless of the initial conditions for the test. It was difficult to have consistent criteria for judging whether an explosion was caused by equipment failure. The video

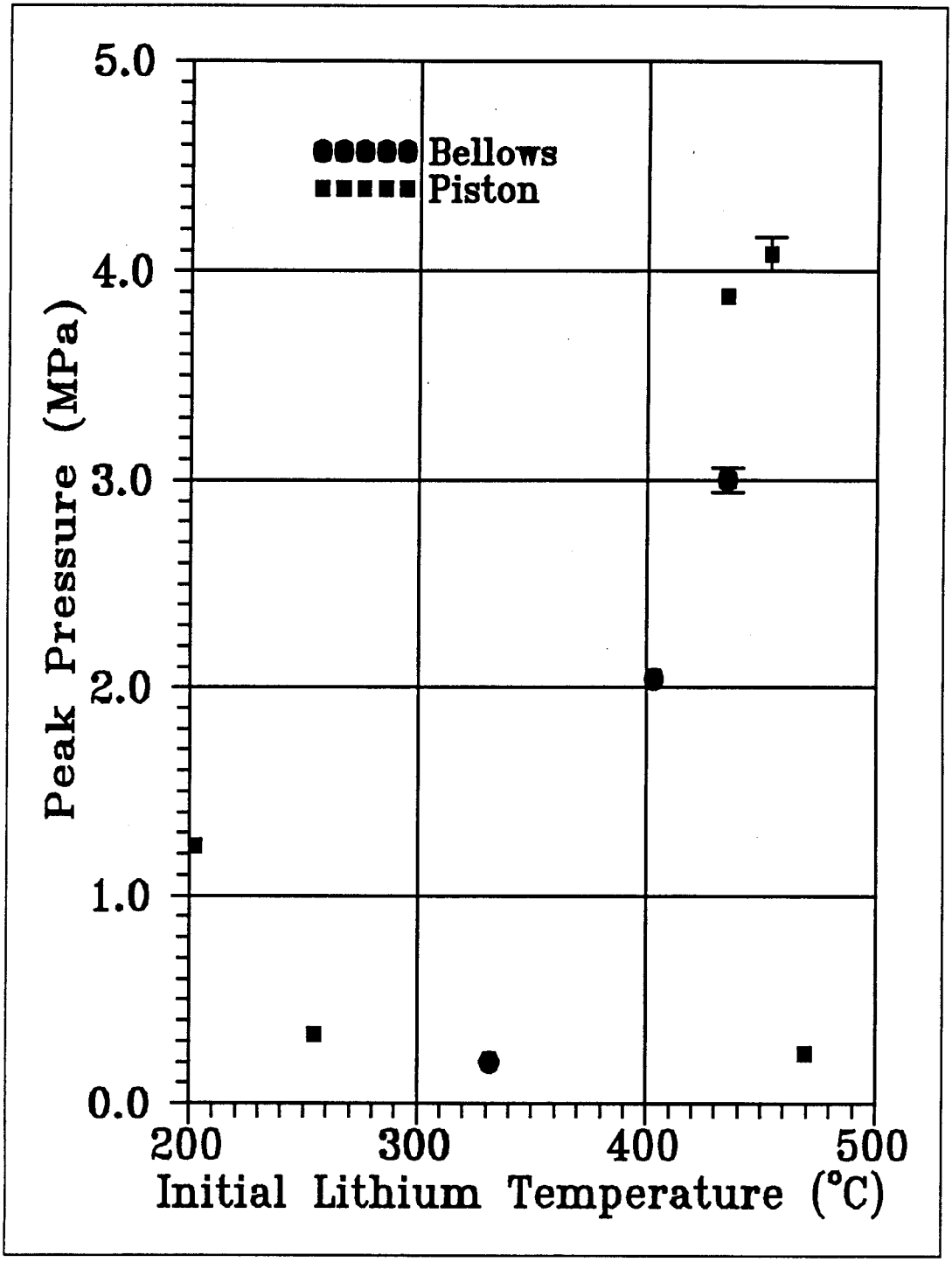

Figure 3.4

Peak Explosion Pressure versus Initial Lithium Temperature

camera and high-speed camera provided the best record of how the injection proceeded, but their use became severely limited when the aluminum reaction vessel was introduced. The video camera was often used as a tool to monitor potential trouble spots during injection, and so its location and point of view often changed. From test observations and video tape analysis, any sign of sparks or flame exiting the bottom portion of the oven was judged to be an indication of a failed injection. When this occurred it was concluded that lithium left the injector before the nozzle tore through the foil, and lithium was injected into the oven, as well as the reaction vessel. These tests have been omitted from Figures 3.3 and 3.4.

Figures 3.5a and 3.5b are included to provide sample pressure traces of mild and explosive reactions. The first plot is a typical pressure trace that always appears when the reaction is not violent. The peak near 60 milliseconds shows the moment when the injector strikes the oven and produces a small pressure wave in the reaction vessel, rather than a rise in pressure due to the lithium/water reaction. Note that the abscissa in both figures refers to time elapsed after the pneumatic cylinder has been triggered.

Before discussing what conclusions might be drawn from the results of these scoping tests, it is appropriate to describe the observed explosion phenomenon in more detail since the remainder of this chapter focuses on these occurrences. The explosion described here involved water and lithium at initial temperatures of 53 C and 403 C, respectively. The pressure trace for this test is provided in Figure 3.5b. The steel bellows was used to inject between 1 g and 0.5 g of lithium while both the high-speed and video cameras recorded the reaction. The high-speed camera provided more useful

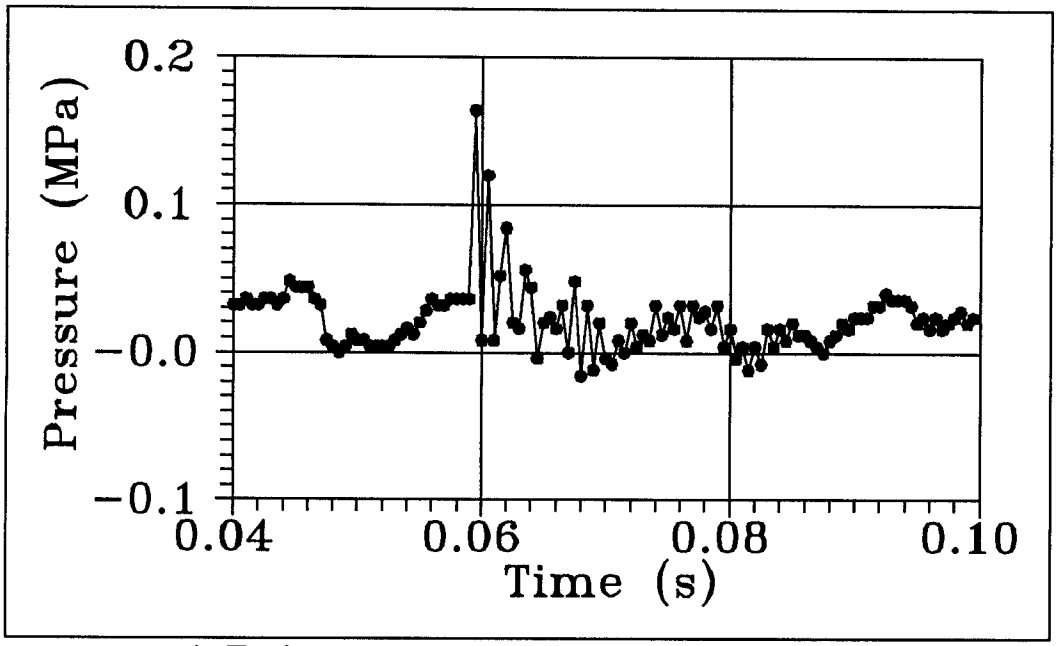

a) Typical pressure trace during modest reaction

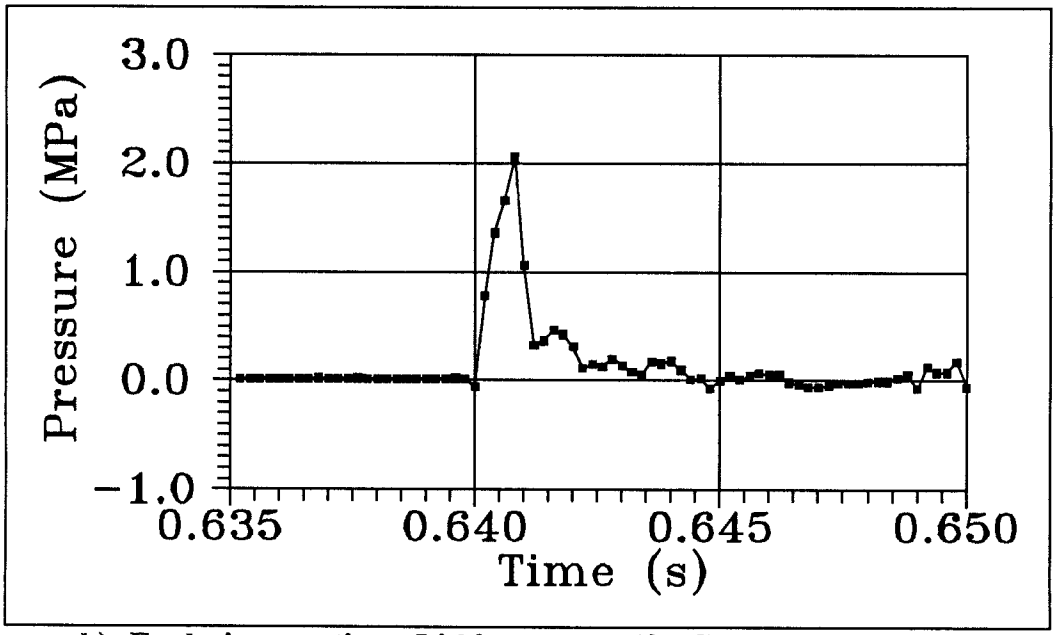

b) Explosive reaction. Lithium temp. 403 C, water temp. 53 C

Figure 3.5

Pressure Transients Measured After Injection

information because it had a closer view of the reaction and because the framing rate, 2000 frames/second, was used to measure elapsed time. The black and white film shows a roughly spherical lithium droplet, about 10 mm diameter, forming in the water at the nozzle exit. It is dark colored rather than shiny (because it is silhouetted by the bright tungsten lighting and possibly because a reaction product layer has formed) or incandescent. A small bubble of gas separates from the top of the drop and another begins to form. The gas layer surrounding the drop is so thin as to be barely visible, on the order of a millimeter thick. Just as it appears that the droplet is about to detach from the nozzle, it ignites so that droplet and nozzle are lost in a small irregular region of white flame. The transition from an unremarkable droplet to ignition takes place between one frame and the next, or 0.5 ms. Within another millisecond, the entire area around the injection point is engulfed in a mushroom of white flame. The elapsed time between lithium beginning to exit the nozzle and ignition is 300 ms. A pressure spike of 2 MPa with a 2 ms width was measured by a transducer located near the explosion.

III.IV Discussion and Analysis

The literature review of chapter two provided some insight into the phenomenon of metal ignition with regard to both experimental observations and attempts to model and explain the phenomenon. The term 'metal ignition' is commonly used in instances of extremely rapid metal oxidation, when flames are present or an explosion occurs. The review was far from a complete sampling of papers on the subject but one point was clear: the cause(s) of metal ignition is not well understood. The studies in chapter

two suggested various explanations, some of which were contradictory. For example, experiments with sodium and room temperature water exhibited explosions for large sodium samples but not for smaller samples. Also, explosions ceased when the initial water temperature was raised to 95 C. In contrast, the work with zirconium and water clearly demonstrated an increasing tendency toward explosive reactions as the particle size decreased and the water temperature increased.

In the remainder of this section, we will consider some mechanisms that could account for these explosions. The discussion is limited to explaining the observed lithium/water explosions rather than considering the topic of metal ignition in general. We begin by noting relevant observations made during the tests. These are intended to provide a basis of facts before postulating an ignition model, which is done in the next chapter.

The first observation is that both explosive and mild reactions begin with the same sequence of events. As the lithium drop forms at the nozzle exit, it is seen to be surrounded by a thin gas layer and the surface temperature must be relatively low because visible radiation is not evident. In a mild reaction the drop separates from the nozzle and rises, usually growing quite hot after traveling about 200 mm through the water, glowing orange from inside the hydrogen bubble created by the chemical reaction. In an explosive test, the drop ignites before separating from the nozzle or after travelling a few centimeters upward. There is no apparent transition to an incandescent drop before ignition, and if this does indeed occur, it must take place on a time scale less than one-half millisecond (the framing rate of the high speed camera). Judging by

the difference between the two types of reaction, it seems that a highly elevated surface temperature is an insufficient condition for ignition.

Up to this point, there has been no clear distinction between the drop temperature and surface temperature. This should be clarified because the two temperatures may be quite different and this could have some bearing on the ignition mechanism. For a step change in surface temperature of a body, the pertinent dimensionless time is the Fourier number [37]:

$$Fo = \frac{k}{\rho c}\frac{\Delta\theta}{d^2} \qquad (3.1)$$

This relation, based solely on conduction, indicates how far into the drop a temperature excursion at the surface has penetrated after a time $\Delta\theta$. Heat transfer due to circulation patterns within the drop is neglected. This should be a good assumption because the time scale of interest is short. For a typical drop, $\mathbf{d} \approx 1$ cm and $\mathbf{k}/\rho\mathbf{c} \approx 0.2$ cm^2/s. Consider the case where ignition took place between one frame of the high speed film and the next, nearly a step change in temperature over $\Delta\theta$~.5 ms. The Fourier number in this instance is on the order of 10^{-4}, much too small for the interior of the drop to be affected by the initial transient at the surface. This also suggests that if the surface temperature transient is the key element in the ignition mechanism, drop size should be unimportant (for **d** near 0.1 mm or larger) because it behaves as a semi-infinite body.

Some studies of metal ignition focus on the role of a temperature threshold in predicting an ignition point. This threshold may correspond to the point at which the metal-oxide melts, the metal vapor pressure reaches a critical value, or the metal simply reaches some specified point above the melting temperature. This is too simplistic a

view to explain observations from the scoping tests. For example, lithium hydroxide, the primary reaction product, melts at 471 C. This temperature has obviously been surpassed by the glowing droplets (visible radiation first becomes evident in darkened surroundings at about 500 C, the so-called Draper Point), which are not seen to explode.

A slightly more sophisticated analysis suggests that ignition occurs when energy generation from oxidation exceeds the losses to surroundings. Under the proper conditions, there is positive feedback between temperature and reaction rate, resulting in ignition. The exothermic reaction at the metal surface increases the local temperature which, in turn, elevates the reaction rate (this may rise exponentially with temperature). In addition, as the film separating the reactive surface from surrounding water heats up, diffusion of water molecules across the film increases. If the metal temperature increases to its boiling point at the local pressure, the reaction takes on a new character, where water molecules and lithium atoms meet in the film rather than exclusively on the metal surface. This may, in fact, be the event that precipitates ignition. Note that the boiling point per se may not be a crucial value; the molten-metal vapor pressure increases continuously with temperature and so there should be some lithium vapor at lower temperatures. Transition to a vapor phase reaction (and ignition) results when reactions in the film become 'important', and this could occur somewhere below the boiling point.

While the mechanisms just described combine to elevate the metal temperature, other mechanisms act to dissipate the energy generated. Radiative heat losses increase with the fourth power of temperature, the gaseous film grows and inhibits diffusion of

water to the metal surface, and a reaction product layer forms on the metal. The difficulty now lies in predicting, for a particular set of initial conditions, whether the chemical reaction rate levels off to an equilibrium state or increases toward ignition. In the next chapter, a numerical model is formulated to study the metal water reaction. This is used to examine and explain some of the experimental findings presented in this chapter.

III.V Measurement Error

Measurements made during the scoping tests are used to identify three quantities: lithium temperature prior to injection, bulk water temperature, and peak pressure at the reaction vessel wall (if an explosive reaction occurs). This discussion is limited to relating how uncertainties in these three quantities are found. The bulk of this section is devoted to explaining how uncertainties in the initial lithium and water temperatures are calculated. This is followed by a short discussion of pressure measurement error.

The number of thermocouples used in these experiments changed over the course of the scoping test series. In addition, the arrangement of these thermocouples was occasionally modified. These changes are detailed below before discussing errors.

The stainless steel bellows was used as an injector in tests 9-26. In tests 9-19, the lithium temperature was measured with two thermocouples. Bare thermocouple junctions are in the gas layer above the lithium, about 3 mm above the metal surface. In tests 20-26, two more thermocouples were added. Two holes were drilled into the flange at the top end of the bellows. The base of each well is about 1 mm from the

inner surface of the flange. The bellows was filled with lithium until the metal surface was roughly level with this flange, so the two new thermocouples were separated from the lithium by about 1 mm of steel. All tests after #26 used the stainless steel piston as the injector. Eight thermocouple wells were drilled into the steel sleeve, and the bases of these wells were about 2 mm from the inside surface (see Fig. 3.2). Four thermocouples were used to measure lithium temperature in tests 27-37, and in all succeeding tests, eight thermocouples were used.

Water temperature was measured with two thermocouples that were within about 50 mm of the reaction vessel wall, and approximately 10 mm above the aluminum support plate (see Fig. 3.2). Additional temperature measurements made during some early tests showed that thermal stratification in the water is negligible, even when hot water is used. This demonstrated that these two thermocouples were sufficient for characterizing the initial water temperature.

All temperatures were measured with standard K-type (chromel-alumel) thermocouples, purchased from OMEGA Engineering Inc. The published limits of error for these are specified to be approximately 2.2 C or 0.75%, whichever is greater [38]. The initial temperature given by any one thermocouple, or channel, was calculated from the average of forty readings taken during the twenty seconds prior to injection. The standard deviation of these forty readings was always much smaller than the error limits.

Initial reactant temperatures were calculated by averaging the values calculated for each channel. The standard deviation about this average was then computed. The

uncertainty in initial metal temperature was set equal to this deviation, or the upper limit of individual thermocouple error, whichever was greater. These uncertainties are tabulated with the initial conditions for each test in Appendix A. They range from a low of 2 C to a high of 12 C. A typical value for the uncertainty is about 3-4 C.

The deviation about the average water temperature was always much less than the thermocouple error limit of 2.2 C. Consequently, the uncertainty in initial water temperature was conservatively assumed equal to 2.2 C.

Error in pressure measurements arise from nonlinearities in transducer response, and response changes with temperature. Factory calibration curves demonstrate that transducer linearity is within one percent of full scale. The temperature coefficient is approximately 0.02%/C. Using these values, the maximum uncertainty in peak pressure measurements was estimated to be two percent of the measured pressure.

Comparisons of measured peak pressures (in Fig. 3.4) should be made with caution for two reasons. First, two different steel bellows and a steel piston were used as lithium injectors. This introduces uncertainty in the lithium droplet size produced by the injection. This, in turn, may be expected to effect the peak pressure produced in an explosive reaction. Intuitively, one could presume that a larger pressure source term (more lithium) would produce a larger peak pressure.

The second source of uncertainty in the peak pressure lies in the fact that three different reaction vessels have been used over the course of these tests. The overall size of each vessel is roughly the same, but the materials are different. There is certainly an appreciable difference in the mechanical properties of acrylic compared to steel or

aluminum. This might be expected to affect the measured peak pressure for a given source impulse. Examination of test data shows that pressure pulse rise times range from roughly 500 us to 50 us. A pressure pulse could propagate to the reaction vessel wall during the longer rise time, which affects the pulse height. Still, we believe that these uncertainties do not have a profound effect on the trends observed in the experimental data.

IV METAL/WATER REACTION MODEL

Experimental results presented in the previous chapter revealed a dual nature of the lithium/water reaction. Some reactions were mild, while others were violent and destructive. We wish to discuss and explain the results of these tests in the context of a physical model. This chapter is used to develop and present such a model. Our interest is in calculating the rate at which a drop of lithium heats up during a reaction with water. The model is also used to estimate reaction rates under various conditions.

We begin by introducing a numerical model for conduction heat transfer within the drop. It is a transient finite-difference model that includes conduction, convection, and radiation heat losses from the drop surface. We then detail two different models for mass transfer of water vapor to the lithium drop surface that are incorporated into the numerical model. In the first case, mass transfer occurs through stagnant diffusion across a vapor film. In the second case, mass transfer rates are calculated with a film boiling model that includes convection effects. The mass transfer model is a key element in the numerical analysis because it governs the rate at which the drop temperature rises. After each mass transfer model is outlined, a graphical presentation of the numerical model results is provided. The results and their implications are then addressed.

IV.I Numerical Model for Heat Transfer in Lithium Droplet

To understand the ignition process, it is useful to calculate the temperature change of the lithium drop as a function of time, given different mass transfer mechanisms. We

would like to know the likelihood of heating a significant portion of the drop to the high temperatures observed experimentally. The primary concern is the transfer of water vapor across the gaseous film to the metal surface, not from the surface through a reaction product layer. Other studies have suggested that this latter mechanism does not limit the reaction rate in early stages [24,39]. The starting point is Equation 2.4, which gives the overall energy balance for the lithium drop:

$$\rho c V \frac{dT}{d\theta} = Q_{reac} - Q_{cond} - Q_{conv} - Q_{rad} \qquad (4.1)$$

The temperature change is a function of the energy generated by chemical reaction and energy losses from conduction, convection, and radiation. We have seen that the time scale and drop size of interest preclude the use of a lumped parameter, zero-dimensional model. Instead, a finite-difference approximation to the conduction equation will be used within the drop. The time-dependent conduction equation in spherical coordinates is:

$$\frac{1}{\alpha}\frac{\partial T}{\partial \theta} = \frac{\partial^2 T}{\partial r^2} + \frac{2}{r}\frac{\partial T}{\partial r} \qquad (4.2)$$

Where $\alpha=k/\rho c$. The spatial derivatives in this equation are discretized with the familiar finite-difference approximation so that the temperature at node **k** is written as:

$$\frac{1}{\alpha}\frac{dT_k}{d\theta} = \frac{T_{k-1} - 2T_k + T_{k+1}}{\Delta r^2} + \frac{T_{k+1} - T_{k-1}}{r\Delta r} \qquad (4.3)$$

The change in temperature with time is obtained using the Crank-Nicolson method [37], which calculates the new nodal temperature, T_k^{j+1}, with the arithmetic average of the derivatives at the current and new time step:

$$T_k^{j+1} = T_k^j + \frac{\Delta\theta}{2}\left[\frac{dT_k}{d\theta}\Big|_j + \frac{dT_k}{d\theta}\Big|_{j+1}\right] \qquad (4.4)$$

The boundary conditions necessary to solve the resulting system of equations are:

$$\frac{dT}{dr} = 0 \qquad at\ r=0$$
$$\rho c V_s \frac{dT_s^j}{d\theta} = Q_{in}^j - Q_{out}^j + Q_{reac}^j \qquad at\ r=R \tag{4.5}$$

where Q_{in} is the rate of energy conducted into the outermost control volume of the drop, at a temperature T_s, from the adjoining control volume, at a temperature T_{s-1}. The finite-difference formulation for this is:

$$Q_{in}^j = 4\pi(R - \frac{\Delta r}{2})^2 k\left(\frac{T_{s-1}^j - T_s^j}{\Delta r}\right) \tag{4.6}$$

The term Q_{out} is energy loss through the film in the form of radiation and either conduction or convection, depending upon the particular model being used (the choice of heat transfer model is discussed further in the following sections). Conduction through the film is calculated from:

$$Q_{cond}^j = 4\pi(R+\frac{\delta^j}{2})^2\ k_{film}\ \frac{T_s^j - T_i^j}{\delta^j} \tag{4.7}$$

The film conductivity is calculated by averaging the water vapor and hydrogen thermal conductivities at the film temperature. The film temperature is an average between the water temperature at the film edge (hereafter referred to as the interface temperature) and drop surface temperature. The film thickness δ increases as hydrogen is produced from the chemical reaction and so this is written as a time dependent quantity.

Convective heat transfer is calculated from the following relation:

$$Q_{conv}^j = 4\pi R^2\ h^j(T_s^j - T_{bulk}) \tag{4.8}$$

The heat transfer coefficient is dependent upon film properties, which are a strong

function of temperature. Because of this, the heat transfer coefficient is recalculated during each time step. The coefficient is obtained from a correlation of experimental data from film boiling on metal spheres; this is discussed further in Section 4.3.

Calculations show that radiation heat transfer becomes comparable to conduction losses as the surface temperature approaches about 600 C. The radiative losses from the drop surface to the film interface are calculated from:

$$Q_{rad}^{j} = 4\pi R^2 \sigma \varepsilon (T_s^{j\,4} - T_i^4) \qquad (4.9)$$

This expression implicitly assumes that the view factor between the drop and film interface is one, which is a good approximation for a thin film. There is no experimental data available for the emissivity of molten lithium [40] so it is assumed equal to one. The nonlinearity of the radiation equation makes it difficult to incorporate into the system of equations generated by the finite-difference approximations. Radiative heat losses are treated in an approximate fashion by calculating the radiative loss from the surface during the current time step **j** by using the temperature from the previous time step, **j-1**. This was found to be an acceptable approach because radiation losses are small compared to convection and conduction losses for the conditions of interest. Time step selection used the criteria that the Fourier number be less than one-half. This is a typical requirement for one-dimensional conduction computations. A schematic is provided in Figure 4.1 to illustrate the geometry of this model and to clarify nomenclature use.

The chemical energy generated in the outermost control volume is calculated from the molar flux of vapor $\mathbf{J_v}$ reaching the drop surface and the energy generated per mole of water **E** :

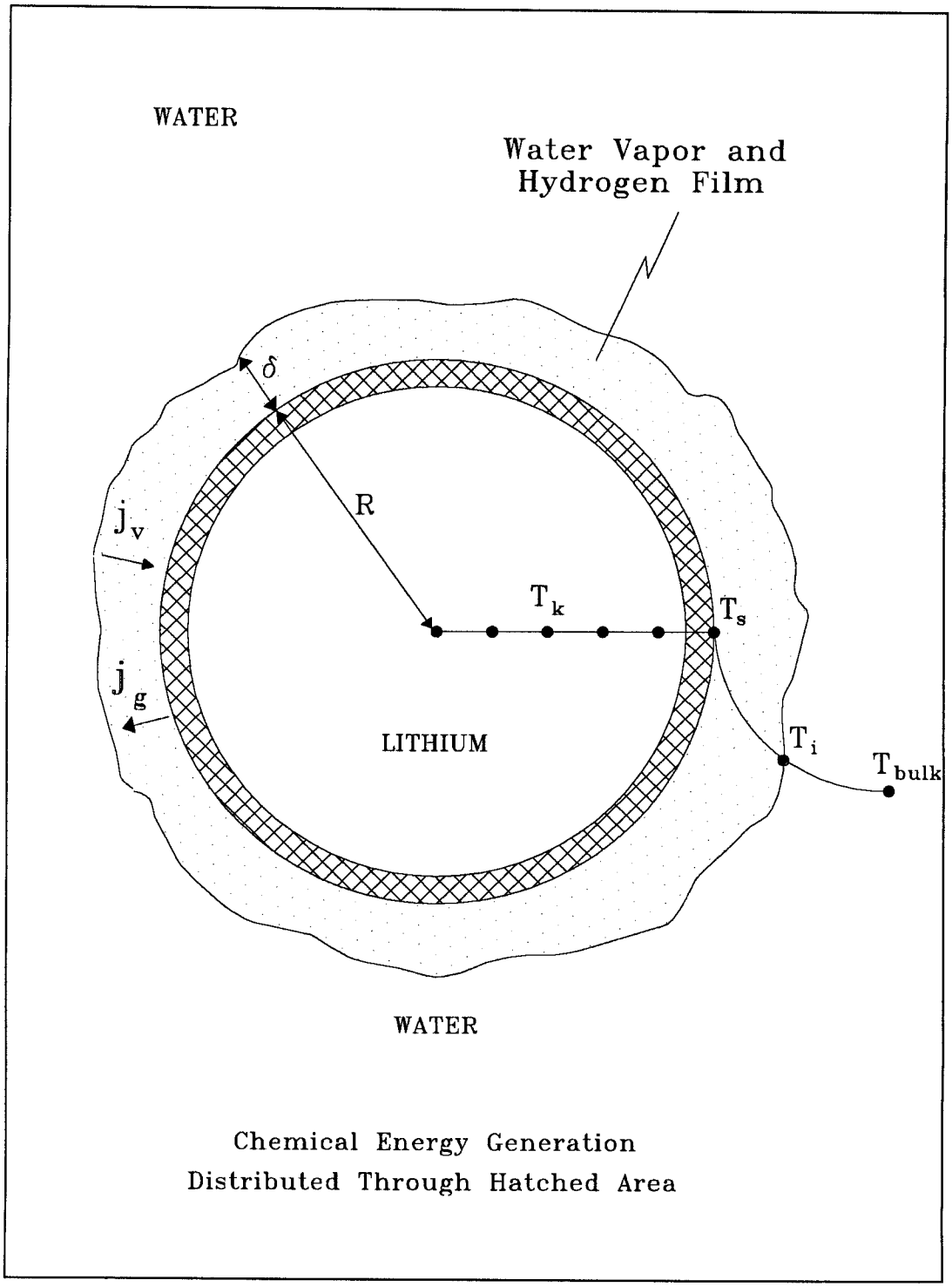

Figure 4.1

Geometry for Chemical Reaction Model

$$Q^j_{reac} = 4\pi R^2 J^j_v E \tag{4.10}$$

This energy is distributed uniformly through the outermost control volume, denoted by the hatched area in Figure 4.1. This region retains the physical properties of lithium throughout the calculation, and the accumulation of reaction products at the drop surface is not considered.

Finally, the volume associated with the mesh point on the drop surface is:

$$V_s = \frac{4}{3}\pi(R^3 - (R-\Delta r)^3) \tag{4.11}$$

The specific heat, thermal conductivity, and density of lithium (**c**, **k**, and ρ, respectively) are all evaluated at the initial drop temperature and then assumed to be constant.

IV.II Diffusion Model for Mass Transfer Across the Gaseous Film

The first model considers a lithium droplet surrounded by a stagnant film. This is used as a starting point for two reasons. First, stagnant diffusion enables the calculation of a minimum heat-up rate for the drop. The rate may be compared to experimental observations of the ignition phenomenon to decide if ignition can take place under these conditions. Second, a portion of the stagnant diffusion model provides a basis for the film boiling mass transfer model that is discussed in section 4.3. We now turn to a description of the mathematical relations for this model and then a discussion of the calculated results.

Referring once again to a stagnant film, the total pressure throughout the film is taken to be constant at 0.1 MPa (atmospheric pressure). Water vapor diffusing across this

film is governed by the following equation [41]:

$$\bar{J}_v = x_v(\bar{J}_v + \bar{J}_g) - nD_{vg}\nabla x_v \tag{4.12}$$

Solution of this equation requires that one specify some relationship between the molar flux of vapor, J_v, and the molar flux of hydrogen gas J_g. This relationship is obtained from the stoichiometry of the chemical reaction. Two possible reactions may be occurring:

$$\begin{aligned} &(\textit{reaction 1}) \quad Li + H_2O = LiOH + \tfrac{1}{2}H_2 \; -.20\ MJ\ /\ mole\ Li \\ &(\textit{reaction 2}) \quad Li + \tfrac{1}{2}H_2O = \tfrac{1}{2}Li_2O + \tfrac{1}{2}H_2 \; -.16\ MJ\ /\ mole\ Li \end{aligned} \tag{4.13}$$

In chapter one, it was explained that the first reaction is dominant when excess water is present. For similar reasons, the second reaction dominates under the condition of excess lithium (see the reaction paths in Chapter 1). In our reaction model the lithium drop is surrounded by water, seemingly an excess of water for reaction, but the water vapor pressure at the drop surface is assumed to be zero, an apparent excess of lithium. It is unclear which of these two reactions is preferred or if one is predominant during one stage of the reaction while the other dominates at other times. The approach here is to solve Equation 4.12 for both cases and determine if the reaction path has a profound effect on the calculated temperature transient. The molar balances between vapor consumed by reaction and hydrogen production are:

$$\begin{aligned} &(\textit{reaction 1}) \quad \bar{J}_g = -\tfrac{1}{2}\bar{J}_v \\ &(\textit{reaction 2}) \quad \bar{J}_g = -\bar{J}_v \end{aligned} \tag{4.14}$$

The large temperature difference between the metal surface and water suggests that

assuming an isothermal film is inappropriate. Instead, the film temperature is assumed to vary radially with the following form:

$$\frac{T(r)}{T_s} = \left(\frac{r}{R}\right)^y \tag{4.15}$$

where the exponent is calculated from the temperatures at the metal surface and film interface. The total molar concentration of gas and vapor, **n**, and the diffusion coefficient, $\mathbf{D_{vg}}$, are functions of temperature. The value of **n** is calculated from the perfect gas law while the diffusion coefficient is found with the following relation [42]:

$$D_{vg}(T) = D_o\left(\frac{T}{T_o}\right)^{1.75} \tag{4.16}$$

These relationships are used to express the diffusion coefficient and molar concentration as a function of radial position within the film. Using Equations 4.14-16, Equation 4.12 can be integrated and expressions for the molar flux of water vapor to the drop surface are obtained for each reaction path. For reaction 1:

$$J_v = -\frac{D_o P}{\Re T_s}\left(\frac{T_s}{T_o}\right)^{1.75} \frac{(1+.75y)}{R_s^{2+.75y}\left(R_i^{-1-.75y} - R_s^{-1-.75y}\right)} 2\ln\left(\frac{1-\frac{1}{2}x_{vi}}{1-\frac{1}{2}x_{vs}}\right) \tag{4.17}$$

and for reaction 2:

$$J_v = \frac{D_o P}{\Re T_s}\left(\frac{T_s}{T_o}\right)^{1.75} \frac{(1+.75y)}{R_s^{2+.75y}\left(R_i^{-1-.75y} - R_s^{-1-.75y}\right)} (x_{vi} - x_{vs}) \tag{4.18}$$

To calculate this flux, all that remains to be determined is the temperature of the film interface. This temperature is needed to calculate the exponent in Equation 4.15, and it leads directly to a value for the water vapor pressure at the interface. It is important that this temperature is evaluated accurately because the vapor pressure at the interface

is essentially the driving pressure for the reaction. One can be sure that the interface temperature is somewhere between the bulk water temperature, $\mathbf{T_{bulk}}$, and the saturation temperature at the local pressure. However, a simple calculation suggests that this temperature is very close to the bulk water temperature. Since we are interested in a stagnant film and a time scale that is very short, one may consider the interface to be between two semi-infinite bodies. In this case, the contact temperature between the two is given by [37]:

$$T_c = \frac{T_{film}\sqrt{k\rho c_{film}} + T_{bulk}\sqrt{k\rho c_{bulk}}}{\sqrt{k\rho c_{film}} + \sqrt{k\rho c_{bulk}}} \tag{4.19}$$

The product $\mathbf{k\rho c}$ is much larger for liquid water than it is for the gaseous film and so the contact temperature is very near $\mathbf{T_{bulk}}$. With the interface temperature near $\mathbf{T_{bulk}}$, one finds that heat conducted from the film interface into the water is small, so this is neglected.

The previous analysis indicates that very little energy is conducted into the liquid water. It is then reasonable to assume that all energy conducted from the drop to the film interface contributes to evaporation at the interface. The evaporation rate is simply the rate of energy loss through the film divided by the heat of vaporization. It is convenient to write the evaporation rate as a molar flux per drop surface area so that it may be compared with the diffusion flux:

$$J_{evap} = \frac{1}{4\pi R^2}\frac{Q_{cond}+Q_{rad}}{M_v h_{fv}} \tag{4.20}$$

In practice, radiative losses are much smaller than conduction losses for the temperatures of interest. In this expression, the energy necessary to heat the water from the bulk

temperature to the saturation temperature has been neglected in comparison to the heat of vaporization.

The diffusion rate of water vapor to the metal surface may now be compared with the evaporation rate of water at the interface. We will look at how these rates vary as the interface temperature changes. Figures 4.2a and 4.2b provide plots for drop temperatures of 200 C and 600 C, the lower and upper limits of injection temperature for the experiment. A drop radius of 10 mm and initial film thickness of 1 mm are chosen for these calculations. It is seen that both the evaporation and diffusion rates of the 600 C drop are larger than those of the 200 C drop. As the metal temperature rises, the evaporation rate increases faster than the diffusion rate. This effect should become more pronounced as the metal temperature increases beyond 600 C and radiation heat transfer becomes appreciable.

Figures 4.2a and 4.2b show that for the majority of initial conditions (lithium/water initial temperatures) used in the experiment, the diffusion rates for each reaction path are about the same. It is also seen that the evaporation rate exceeds the diffusion rate for these conditions. However, these rates are instantaneous values and they will change if the evaporation and diffusion rates are not balanced; i.e., the boundary conditions under which the calculations were made are changing. If the evaporation rate exceeds the diffusion rate, the vapor pressure at the interface builds, increasing the diffusion rate, until the two are equalized. In essence, the diffusion rate moves up along the curve until it intersects the evaporation rate (it is the vapor pressure that is actually changing, rather than the interface temperature). This reasoning indicates that the reaction rate at the drop surface is maximized by assuming it equal to the evaporation rate. The evaporation rate

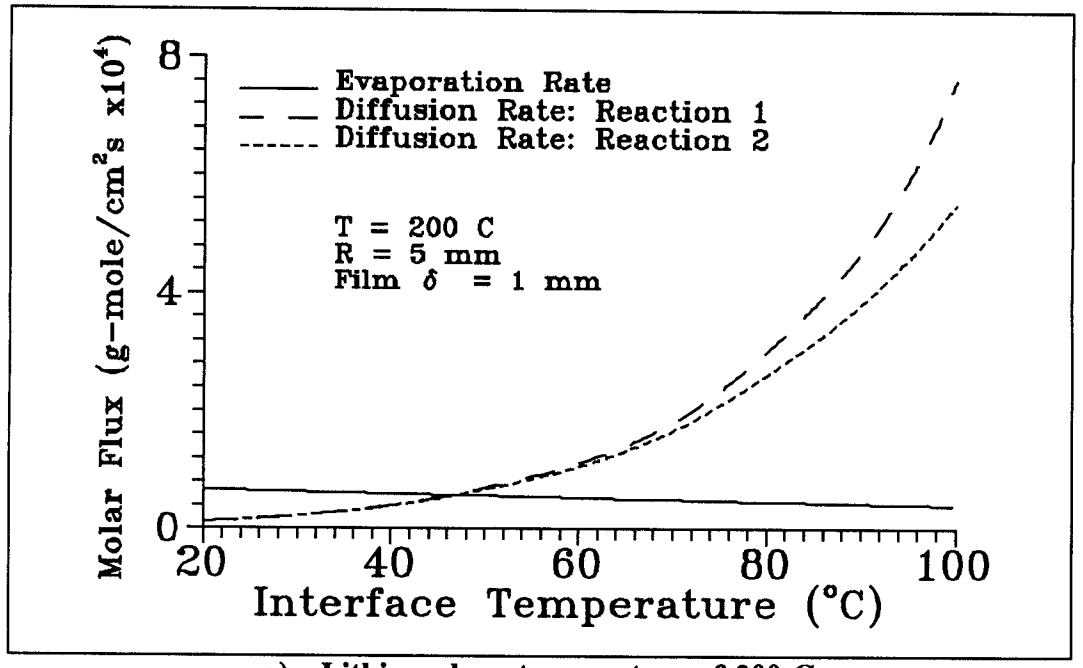

a) Lithium drop temperature of 200 C

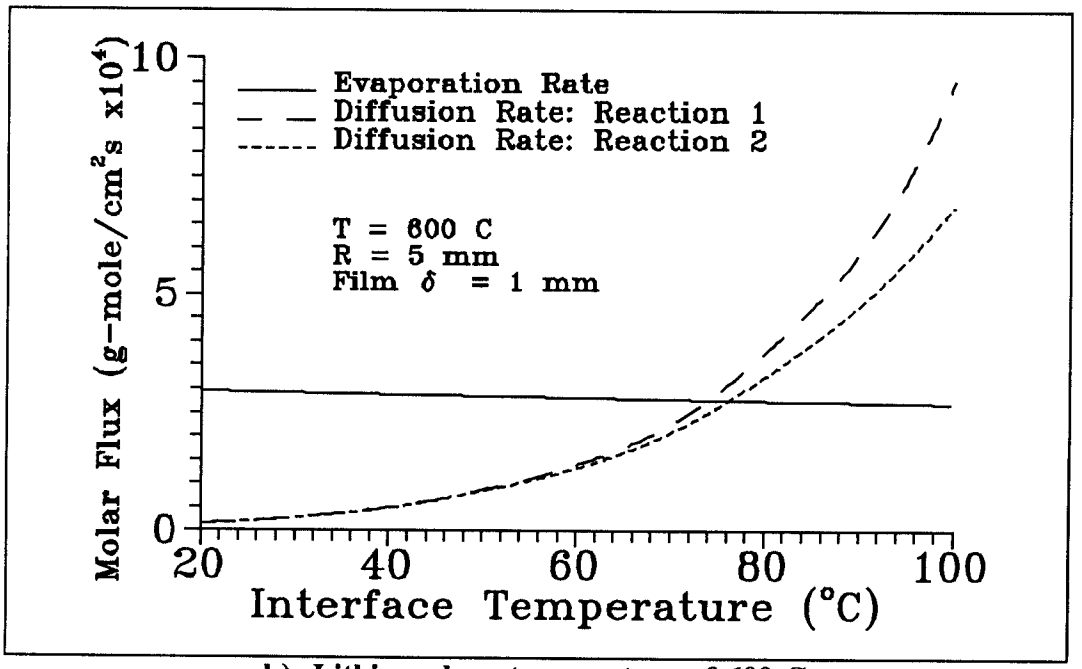

b) Lithium drop temperature of 600 C

Figure 4.2
Molar Flux vs Interface Temperature for Two Drop Temperatures

is maximized by assuming all heat loss through the film contributes to evaporation. For the calculations to follow, *the reaction rate at the drop surface is conservatively set equal to the evaporation rate.* This defines a maximum heat-up rate for the drop with stagnant diffusion, the original goal for the analysis in this section.

One final element remains to be incorporated into this reaction model: calculation of the size of the gaseous film as a function of time. The film thickness is an important parameter in governing the diffusion rate and heat loss from the drop surface. The size of the film changes with time and the rate of this change is dependent upon reaction rate (as well as reaction path). It is most convenient to compute film size in terms of the total number of moles of gas in the film, N_t. The rate of change in the total number of moles of gas is simply the difference between the rate at which water vapor and hydrogen are produced and the rate of vapor consumption:

$$\frac{dN_T}{d\theta} = 4\pi R^2 (J_{evap} + J_g - J_v) \tag{4.21}$$

It has already been stated that the vapor generation is governed by the rate at which energy is conducted to the film interface. From the stoichiometric relations in Equation 3.14, relationships between hydrogen production and vapor consumption for each reaction path are known. Using these expressions, the film growth rate can be written as:

$$\begin{aligned} (\textit{reaction 1}) \quad & \frac{dN_T}{d\theta} = 4\pi R^2 (J_{evap} - \tfrac{1}{2} J_v) \\ (\textit{reaction 2}) \quad & \frac{dN_T}{d\theta} = 4\pi R^2 J_{evap} \end{aligned} \tag{4.22}$$

The major difference between the two reaction paths is now evident. When LiOH is the primary reaction product (reaction 1), the consumption of two water vapor molecules results in the production of only one hydrogen molecule. With this reaction, if the diffusion rate is more than twice the evaporation rate, the film contracts. Figures 4.2a and 4.2b show that this situation does not exist for water temperatures used in the experiment, less than 70 C.

The total number of moles of gas in the film at the new time step, N^{j+1}, is the sum of the moles already in the film and the moles reacting in the current time step:

$$N_t^{j+1} = N_t^j + \frac{dN_t^j}{d\theta}\Delta\theta \qquad (4.23)$$

The film thickness is then found by calculating the volume of gas present using the equation of state for a perfect gas, assuming atmospheric pressure and a gas temperature equal to T_{film}.

Sample calculations with this model are plotted in Figures 4.3 and 4.4 for a 10 mm diameter drop at 400 C. The initial film thickness chosen for these calculations is 0.1 mm, and reaction 1 governs the energy generation and film growth rates. Figure 4.3 shows the temperature profile across the drop during a time span of 0.5 s. The reaction proceeds slowly enough that the temperature profile remains nearly flat. Figure 4.4 is a plot of the surface temperature and film thickness as a function of time. Note that both grow very rapidly at first and then slow to a somewhat linear increase. This is expected because, as the reaction proceeds, the thickening film inhibits heat transfer from the drop surface to the film interface. There is a corresponding reduction in the evaporation rate and the rapid temperature increase cannot be sustained. The trends

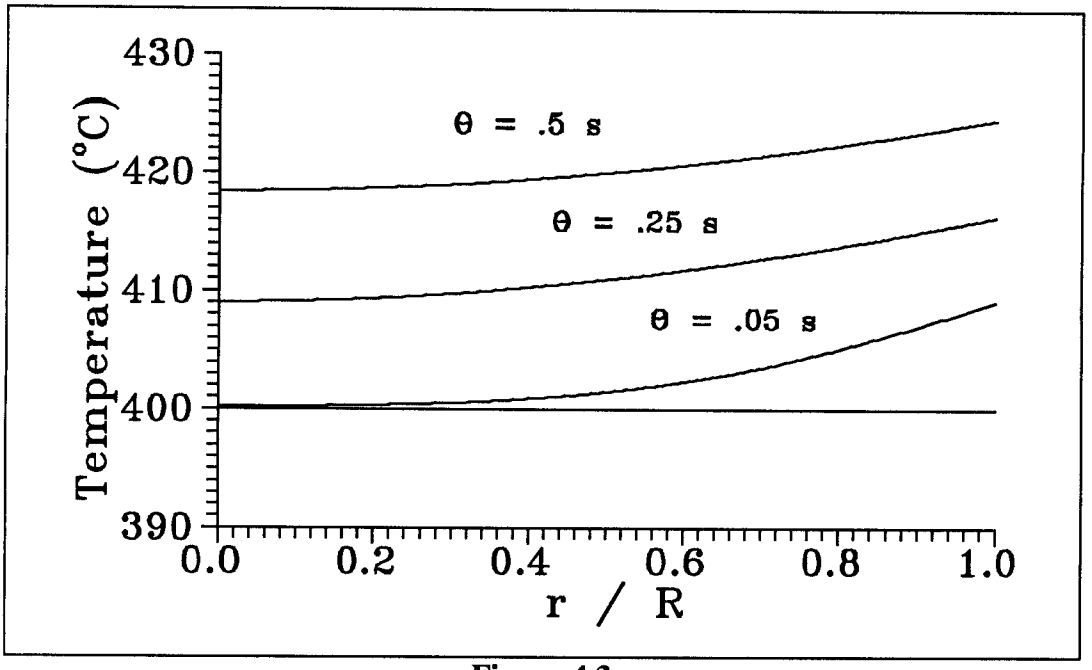

Figure 4.3

Radial Temperature Distribution of 10 mm Diameter Droplet

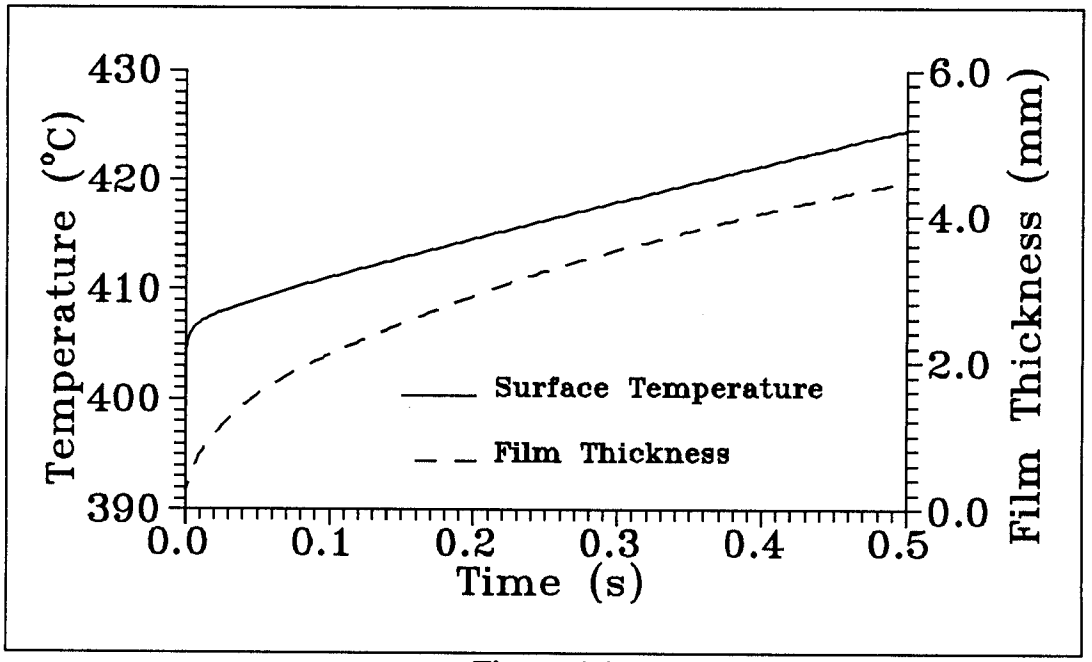

Figure 4.4

Film Thickness and Surface Temperature of Drop Versus Time

shown are typical, and they are not sensitive to input parameters such as drop diameter, initial film thickness, and initial temperature. Calculations with reaction 2 are similar though the temperature increase is smaller and the film growth rate is greater.

The purpose of the analysis in this section was to examine the possibility of lithium drop ignition when heat and mass transfer processes are minimized. The preceding calculations suggest that this is very unlikely under stagnant conditions. When stagnant diffusion and conduction are the dominant mass and heat transfer processes, the rate of vapor transport to the drop surface is insufficient for the surface to heat up to the high temperatures expected for ignition. We will now turn to a model where the mass transfer rate of vapor is expected to be much higher; a model that should be more representative of the conditions under which ignition occurs.

IV.III Film Boiling Heat and Mass Transfer Model

The previous analysis arrived at a lower bound estimate of the rate of temperature increase in the drop by assuming a diffusion controlled reaction rate under stagnant conditions. The model in this section considers the enhanced heat and mass transfer that exists under the condition of film boiling. Included in the analysis are forced convection effects caused by drop motion.

The first task is determining the heat transfer coefficient from the drop surface to the water as a function of lithium and water temperature and drop velocity. This is used to calculate a corresponding mass transfer rate of water vapor to the metal surface. Once these parameters are determined, the finite-difference model may again be used to calculate the temperature history of the drop.

The heat transfer coefficient is calculated from a correlation of the experimental data of Dhir and Purohit [43]. Their experiments involved the study of film boiling on small metallic spheres in saturated and subcooled water. Their correlation of test results for saturated film boiling with forced convection takes the following form:

$$\frac{hd}{k_v} = Nu_o + .8(Re)^{\frac{1}{2}} \tag{4.24}$$

where:

$$Re = \frac{dv\rho_f}{\mu_f} \tag{4.25}$$

and

$$Nu_o = .8\left(\frac{g_o\rho_v(\rho_l-\rho_v)i_{fg}d^3}{\mu_v k_v(T_s-T_{sat})}\right)^{\frac{1}{4}} \tag{4.26}$$

A saturated film boiling correlation has been chosen instead of a subcooled one because of the presence of hydrogen. In saturated boiling, the vapor generated at the metal surface does not condense because the surrounding water is unable to absorb the energy. The vapor blanket builds on the metal surface until buoyancy forces and convection pull portions of it away as bubbles. The situation is analogous with hydrogen present and so Equation 4.24 is more appropriate than a correlation for subcooled film boiling. To evaluate $\mathbf{Nu_o}$ the physical properties of the gaseous film (denoted by the subscript v; the film is entirely water vapor in Dhir's work) are evaluated at the film temperature. For our calculations these are considered to be an average of the properties of hydrogen and water vapor at the film temperature. In addition, the term $\mathbf{T_{sat}}$ is replaced with $\mathbf{T_{bulk}}$ to account for subcooling.

The heat transfer coefficient found with the above relations is now used to calculate a mass transfer coefficient. Using the analogy between heat and mass transfer,

a mass transfer coefficient may be written as [44]:

$$G = \frac{h_v}{\rho_v c_{pv}} \left(\frac{Pr}{Sc}\right)^{\frac{2}{3}} \tag{4.27}$$

where the Prandtl and Schmidt numbers are defined as:

$$Pr = \frac{c_{pv}\mu_v}{k_v} \quad and \quad Sc = \frac{\mu_v}{D\rho_v} \tag{4.28}$$

To make use of this mass transfer coefficient the diffusion equation is solved in rectangular coordinates. Beginning with Equation 4.12, the molar flux of vapor to the metal surface is written as :

$$J_v = \frac{-nD_{vg}}{(1 - \frac{1}{2}x_v)} \frac{\partial x_v}{\partial z} \tag{4.29}$$

Where the stoichiometry of reaction one has been used to eliminate J_g. The analysis for the case of stagnant diffusion showed that there was little difference in the calculated heat-up rate between reactions one and two. This is particularly true for this model because the heat and mass transfer rates are not explicitly calculated from the film thickness. Therefore, this model employs the diffusion equation and energy generation for reaction one, but the calculated values of the molar flux are considered representative of both reactions. Equation 4.29 is now integrated to provide the following:

$$J_v = \frac{2nD_{vg}}{\delta} \ln(1 - \frac{1}{2}x_v) \tag{4.30}$$

Where x_v is the molar concentration of water vapor at the edge of the diffusion layer, a distance δ from the metal surface. This distance is less than the film thickness because of the turbulent nature of film boiling. Integration of Equation 4.29 was accomplished by assuming the molar density of the film **n** and the diffusion coefficient **D** may be

treated as constants evaluated at the film temperature. The thickness of the diffusion layer is unknown but it is related to the diffusion and mass transfer coefficients [44]:

$$G = \frac{D_{vg}}{\delta} \tag{4.31}$$

It is now possible to eliminate the diffusion layer thickness from the expression for the molar flux:

$$J_v = 2n \ln(1 - \tfrac{1}{2}x_v)\left(\frac{h_v}{\rho_v c_{pv}}\right)\left(\frac{Pr}{Sc}\right)^{\frac{2}{3}} \tag{4.32}$$

This is the relationship used to calculate the flux of water vapor to the metal surface for the condition of film boiling. This flux is proportional to the film boiling heat transfer coefficient and increases with Reynolds number (through the heat transfer coefficient correlation). The water vapor concentration at the edge of the diffusion layer, x_v, is assumed equal to one. Finally, it is noted again that all physical properties and dimensionless groups associated with the gaseous film are calculated from an average of the physical properties for hydrogen and water vapor, evaluated at the film temperature.

IV.IV Results and Discussion

The mass transfer model developed here is a rudimentary one. Even so, there are several independent parameters within the model that are needed to calculate the drop temperature transient. These are identified as the drop diameter, velocity, initial temperature, and bulk water temperature. Presentation of calculated results begins by examining the sensitivity of drop heat-up rates to variations in these parameters. This is to identify parameters that have a strong influence on the transient. Also, we wish to

show that the model behaves correctly. In these sensitivity studies, parameters are varied about values that have been observed during (or assigned for) the scoping tests. After this, the model is used to compute the time dependent temperature profiles of a droplet with two different initial temperatures. These profiles are then discussed in the context of scoping test results.

Figure 4.5a is a plot of drop surface temperature versus time for three drop sizes. It shows how a reduction in drop diameter raises the rate of temperature increase. This is due to a larger surface to volume ratio for smaller drops. In Figure 4.5b, the surface temperature of a 10 mm diameter drop versus time is plotted for three drop velocities. The Reynolds number increases with drop velocity, which enhances the mass transfer rate of water vapor to the metal surface. The effects of this increased mass transfer are clearly seen; the heat-up rate increases with drop velocity. The effect of velocity is not a strong one because the Nusselt number increases with velocity raised to the one-half power.

Figure 4.6a shows how the bulk water temperature affects the drop heat-up rate. Hotter water increases the reaction rate, as one would expect. The denominator of Equation 4.26 contributes to the temperature dependence. The reader is reminded that though we have used a heat transfer correlation for saturated film boiling because of hydrogen production, the bulk water temperature is used in place of $\mathbf{T_{sat}}$. This means that the calculated Nusselt number increases with bulk water temperature, but the effect is small. Most of the Nusselt number increase is from an increase in Reynolds number. As the water temperature increases, the viscosity of water decreases, which raises the Reynolds number.

For all preceding computations, it is assumed that **LiOH** is the only reaction

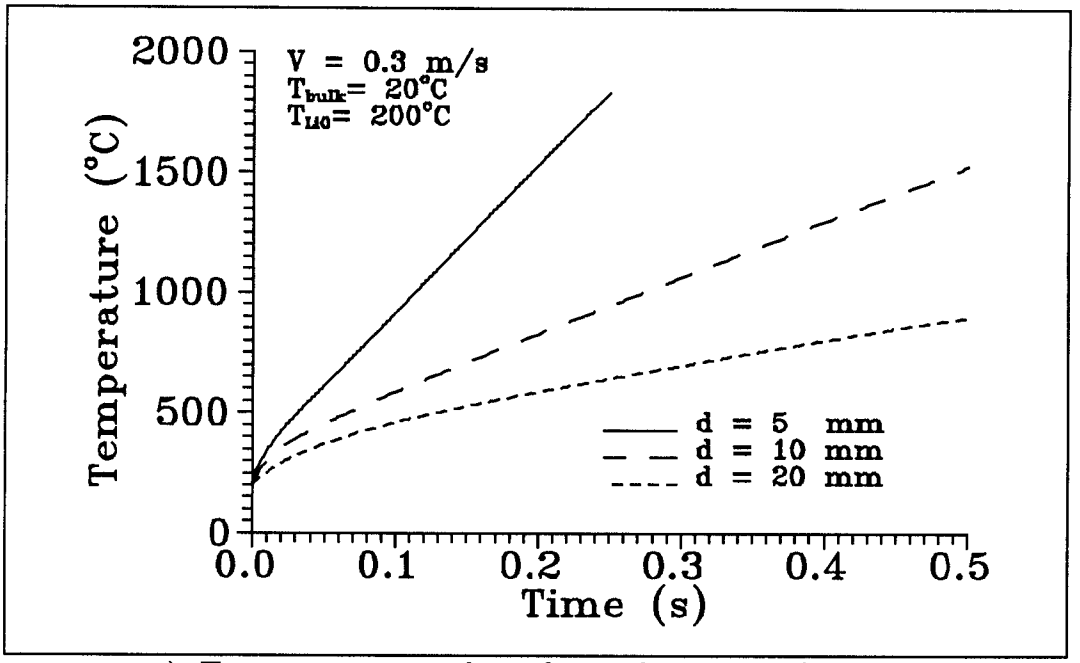

a) Temperature transients for various drop diameters

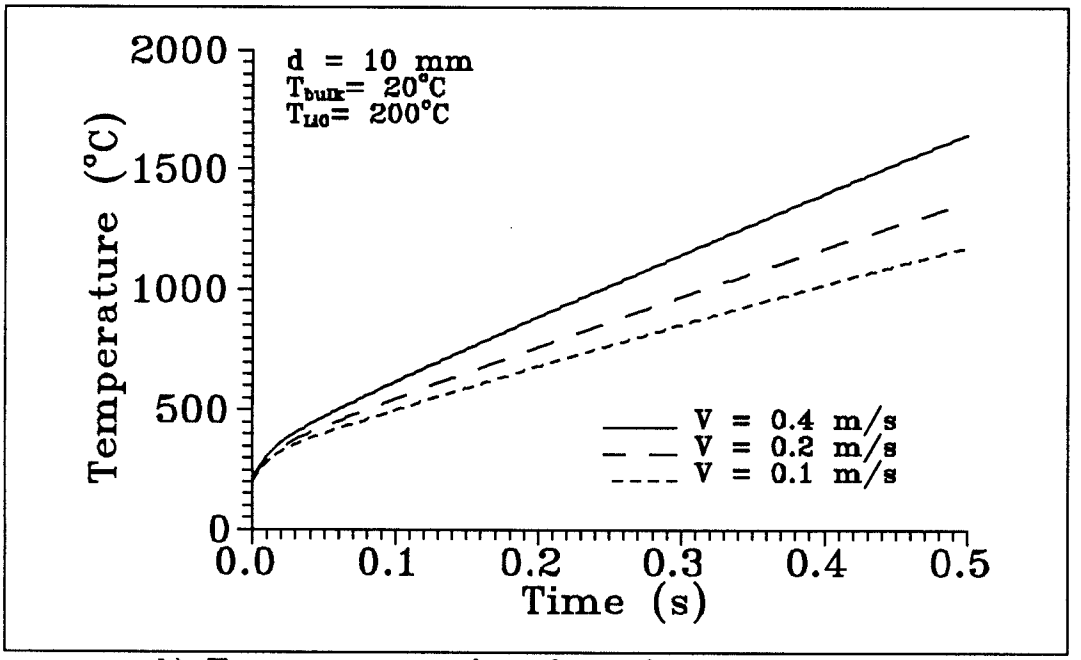

b) Temperature transients for various drop velocities

Figure 4.5

Calculated Lithium Drop Surface Temperatures versus Time

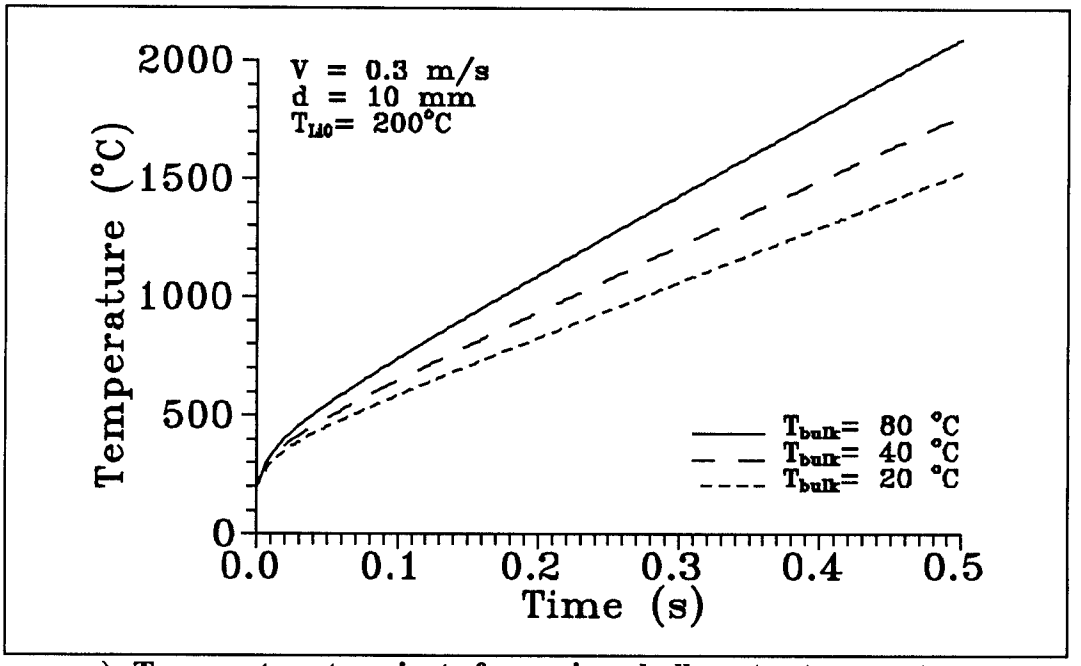

a) Temperature transients for various bulk water temperatures

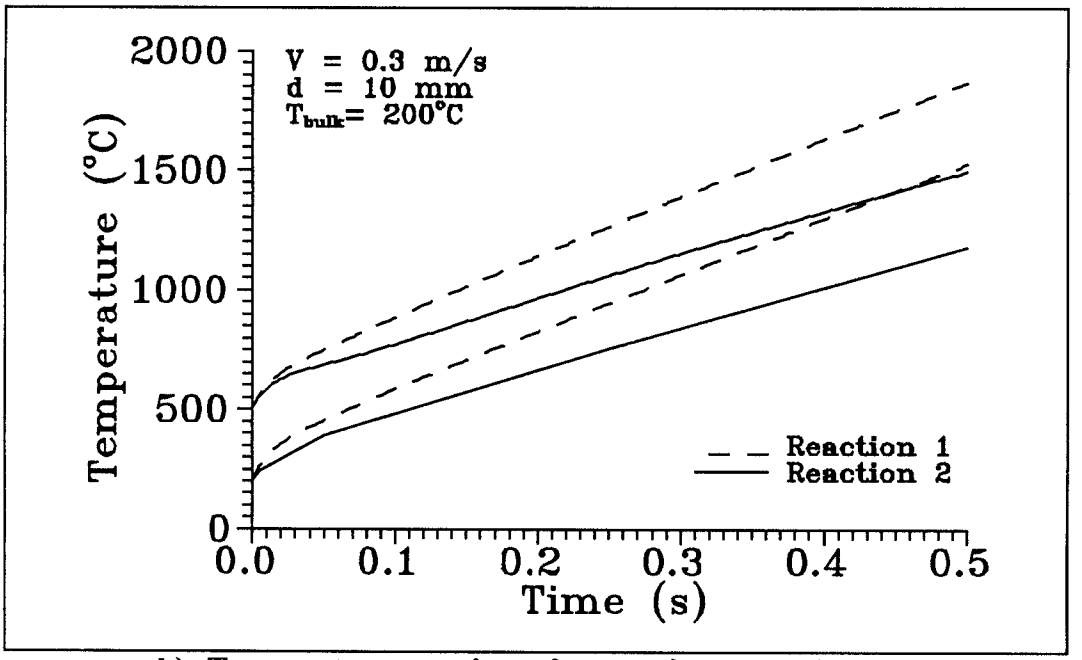

b) Temperature transients for reaction paths 1 and 2

Figure 4.6

Calculated Lithium Drop Surface Temperatures versus Time

product. Also, ten mesh points are used to compute conduction heat transfer across the drop, and the chosen time-step is 5 ms (except for the 2.5 mm drop, where the time step is 1 ms). Note that the boiling point of lithium is about 1350 C at atmospheric pressure.

Figure 4.6b has been included to illustrate how the reaction path affects the drop temperature transient. The energy produced per g-mole of lithium for reaction path 2 is only 77% that of reaction 1. The effect is that the drop heats up more slowly with reaction path 2 than with path 1, given the same reaction rate. The temperature difference between the two paths grows with time. It is believed that reaction path 1 is the dominant path in our experiments, for reasons outlined earlier, and this path is used in all subsequent calculations.

Figure 4.6b also shows that for a given reaction path, the rate of temperature increase is the same for both initial metal temperatures. Lithium drops with higher injection temperatures are expected to reach the boiling point sooner than drops at lower temperatures. This is an important point, which we will return to shortly and relate with scoping test results.

The previous figures illustrate that reaction rates calculated with the film boiling model are much greater than those calculated on the basis of stagnant diffusion. The calculated molar flux of vapor to the metal surface for film boiling ranges from around 40 to nearly 300 times that computed for the stagnant diffusion model. In addition, the flux does not decline as the vapor film grows from hydrogen production, and so the reaction rate remains high during the entire transient. This contrasts with the stagnant diffusion model, where a growing hydrogen film slows the reaction rate. For this reason, computations are never carried out past 0.5 s. At this point in the transient, the calculated

film thickness has grown to two or three centimeters, and the film boiling model is inappropriate. This is discussed further after computed droplet temperature distributions are presented.

Now transients with two different initial lithium temperatures are considered. For these calculations, the drop diameter and velocity are set equal to 10 mm and 0.3 m/s, respectively. These values are chosen because they are indicative of those found during scoping tests. Figure 4.7 contains plots of radial temperature distributions as a function of time for initial drop temperatures of 200 C and 500 C. These temperatures are chosen because they represent the lower and upper limits of initial metal temperature. The graphs show that the temperature profiles change more quickly and have larger radial gradients than profiles for stagnant diffusion. Figure 4.7a shows that after an elapsed time of 0.5 s, most of the drop remains below the lithium boiling point. This differs from the drop with an initial temperature of 500 C, shown in Figure 4.7b, which is near or above the boiling point at this time.

It is recognized that this film boiling model is applicable for only a short time after injection. This is because the model does not consider the growing hydrogen bubble around the droplet. The correlation used to compute a film boiling heat transfer coefficient is derived from experiments where steam generated by film boiling is constantly leaving the sphere. A relatively thin film (on the average) of vapor is maintained around the sphere under these conditions, and a thinner gaseous film correlates with higher conduction heat transfer.

This physical picture of film boiling without a chemical reaction differs somewhat from experimental observations of the lithium/water reaction. The reaction looks much

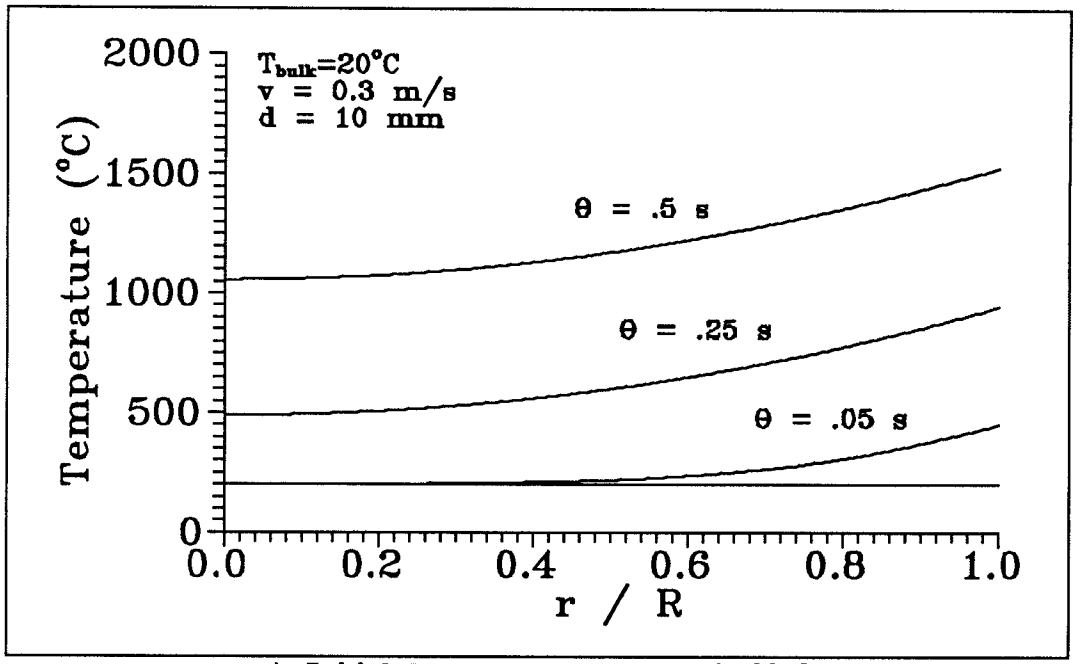

a) Initial droplet temperature of 200 C

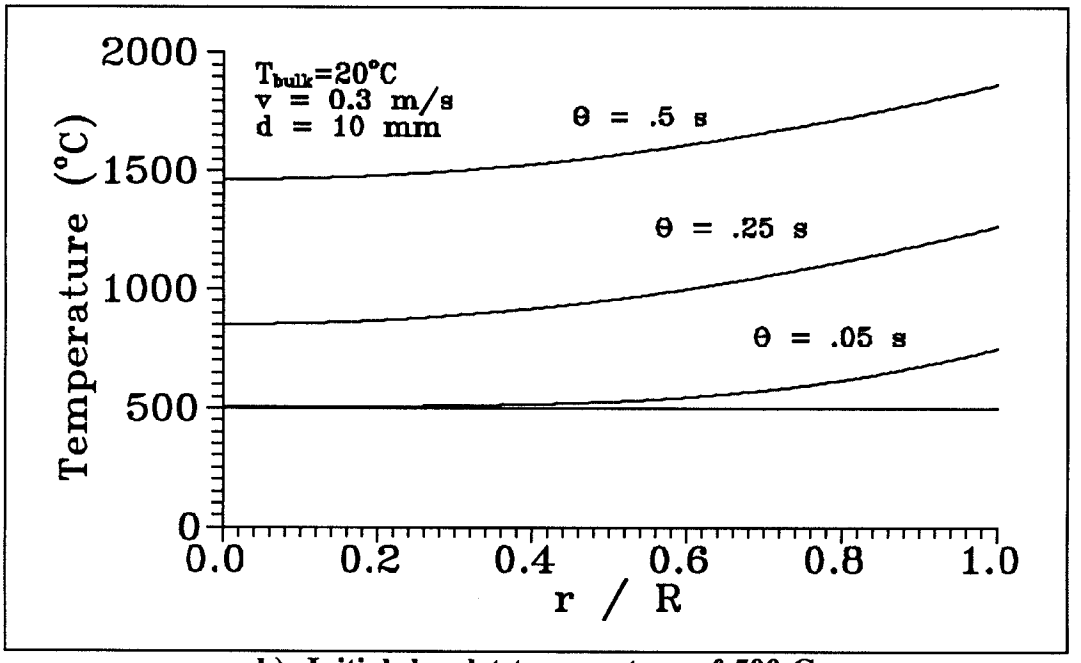

b) Initial droplet temperature of 500 C

Figure 4.7

Radial Temperature Distributions of Lithium Droplet

like film boiling during drop formation and early stages of its travel upward. A thin gaseous layer covers the drop, which is presumably a mixture of hydrogen gas and water vapor. However, as the reaction proceeds, and the drop rises a few centimeters from the injection point, the gaseous film around the drop develops into a bubble. The lithium is carried further toward the water surface, sitting at the base of the bubble. The lithium and gas bubble are rarely seen to separate from one another.

At this point, it is useful to summarize pertinent findings of the numerical analyses and scoping tests:

(1) The numerical model showed that droplets with higher initial temperatures reach the boiling point earlier. Also, the extent of reaction necessary to raise the drop to such a high temperature is greater for drops with lower initial temperatures. Comparing a high initial temperature to a low one, one can say that more hydrogen gas will surround the low temperature drop when it reaches the boiling point.

(2) Scoping test results revealed that explosive reactions were much more likely for higher injection temperatures. These explosions occurred soon after injection. A temperature threshold was found, above which explosive reactions become much more likely. It was noticed that for nonexplosive tests, most lithium drops were glowing orange before reaching the water surface. These drops are seen to be surrounded by a large gas bubble.

What conclusions can be drawn by combining these numerical analyses and results of the scoping experiments? A necessary condition for ignition is proposed from these results: *If a significant portion of the drop reaches the saturation temperature before the film grows enough to inhibit further mass transfer, ignition occurs.* This is likely only

when initial drop temperatures are high. Also, higher water temperatures make explosive reactions more probable, but the effect is less pronounced than the trend seen for an increase in metal temperature. For a drop injected at lower temperature, a relatively large hydrogen bubble surrounds the metal when it reaches the boiling point. This inhibits an explosive reaction. This is consistent with computations using the film boiling model and with scoping test data. The important point here is not how much boiling is necessary to trigger an explosive reaction. The numerical models developed here lack the sophistication necessary to predict this. We have simply compared the observations from experiments with general trends predicted by the numerical models in an effort to explain the physical mechanisms at work.

To further illustrate that trends revealed by the numerical model compare well to experimental findings, another set of computations are performed. The film boiling model is used to calculate the initial lithium and water temperatures necessary to bring the drop surface to the boiling point in 0.25 s. The boiling point has been identified as an important ignition criteria. We would like to see if the numerical model will show the same trends as experimental data plotted in Figure 3.3. Choosing an interval of 0.25 s is arbitrary in part, but it is chosen with some physical reasoning. First, the film boiling model is valid for an interval less than 0.5 s, as previously discussed. Furthermore, calculations show that the film thickness is around 25 mm after 0.25 s. This is larger than what has been observed just prior to an explosion during experiments. In addition, the interval for calculations should not be much shorter than 0.25 s because explosions typically occur around 0.5 s after injection. Strong explosions occur earlier, near 0.25 s, and weak ones occur after 0.5 s. This choice of elapsed time is a compromise. Again,

these computations are intended to show general trends with the numerical model.

Parameters selected for the calculations are: drop diameter of 10 mm; time step of 5 ms; ten mesh-points; and reaction path 1. The drop velocity is not a well known parameter, but it influences the drop heat-up rate. Therefore, two velocities have been chosen to provide an indication of its influence on the results. Velocities of 0.3 m/s and 0.4 m/s represent a best estimate of the range observed in experiments. Results of the computations are shown in Figure 4.8. Experimental data from Figure 3.3 has been included in this plot to facilitate comparisons between computations and experimental findings. It is seen that trends in the numerical results correspond well to experimental data. Given the time limit of 0.25 s, higher initial metal temperatures permit the drop surface to reach the boiling point at lower water temperatures. These results add validity to the proposal that ignition is triggered by a large vapor pressure in the metal droplet, and that this must occur before hydrogen generation slows the reaction rate.

The results of experiments with sodium (see Fig. 2.14) provide another indicator of the validity of our hypothesis. The data clearly shows that the reaction rate at the nozzle is about 100 times the rate in the bubble. At the nozzle, the gas layer surrounding the metal is small, and sodium/water reaction rates are high. This corresponds with our physical picture of the lithium/water reaction during early stages. The reduced sodium/water reaction in the bubble compares well with calculations made using the stagnant diffusion model.

A brief note is made concerning this set of calculations. It is recognized that

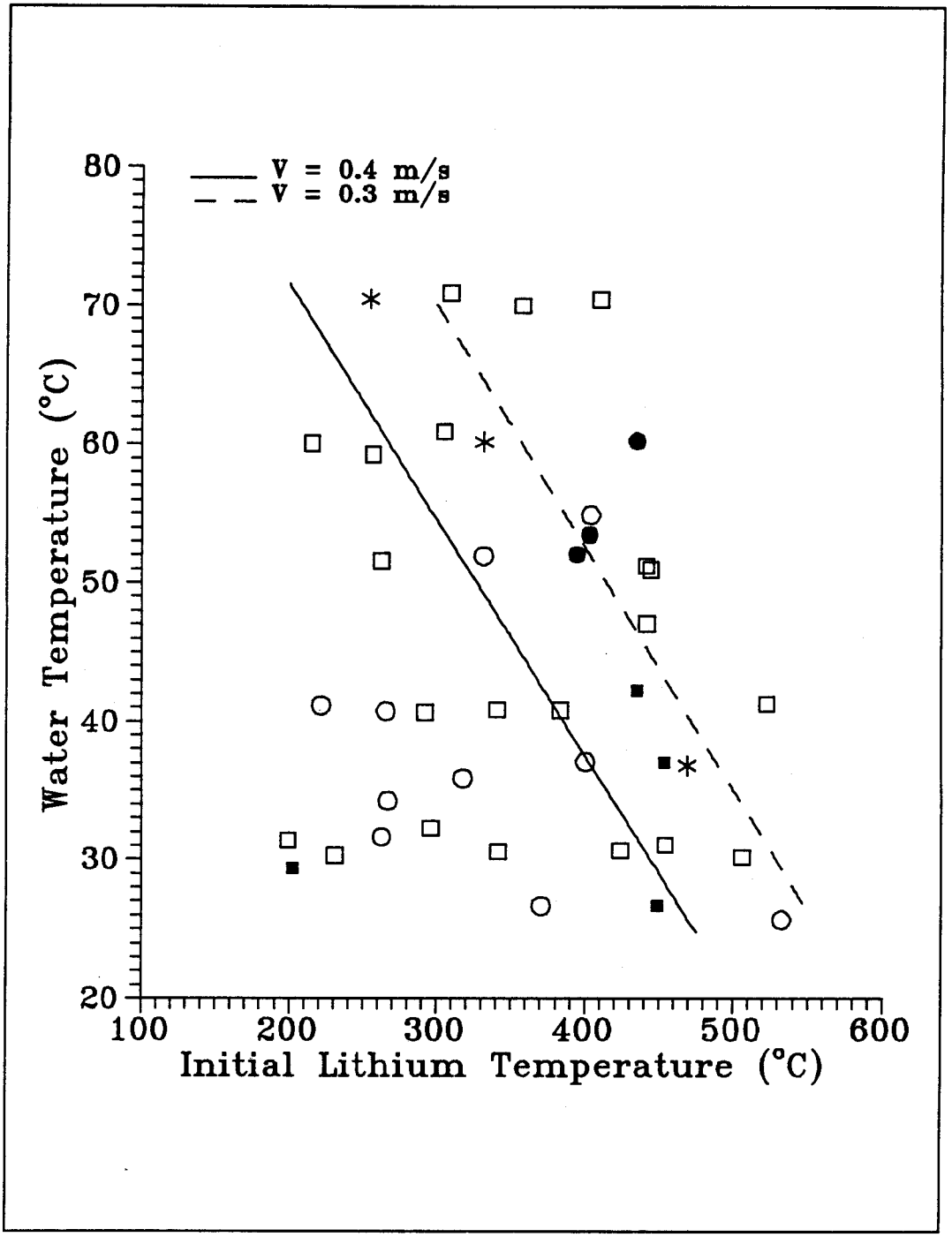

Figure 4.8

Calculated Initial Conditions for the Surface of a 10 mm Diameter Lithium Drop Surface to Reach the Boiling Point in 0.25 s

choosing a different time scale would shift the plotted curves. They would shift downward, to lower reactant temperatures, if the time scale is shortened, and shift up if the time scale were lengthened. Similar effects would be observed if the drop diameter were varied. Still, the parameters chosen for these calculations are representative of experimental tests, and the shape and slope of the curves would remain relatively invariant. It seems clear that our hypothesis, which relates boiling and explosive reactions, could have some physical significance.

To this point, analysis has focused entirely on how chemical energy generation causes significant vaporization in the drop. However, the role of molten-metal fragmentation in explosive metal/water reactions was mentioned frequently in the literature review of chapter two. Examining the scoping test results in that context is certainly just as sound as studying temperature transients. For completeness, the topic of molten-metal fragmentation is briefly discussed.

IV.V Droplet Fragmentation

Our analysis of the metal ignition phenomenon has focused on temperature excursions in the drop resulting from chemical reaction, and how this explains the experimental finding of a temperature threshold for explosive reactions. However, the literature review in chapter two showed that explosive metal/water reactions may result in the absence of chemical reactions. In these instances, a dispersion mechanism increases the metal surface area and the sudden release of thermal energy results in a pressure event, i.e., vapor explosion. Our interest here is not in this dissipation of thermal energy, but rather the dispersion process that precedes it. We are considering the possibility that

some fragmentation mechanism increases the area available for chemical reaction, prompting a sudden increase in the overall reaction rate, which results in an explosive production of steam and gaseous reaction products. This mechanism would be distinctly different from dispersion caused by boiling within the drop, which was proposed in the previous section. Since molten-metal fragmentation has been observed in experiments closely resembling this lithium/water experiment [35], we must address the issue that the recorded pressure events are linked to this phenomena instead of the temperature transients discussed earlier.

Much of the research that examines the causes of vapor explosions focuses on the role of boiling in precipitating fragmentation [16,30,45,46]. Two types of boiling are usually considered, film boiling and transition boiling. Film boiling is characterized by relatively high heat fluxes, so that a continuous vapor film separates coolant from the metal surface. In transition boiling, the metal surface is in contact with both liquid and vapor because the heat flux from the metal surface is insufficient to maintain a continuous vapor film. Transition boiling is regarded as more hydrodynamically violent than film boiling, and is often linked to metal fragmentation. The minimum surface temperature necessary to maintain film boiling, i.e., the minimum film boiling point, may be seen as a threshold beyond which fragmentation (and explosions) become less frequent.

Dhir and Purohit's study of film boiling on metal spheres included measurements of the minimum film boiling point [43]. Their tests involved plunging preheated spheres into water baths and measuring the surface temperature at which the vapor film collapses, and transition boiling commences. Results were correlated in terms of water temperature and sphere surface temperature. If a plot of this correlation were overlaid on Figure 4.8,

it would be similar to the dashed line that has been plotted, but would be displaced upward to higher reactant temperatures. Film boiling occurs above the line, when water and metal temperatures are relatively high, while transition boiling takes place below it.

In general, our experimental data shows that explosive interactions become more probable as reactant temperatures increase. However, our original assertion here was that transition boiling is more likely to cause fragmentation and explosive reactions than film boiling. In fact, we see a *decrease* in explosive reactions at temperatures where transition boiling is expected, which is at lower reactant temperatures. This simple evaluation suggests that fragmentation caused by transition boiling is not the mechanism responsible for triggering the explosive reactions observed in these experiments.

V REACTION RATE MEASUREMENTS

The main goal for this study has been to determine the reaction rate of molten lithium in water for various initial reactant temperatures. Experiments discussed in chapter three dealt with the discovery and subsequent mapping of an ignition boundary for the lithium/water reaction in terms of initial reactant temperatures. Unfortunately, the experimental configuration necessary for this work was ill-suited to measure quantities useful for determining reaction rates. Thus the apparatus was modified and instrumentation was added. This chapter covers the experiments for measuring the reaction rate of molten drops of lithium metal injected into water. It is emphasized that our interest here is in the reaction rate for mild reactions rather than explosive ones.

The chapter begins with a description of modifications made in the experimental apparatus and procedure so that reaction rates could be determined. Then the new instrumentation introduced for these tests is detailed. A 3-color pyrometer used for temperature measurement of the drop is of particular note, and will be discussed extensively. After this, the methodology for using test measurements to calculate reaction rates is described. This is followed by a presentation and discussion of experimental findings. These findings are compared to calculations with the model described in the previous chapter, and with the results of investigations discussed in chapter two. The remainder of the chapter is devoted to identification and estimation of measurement errors.

V.I Experimental Apparatus

Discussion of the new apparatus and procedure is motivated by giving a synopsis of how the reaction rate is measured. First, it should be mentioned that the design was strongly influenced by results of the scoping tests. Subsequent tests will avoid initial conditions that proved conducive to explosive reactions, but such events must be considered in the new design. The literature review showed that experiments for quantitative reaction rate measurements typically depend upon a closed volume type design to contain reaction products. The pressure change resulting from gas and vapor generation is used as an indication of how far the reaction has proceeded. This strategy was regarded as unwise considering the explosive potential of the reaction; recall that peak pressures near 4 MPa were recorded inside an open reaction vessel during two of the scoping tests.

An alternate approach is to retain the open volume design used in the scoping tests while relying upon photography of the reaction and temperature measurements of the drop for reaction rate calculations. In essence, the injector produces a drop of lithium that rises through the water while generating hydrogen, and at a known point in time the bubble is photographed. The picture is used to calculate bubble volume, which corresponds to the amount of hydrogen gas present. The hydrogen generation is used to calculate an average reaction rate for the drop during the interval between injection and the measurement. An additional means of calculating the reaction rate involves measuring the drop surface temperature and writing an energy balance for the droplet. These two approaches are described in detail in section 5.4.

The major change in the experimental apparatus described in chapter three occurred with the reaction vessel. Photography plays a key role in reaction rate measurements and so the aluminum reaction vessel used to contain explosive reactions is inadequate for the new test series. A new reaction vessel, with transparent acrylic windows to facilitate photography, was designed and constructed. Front and side views of this are shown in Figure 5.1. The vessel is a 202 mm square steel tube that is 750 mm high and has 16 mm thick walls. Transparent acrylic plates (38 mm thick) serving as window panes are clamped against the outside surface of the reaction vessel with steel bars. The necessity for such thick materials was indicated by a stress analysis that used previous explosions as a source term. A safety requirement for the new design is that it should be capable of withstanding any of the previous pressure transients. A square-shaped vessel is required for good photography, but the structural strength suffered as a result. Stronger and thicker materials were used to compensate for this lack of strength.

Square windows were cut in the steel tube at three different vertical levels, both in front and back. However, the reaction is photographed through only one pair of windows during a particular test. The three sets of windows allow one to choose a total reaction time for the drop by varying the amount of water it must travel through before being photographed. It was found from early tests with the acrylic reaction vessel that pictures of the reaction were best when the bubble is silhouetted against a bright background. This is accomplished by shining tungsten lamps on a white background placed behind the reaction vessel. The video camera views horizontally through the two

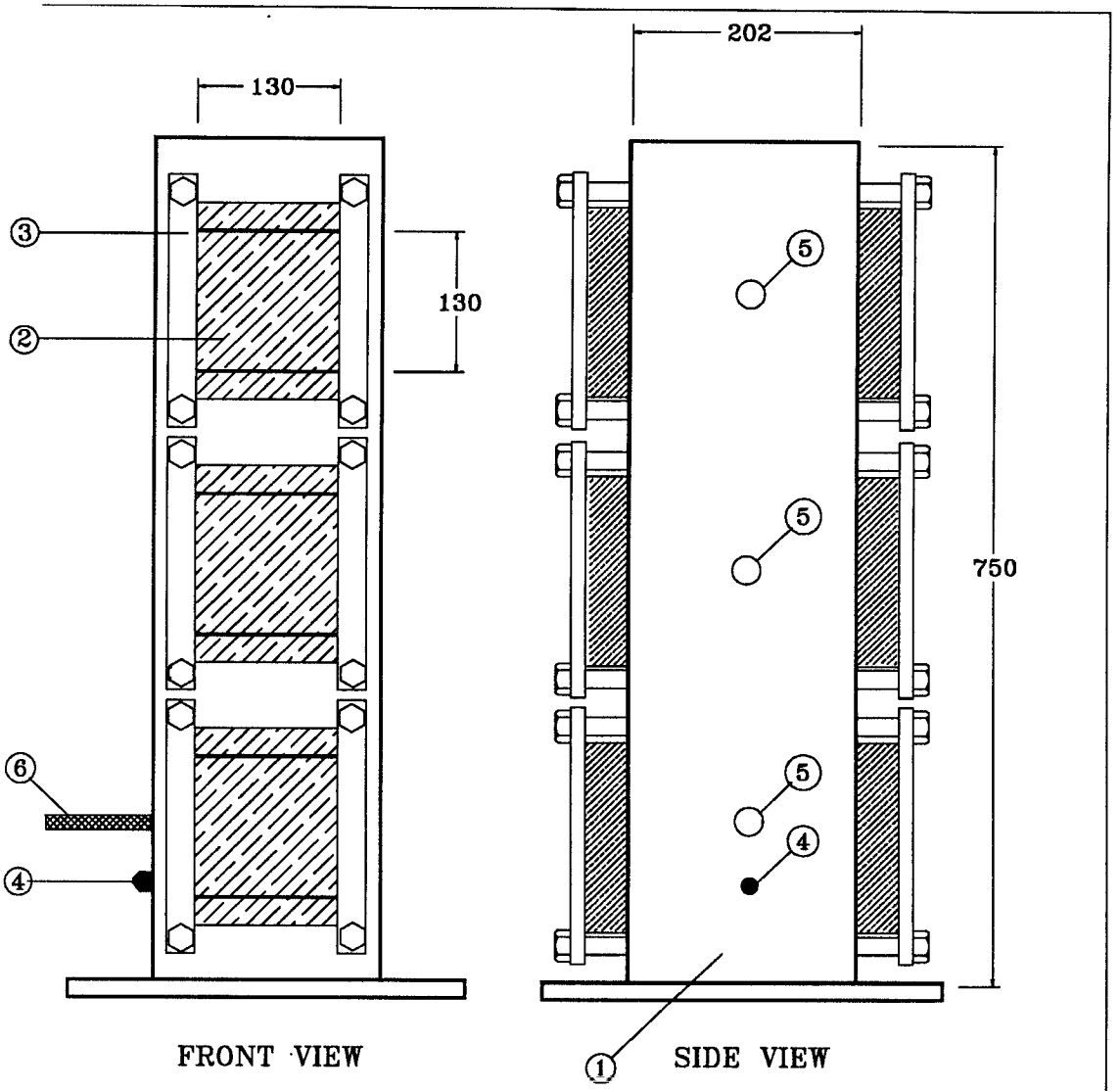

number	description
6	fibre optic cable support
5	pyrometer port
4	pressure transducer
3	steel clamp
2	acrylic plate
1	steel tube

Figure 5.1

Reaction Vessel for Visual Observations

windows at one level.

Another addition to the experiment for this new test series is a 3-color pyrometer. This instrument is used to measure the temperature of the droplet as it rises through the water. This measurement is a crucial element in the new test series and so we will now digress to explain the operation principles and implementation of this device.

V.II Temperature Measurement Through Radiation Thermometry

Previous experiments with small-scale metal/water reactions do not incorporate measurement of the metal temperature, or it is measured in a crude fashion. It was decided that a significant improvement on previous work would be made if the lithium drop temperature could be measured directly and accurately. A radiation ratio thermometer was deemed to be the only instrument capable of making the measurement under the restrictive conditions of these tests. This measurement would have been impractical with more conventional means, such as thermocouples or a disappearing filament pyrometer. The first complication is the necessity to make the measurement remotely due to the potentially hazardous nature of the lithium/water reaction. Additional difficulties arise from the rapidly changing temperature of the drop, the wide range of this change, and because the drop is not stationary. The time elapsed between injection and the drop reaching the water surface is about three seconds, so it is necessary to complete the temperature measurement during an interval less than this. It was decided that a 3-color pyrometer, or ratio thermometer, was the most appropriate device to use under the given circumstances. Radiation thermometry is a powerful

temperature measurement technique, yet some simplifications and assumptions regarding the body to be measured must be made to put the technique into practice. These are indicated by way of briefly reviewing the basic physics involved in radiation thermometry and the principles behind the ratio thermometer.

The spectral distribution of power emitted from the surface of a black body is given by Planck's Law [47]:

$$i_b(\lambda,T_b) = \frac{C_1}{\lambda^5\left(e^{C_2/\lambda T_b} - 1\right)} \quad W/m^2\,\mu m\,sr \tag{5.1}$$

where $\mathbf{T_b}$ is the absolute temperature of the black body, λ is the wavelength at which the energy is being emitted, and $\mathbf{C_1}$ and $\mathbf{C_2}$ are the constants $1.19\text{x}10^4$ W $\text{um}^4\text{cm}^{-2}\text{sr}^{-1}$ and $1.44\text{x}10^4$ um K, respectively. $\mathbf{i_b}$ is called the spectral intensity and it is the amount of power emitted per unit wavelength at the wavelength λ, in a specified direction, per unit solid angle in this direction, and for a projected unit surface area normal to this direction. A black body absorbs all incident radiation, regardless of direction, and emits radiation isotropically so that the spectral intensity, as defined, is independent of direction. The lithium droplet does not qualify as a black body and the difference in spectral intensity is accounted for by the emissivity:

$$i_{drop}(\lambda,T) = \varepsilon(\lambda)\, i_b(\lambda,T_b) \tag{5.2}$$

where the emissivity can, in theory, be used to account for all the variations in $\mathbf{i_{drop}}$ from the ideal black body. The emissivity may be a function of wavelength, temperature, direction, surface roughness or oxide coating on the drop, etc. In practice, it is difficult to account for all these variations so instead, the drop will be treated as an isotropic

emitter with emissivity depending only upon λ.

For the radiation wavelengths and temperatures of interest, the exponential term in Equation 5.1 is much larger than one and so Equation 5.2 can be written as:

$$i_{drop}(\lambda,T) \approx \varepsilon(\lambda)\, C_1 \lambda^{-5}\, e^{-C_2/\lambda T} \tag{5.3}$$

With this expression for power output at a particular wavelength, one can write the ratio of the spectral intensities at two distinct wavelengths:

$$\Re \equiv \frac{i_{drop}(\lambda_1,T)}{i_{drop}(\lambda_2,T)} = \frac{\varepsilon(\lambda_1)}{\varepsilon(\lambda_2)}\left(\frac{\lambda_1}{\lambda_2}\right)^{-5} e^{\frac{-C_2}{T}\left(\frac{1}{\lambda_1}-\frac{1}{\lambda_2}\right)} \tag{5.4}$$

It is now evident that the temperature of a radiating body may be determined with the ratio of the spectral intensities at two distinct wavelengths, and the emissivity of the body at these wavelengths. This is the basic principle behind a ratio thermometer, or two-color pyrometer. If the emissivity is identical at the chosen wavelengths, or varies little, it cancels from Equation 5.4 and need not be known to determine temperature. Moreover, emissivity variations with angle of emission, surface roughness, etc. (which have all been neglected) need not contribute to measurement error. If these emissivity variations are small between λ_1 and λ_2, the measurement error will be small. A more detailed discussion of error will be undertaken in section 5.7.

V.II-I Three-Color Pyrometer

The very specific requirements for the pyrometer: fast response, high sensitivity, detection in the near infrared spectrum, and ruggedness (to withstand inadvertent

explosions), made it difficult to find an acceptable instrument that is made commercially, so one was constructed to meet the desired specifications. Figure 5.2 is a schematic that includes the major pyrometer components and illustrates how the instrument is employed in the experiment. A fiber optic cable is fed through a port in the reaction vessel beside the window to be photographed. A stainless steel tube is also fed through this port and it forms a rigid sleeve around the cable, holding it in place. The end of the tube is capped off with a 3 mm thick transparent acrylic window and the tip of the fiber optic cable is pressed up against it to view into the reaction vessel. Spectral transmissivity of the window is about 90% for each of the three filter wavelengths chosen for the pyrometer [48].

The cable collects light from the droplet and the trifurcated end sends this light to three different narrow band pass filters. The filters have central wavelengths of 900, 1000, and 1060 nm (the near infrared spectrum) with a full-width at half maximum transmission of 20 nm. The small fraction of light within these narrow bands will pass through the filter and reach a photodiode detector. Note the absence of lenses for focusing additional radiation from the drop to the entrance of the fiber optic cable, or to concentrate light on the active detector area. It was found that the lithium drop radiated sufficient energy that elaborate optics were unnecessary to achieve acceptable signal levels. The combined transmission characteristics of the fiber optic cable, acrylic, and narrow band pass filters will be found when the pyrometer is calibrated.

The photodiodes produce a small current that is proportional to the radiant power falling on the detector area. This current is converted to a voltage, which is amplified,

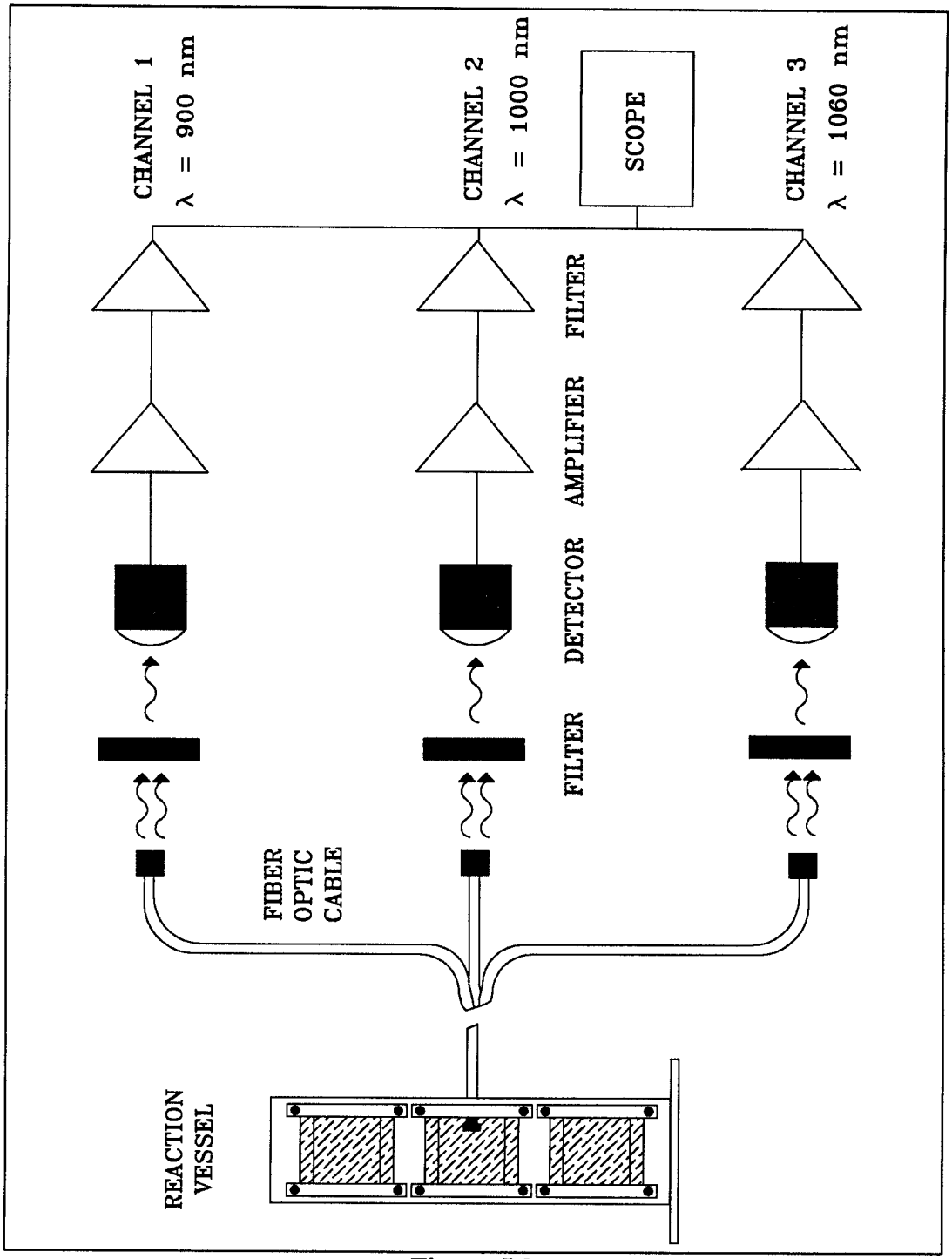

Figure 5.2

Schematic of Primary Pyrometer Components

filtered, and stored in the digital oscilloscope. The amplification and filtering circuitry of a single channel are diagramed in Figure 5.3. The current from the photodiode is converted to a voltage signal by an operational amplifier in the first stage of the circuit. The amplification level is controlled by selecting one of three feedback resistors. The signal from this first stage is sent to a monolithic amplifier purchased from Brown-Burr Electronics Inc.. This device amplifies the signal by 1000 and eliminates considerable high frequency noise because of the amplifier's high common-mode rejection ratio. The signal quality at this point is usually high enough that it can be used without further conditioning. Finally, the second stage output is filtered by a 4-pole Chebyshev low pass filter with a cut-off frequency of about 200 Hz. This filter adds further reduction of high frequency noise. A table containing selected hardware specifications is included in Appendix C for reference.

As a final note, it is pointed out that a 3-color pyrometer was constructed though the theory discussed in the previous section indicated that two colors are sufficient to calculate temperatures. The reason is that by introducing one additional channel (at a modest cost) we now have three signal ratios from which temperatures may be calculated, rather than one. Agreement in the calculated temperatures from each of the three signal ratios will add confidence in the measurement. Another reason the additional channel was regarded as advantageous is that this pyrometer is a prototype. Preliminary design calculations were based upon several assumptions about the lithium drop and water, and a number of compromises were necessary. It was not possible to be sure which wavelength combinations would provide the most accurate temperature

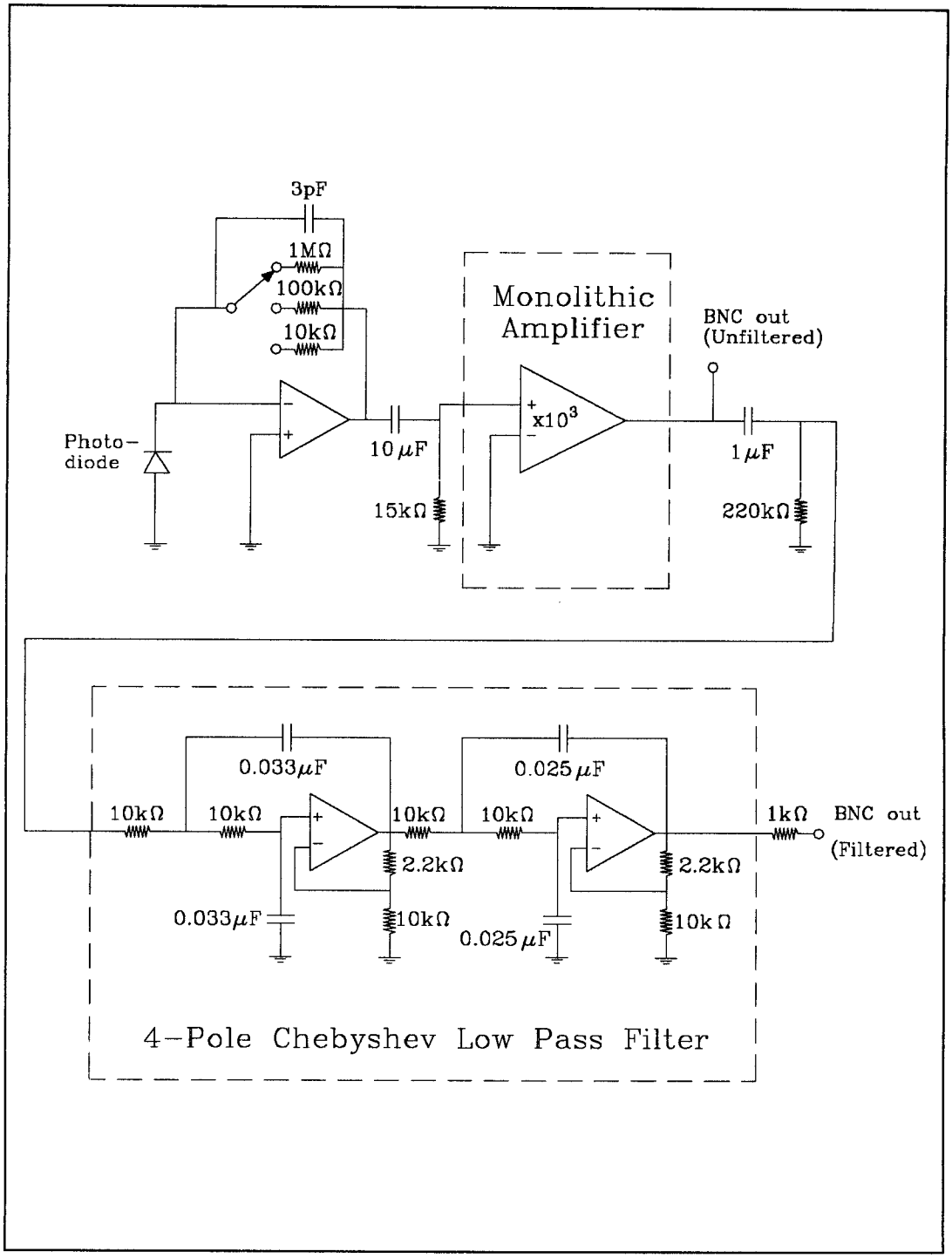

Figure 5.3

Pyrometer Circuit Diagram

measurements until the device was built and tested. It is also desirable to have an extra channel so that if one malfunctions during a test, a temperature measurement may be obtained with the remaining two.

V.II-II Pyrometer Calibration: Theory

The response of each pyrometer channel as a function of temperature is unknown, thus the instrument is not useful until it has been calibrated with a high temperature source. The voltage output of a particular channel can be expressed in the following general form:

$$V = \int_{\Delta\lambda}\int_{\omega}\int_{A_{source}} i_b(\lambda,T_b)\,\varepsilon(\lambda)\,e^{-\alpha(\lambda)r}\,\tau(\lambda)\,F(\omega,A)\,R(\lambda)\,G(f)\;dA\,d\omega\,d\lambda \quad (5.5)$$

Where the new variables are defined as follows:

- $\tau(\lambda)$ is the combined transmittance of the acrylic window, fiber optic cable, and narrow band pass filter, all are a function of radiation wavelength, λ.

- $\mathbf{F(A,\omega)}$ is the fraction of radiation that, after passing through the narrow band pass filter, falls on the active detector area. Radiation leaving the fiber optic cable forms a cone-shaped region as it passes through the filter; there is no condensing lens between filter and detector, and so this cone may be large enough that some radiation will miss the active detector area. The size of the cone shrinks as the light entering the fiber optic cable becomes more parallel to the cable axis. As a result, $\mathbf{F(A,\omega)}$ varies with the size of the source and its distance from the receiving optics.

- $\mathbf{R(\lambda)}$ is the photodiode response, in amps/radiant watt, and is also a strong

function of wavelength.

• **G(f)** is the combined gain of the amplification and filtering circuitry in volts/amp. This gain is a function of signal frequency, **f**.

• $e^{-a(\lambda)\,r}$ is a term that accounts for the absorption of radiation in the medium between the radiating source and collection by the fiber optic cable. **a** is the absorption coefficient of the medium and **r** is the path length a light ray must travel from a point on the source to the cable. Ideally, one would select a wavelength where the absorption coefficient is small (or keep the path length small) so that this absorption term is nearly equal to one, and may be neglected. Unfortunately, we must make the temperature measurement through a few centimeters of water and use wavelengths in the near infrared, so it is found that this term cannot be neglected.

• $\varepsilon(\lambda)$ is the emissivity of the drop surface. In this analysis, only the emissivity of pure lithium metal is considered, and the effects of reaction products on the surface are neglected. Shvarev and Baum used classical electronic theory to derive an expression for the emissivities of good conductors [49]. Their analysis predicts that the emissivity of lithium will not depend on radiation wavelength. For the remainder of this chapter, the emissivity of the drop will be assumed constant.

The integrals are to be taken over the wavelength interval of interest $\Delta\lambda$, the solid angle subtended by the radiating source ω, and the projected area of the radiating body A_{source}. The wavelength-dependent terms in Equation 5.5 may be assumed constant for the small wavelength interval of the narrow band pass filter. It is also assumed that the radiation intensity is constant over the radiating surface (it need only be constant

across the fraction of surface area from which the optics are collecting the bulk of the radiation), so the intensity is constant across the small solid angle subtended by the radiating source. Using these assumptions, Equation 5.5 can be integrated to produce the following:

$$V \cong i_b(T_b)\,\varepsilon\, e^{-ax}\,\tau F R G(f)\;\omega\,\Delta\lambda A_{source} \tag{5.6}$$

where the integral of e^{-ar} over the solid angle has been replaced by e^{-ax}, with x being the distance between the cable aperture and the radiating body. This is an appropriate approximation when the body is small compared to the path length. The wavelength dependent terms are all evaluated at the wavelength about which $\Delta\lambda$ is centered.

The main attraction of the two-color technique is that it permits temperature measurements without actually determining each parameter in Equation 5.6 explicitly. First, the above expression is rewritten by substituting for the spectral intensity and writing:

$$V = \Psi\, C_1 \lambda^{-5} e^{-C_2/\lambda T}\,\varepsilon\, e^{-ax} F \omega A_{source} \tag{5.7}$$

where:

$$\Psi = \tau R G(f) \Delta\lambda \tag{5.8}$$

The function Ψ depends only upon the components of a particular pyrometer channel and the signal frequency. Calibration of the pyrometer requires that the voltage output of each channel be found as a function of temperature. A furnace used as a high temperature source for calibration will be separated from the fiber optic cable by roughly one meter of air, and so $e^{-ax} \approx 1$. Each channel 'sees' the source from the same vantage point with the trifurcated cable, which makes **F**, **A**, and ω identical for each

channel. Furthermore, the emissivity of the source varies little across the small wavelength interval being used, 900 nm to 1060 nm. These simplifications allow one to write the voltage ratio of two channels, V_1/V_2, as:

$$\Re = \frac{\Psi_1}{\Psi_2}\left(\frac{\lambda_1}{\lambda_2}\right)^{-5} e^{-\frac{C_2}{T}\left(\frac{1}{\lambda_1} - \frac{1}{\lambda_2}\right)} \qquad (5.9)$$

It is now seen that the ratio is independent of the radiating surface area, solid angle viewed, and emissivity of the furnace. To achieve this independence of area and solid angle, it is important that the background of the furnace (visible to the fiber optic cable) be relatively cold. This indicates that radiation from this region may be neglected in comparison to radiation emitted by the oven, and instrument calibration is possible even though the field of view of the fiber optic cable has not been filled.

The constants Ψ_1 and Ψ_2 cannot be solved for explicitly, but the ratio of Ψ_1/Ψ_2 is found by combining Equation 5.9 and calibration curves of channel output versus temperature. With this information, one can use the voltage outputs of two channels and Equation 5.9 to determine the temperature of a black or grey body.

V.II-III Pyrometer Calibration: Procedure and Results

An *Astro Ultra-High Temperature Furnace* graphite resistance furnace (Astro Industries Inc.) was used as the high temperature source for pyrometer calibration. This device was made available by the combustion engineering research group here at the University of Wisconsin. The heated surface inside is made of graphite, and a conical shaped cavity has been hollowed out of the inside. This cavity is a close approximation

to a black body with a total emissivity of .996 [50]. A helium gas atmosphere is maintained within the furnace to prevent development of an oxide coating on the graphite at high temperatures. A 28 mm diameter port at the front end of the oven provides a clear view to the heated surface inside. The oven temperature is measured with a *Micro-Optical Pyrometer* disappearing filament pyrometer (the Pyrometer Instrument Company Inc.). The manufacturer's specifications designate the device to be accurate within three degrees centigrade. A schematic that includes these devices and illustrates the calibration arrangement is shown in Figure 5.4. Note that a motor with a rotating wheel is positioned in front of the furnace to chop the radiation signal to the pyrometer; there are two reasons for this. First, we would like to verify that temperature measurements will not depend upon input signal frequency. This is done by varying the rotational speed of the chopper and looking for changes in the calibration constants. Measurements of amplification versus frequency for each channel were made after the pyrometer was constructed, and these suggested that amplification should not vary with signal frequency for the frequency range of interest (see Appendix C). Still, this will be verified.

The second reason for the chopper is to confirm the assumption that the field of view of the fiber optic cable does not need to be filled during calibration. As explained earlier, this requires that the radiation signal from the surroundings be small in comparison to the source signal. With a chopper in place, the pyrometer gives a baseline reading from the background while the oven port is screened, and then a sharp spike appears at each output as the aperture in the chopper rotates in line with the port.

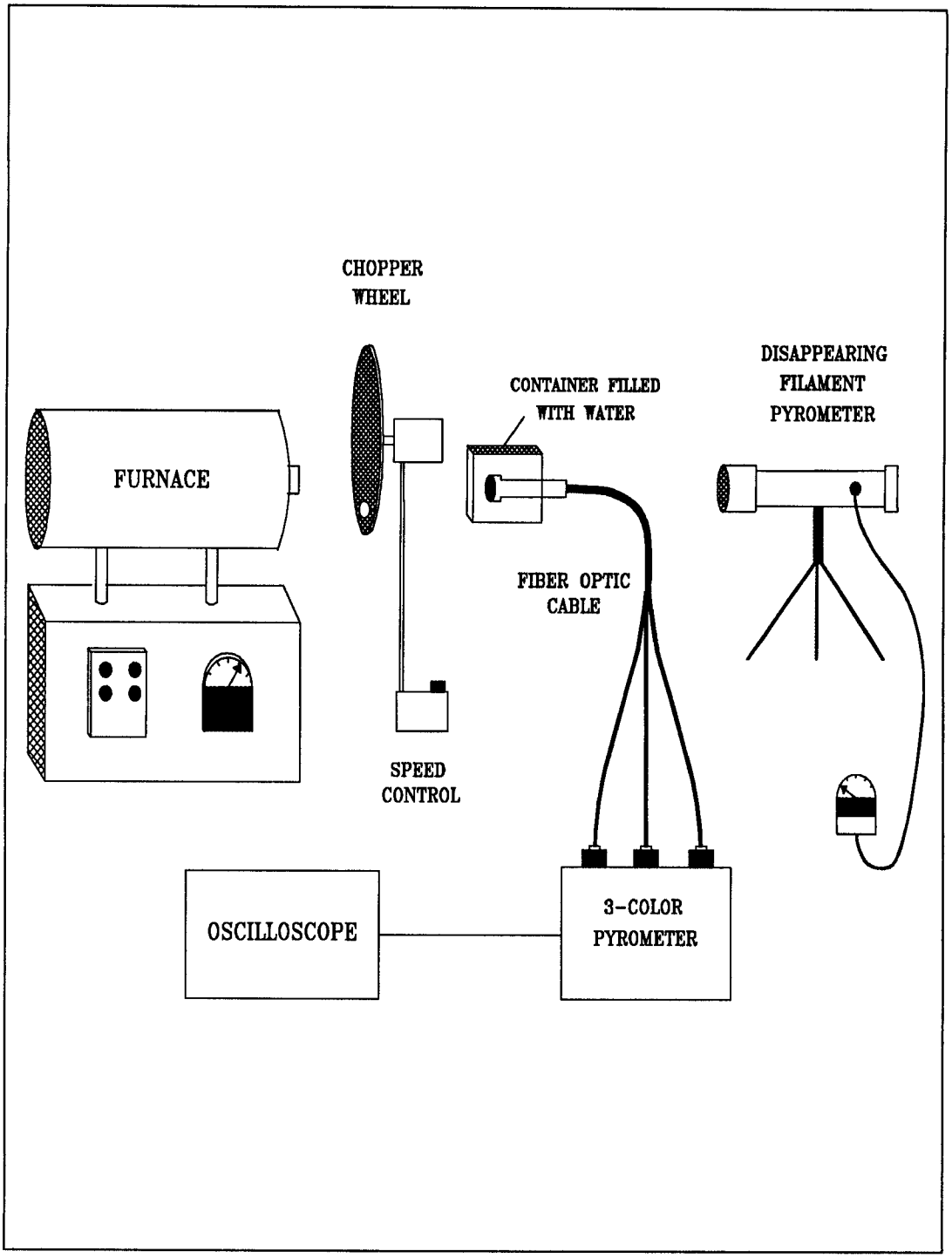

Figure 5.4

Pyrometer Calibration Equipment and Configuration

As long as this spike is much larger than the baseline signal, the original assumption is valid.

The first step in the procedure is to bring the furnace up to temperature, about 2000 C. The furnace temperature is measured by aligning a 10 mm diameter aperture in the chopper with the furnace port and taking a reading with the optical pyrometer. Once this measurement has been recorded, the aperture is covered with black tape and the 3-color pyrometer is positioned in front of the oven. The chopper motor is turned on, and as the wheel rotates, a small pin-hole moves in line between the furnace port and fiber optic cable input. This allows radiation from the oven to reach the pyrometer once every revolution. Output signals from all three channels of the pyrometer are stored in a digital oscilloscope. The peak voltages for each channel are then manually recorded. Due to limited oscilloscope memory and the somewhat slow rotational speed of the chopper wheel, only three to six sets of voltage peaks are recorded for a corresponding temperature reading from the optical pyrometer. The peak voltage for each channel (at the measured oven temperature) is an average of these three to six values.

Once the voltage peaks have been recorded, the chopper frequency is changed and a new set of pyrometer outputs are recorded in the oscilloscope. A new measurement of furnace temperature is then made. This procedure is repeated several times and then the power supplied to the furnace is lowered. When the furnace temperature stabilizes, the above sequence of measurements are repeated.

Calibration results are plotted in terms of the ratio of output signals versus

reciprocal furnace temperature, shown in Figure 5.5. Equation 5.9 shows that the data should form a straight line when this ratio is plotted on a logarithmic axis. A best fit exponential function is obtained by the method of least squares, and this is plotted for each set of data. The y-intercept of each line is equal to $(\Psi_i/\Psi_j)(\lambda_i/\lambda_j)^{-5}$ (where **i** and **j** are the channel numbers), the unknown constants in Equation 5.9. The input signal frequency was varied over the range of about 20 Hz to 40 Hz, and no significant change in signal ratio was found, as expected. Error bars shown in Figure 5.5 are calculated from an error propagation formula [51], and the standard deviation of voltage peak measurements at a particular furnace temperature.

When the pyrometer is used to measure the lithium droplet temperature in water, the absorption term in Equation 5.7 can no longer be neglected. In this case, the voltage ratio of two channels is written as:

$$\mathfrak{R} = \frac{\Psi_1}{\Psi_2}\left(\frac{\lambda_1}{\lambda_2}\right)^{-5} e^{-\frac{C_2}{T}\left(\frac{1}{\lambda_1}-\frac{1}{\lambda_2}\right)} e^{-x(a_1-a_2)} \qquad (5.10)$$

where the absorption terms at each wavelength may be found from published experimental data [52,53]. With absorption coefficients and the path length through water, one can calculate the drop temperature using the calibration data shown in Figure 5.5. However, close inspection of the absorption spectrum of water reveals absorption coefficients that vary greatly with wavelength. For example, between 900 nm and 1000 nm the absorption coefficient increases by a factor of five. Moreover, these coefficients also may be expected to vary with water purity. The net result is that drawing absorption coefficients from tabulated data may be insufficiently accurate.

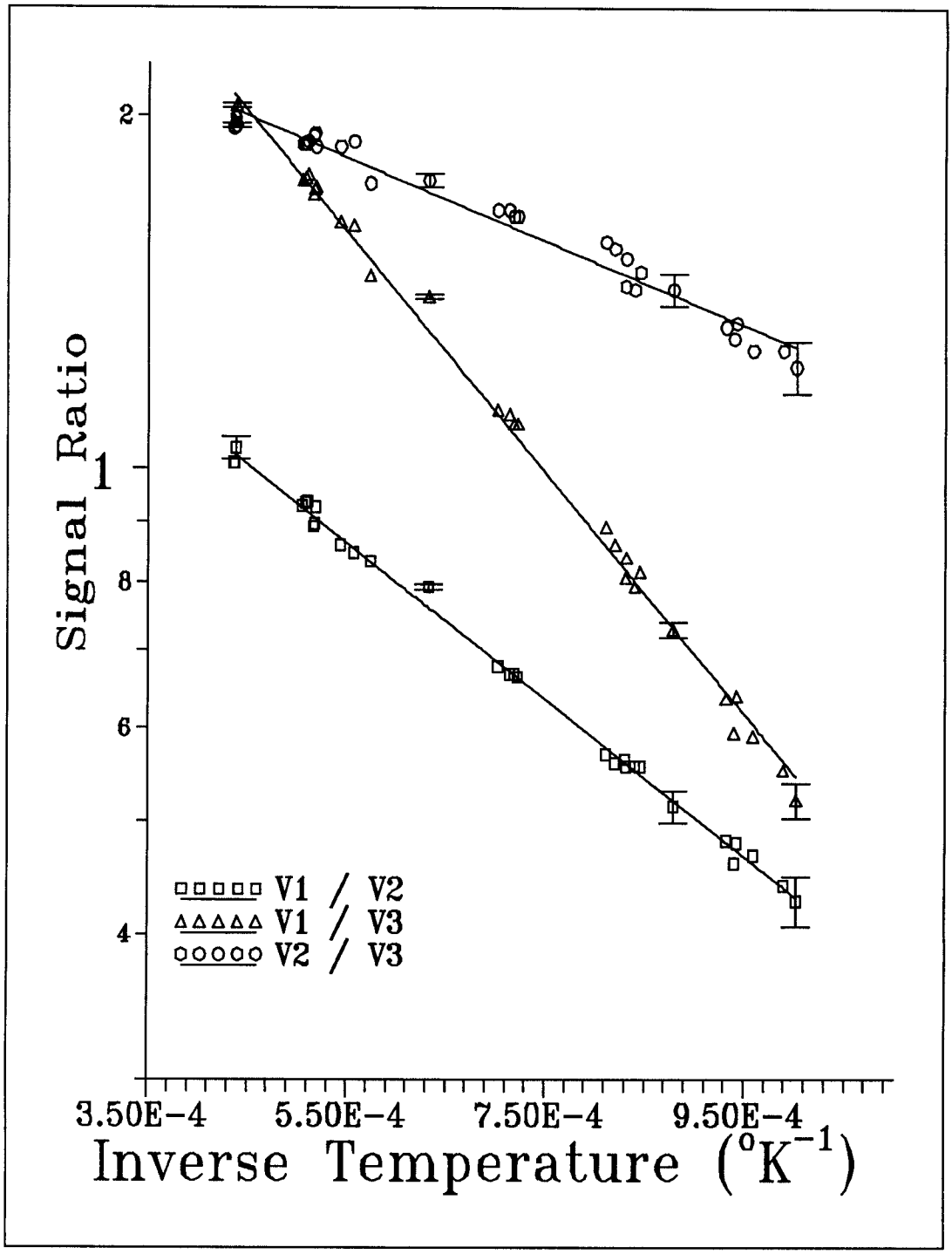

Figure 5.5

Pyrometer Calibration Curves:
Ratio of Output Voltages versus Reciprocal Furnace Temperature

These must be well known if we are to make accurate temperature measurements in water. This is the motivation behind an additional set of measurements with the furnace and pyrometer. Their purpose is to measure the absorption terms $\mathbf{a_i}$-$\mathbf{a_j}$ for each of the three voltage ratios.

The absorption coefficients are measured with the equipment and procedure described for finding the calibration constants Ψ_i/Ψ_j. The only change is that the end of the fiber optic cable is now enclosed in a black aluminum box filled with distilled water. The front end of the box is capped with a three millimeter thick transparent acrylic plate, which holds water within the box and allows the pyrometer to see the furnace. Tests began with turning on the furnace and allowing it to reach an equilibrium temperature, about 1600 C. The furnace remains near this temperature for the entire procedure. This temperature is measured with the optical pyrometer first, and then with the 3-color pyrometer, as previously described. Following this measurement, the path length through the water is increased and the procedure is repeated.

Results of the calibration tests are shown in Figure 5.6. These are plotted in terms of signal ratio versus water path length. Examining Equation 5.10, it is seen that for constant furnace temperature, the data should lie on a straight line when plotted on a logarithmic axis. The slope is equivalent to the difference in absorption coefficients (e.g., $\mathbf{a_1}$ - $\mathbf{a_2}$ for the ratio $\mathbf{V_1/V_2}$), which are the constants of interest.

Much of the departure from linearity in this data is attributed to fluctuations in the furnace temperature. Measured furnace temperatures ranged from a low of 1568 C to a high of 1620 C. Error bars shown in Figure 5.6 are calculated from the error

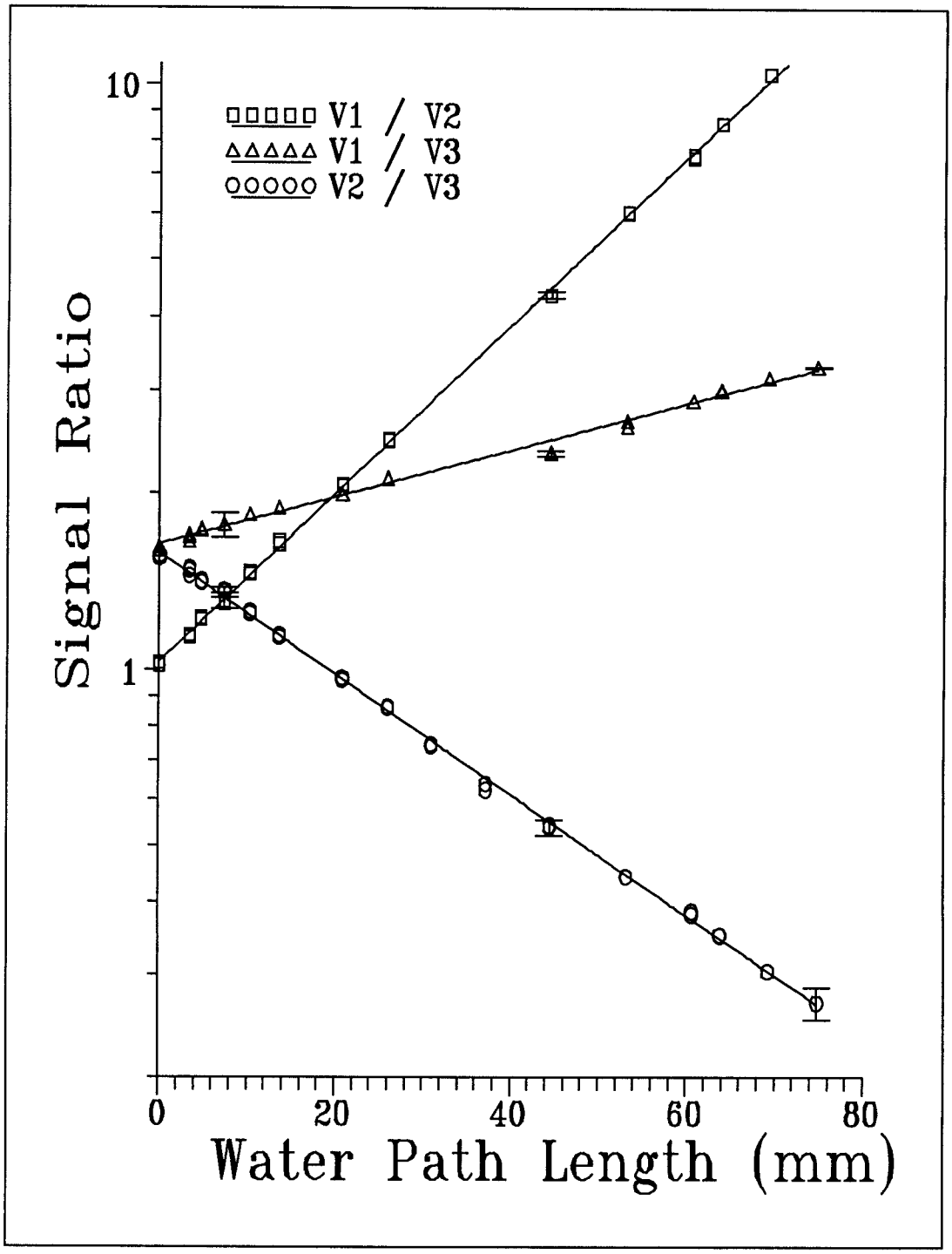

Figure 5.6

Measurements of Furnace Temperature Through Distilled Water: Signal Ratio versus Water Path Length

propagation formula and standard deviation of voltage measurements at each value of path length. All calibration constants are listed in Appendix C for reference.

Before continuing on to discussion of experimental procedure, a final note is made concerning the pyrometer calibration. Close examination of Figure 5.6 reveals inconsistencies in two of the curves. The y-intercepts in Figure 5.6 are signal ratios for zero water path length, while the calibration curves in Figure 5.5 are entirely for zero water path length. Consequently, the y-intercepts of each curve in Figure 5.6 should correspond to signal ratios in Figure 5.5 at the same furnace temperature (about 1600 C). This is not the case for **V1/V2** and **V2/V3.** Examination of the data suggests that **V2** was too small during the calibration with water. A satisfactory explanation for this has not been found. The net result of this problem is that using **V2** for temperature measurements through water will be unreliable. Therefore, only the ratio of **V1/V3** will be used to calculate the lithium drop temperature. This is not regarded as a major difficulty because the ratio **V1/V3** is expected to give the most accurate temperature measurements of the three signal ratios. The water absorption term $\mathbf{a_i}$-$\mathbf{a_j}$ is smallest for this signal ratio, and error in the temperature measurement increases with this term. If the pyrometer is used at some later date for measurements in water, the calibration through water should be repeated to investigate the problem.

V.III Experimental Procedure

The experimental procedure for the current tests is identical with that described for the scoping tests, except for some minor changes and additions, which are detailed

below. Additions include filming the reaction with the video camera, and drop measurement with the 3-color pyrometer.

It is very important that the lithium drop surface area is well known in these reaction rate experiments. The best way to achieve this is to ensure that only one droplet is produced in each test. It was established after numerous tests that the optimum mass of lithium to load into the injector is about 0.75 g. This is the mass of lithium placed inside the injector and melted (as described in the experimental procedure for the scoping tests) before each test. During the heat-up phase of the experiment, the pyrometer is tested with a high-temperature source to verify that it is functioning properly. The test is quite simple, consisting of quickly moving the source past the pyrometer input and confirming that all three channels respond in unison, and that output magnitudes are similar. After this procedure, the fiber optic cable is fed through a port in the reaction vessel adjacent to the window to be photographed.

Several early tests with the new reaction vessel showed that reaction geometry, i.e., bubble shape and position, grows more complex and irreproducible as the drop rises. The observed geometry was usually too complex (to assume a single bubble with well defined shape) by the time the bubble rises to the middle window of the reaction vessel. For this reason, all tests consist of pyrometer measurements and pictures of the reaction through the lowest reaction vessel window. The pyrometer port is midway between the top and bottom edges of the window.

Prior to injection, the video camera is positioned about a meter from the reaction vessel, with a transparent acrylic shield between the camera and reaction vessel. The

zoom lens is adjusted until the bottom window nearly fills the camera's field of view. Recording begins after the twenty second countdown to injection has been initiated and it is stopped about one minute after the injection is completed. Pyrometer outputs stored in the oscilloscope are transferred to the computer and saved in data files on disk.

V.IV-I Reaction Rate Determination I - Hydrogen Generation Measurements

Production of the noncondensible gas, hydrogen, provides a means of determining the amount of lithium reacted. The preferred method for this consists of monitoring the system pressure as a function of time but, for reasons explained earlier, this technique could not be used. Instead, our methods involve measurement of drop temperature and pictures of the gaseous bubble that surrounds the lithium. The pictures are used to calculate the volume of hydrogen present while the measured temperature indicates energy generated by the reaction. These are used to calculate the reaction rate. The hydrogen measurement is discussed in this section. The particulars of the video system, calculations, and assumptions used to find the reaction rate are now detailed.

During a test, the injected droplet of lithium rises through the reaction vessel while surrounded by a bubble of hydrogen and water vapor. The video camera films the event as the bubble rises past the window and pyrometer input. After the test, the video tape is played on a video cassette recorder so that a special software package can be used to capture and digitize individual frames [54]. These frames are saved and written to disk files on the computer. Figure 5.7 shows examples of such digitized pictures, which are from tests 20 and 30. Each picture is made up of 640x400 pixels,

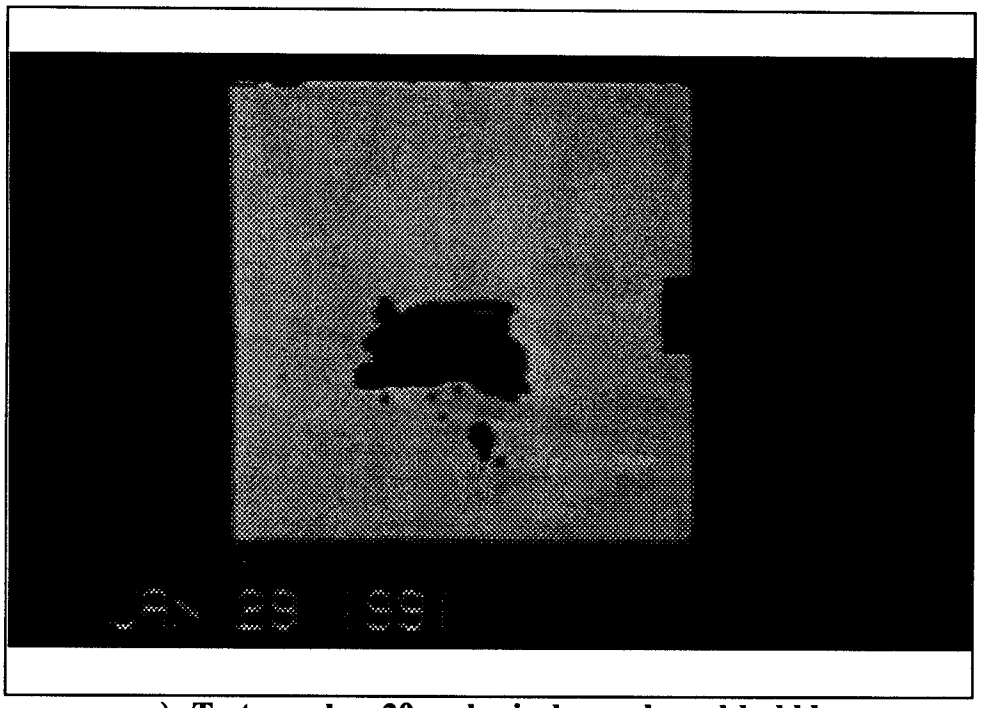

a) Test number 20; spherical cap shaped bubble

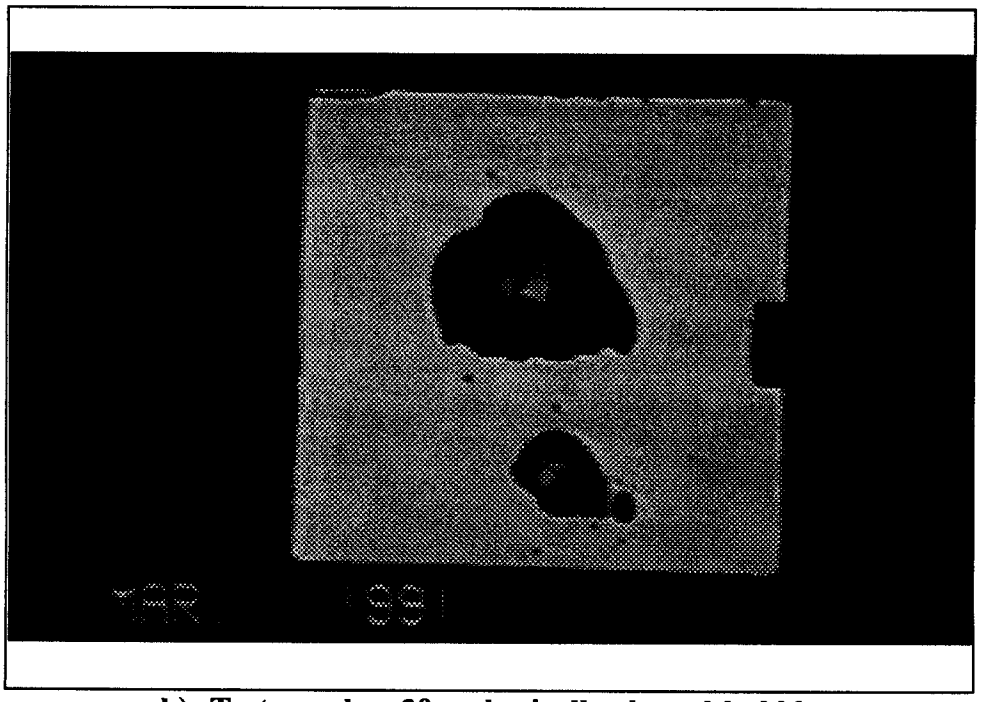

b) Test number 30; spherically shaped bubble

Figure 5.7

Digitized Pictures of Lithium/Water Reactions

where each pixel has one of 16 gray levels. The lightly shaded, square-shaped region is the brightly lit background behind the reaction vessel, and the dark projection on the right side of the window is the stainless steel tubing that surrounds the end of the fiber optic cable. To make these pictures useful in our analyses, they are altered so that each pixel is either black or white. This is done within the program that digitizes the pictures. The 'enhanced' versions of the pictures in Figure 5.7 are shown in Figure 5.8.

The enhanced pictures are edited by a second commercial software package, Publisher's Paintbrush [55]. This is used to remove the black pixels (replace them with white pixels) that correspond to the pyrometer input and small stray bubbles. Paintbrush is also used to blacken all pixels in the background which make up the area surrounding the reaction vessel window. After editing, we are left with a picture made up entirely of black pixels (these correspond to the background and bubble), except the portion of the reaction vessel window visible behind the bubble. From this edited picture, another picture is created where the drop has been erased and replaced with white pixels.

The two edited pictures are saved as files and used as input to yet another computer program, one that counts the number of black and white pixels in each file [56]. By counting these pixels, and using the measured area of the reaction vessel window as an area scale, the projected area of the bubble is calculated. Several tests with the video system were conducted with spheres to verify the accuracy of this method. This is covered in more detail at the end of the chapter, when sources of measurement error are discussed.

Once the projected area of the bubble has been established, it is still a nontrivial

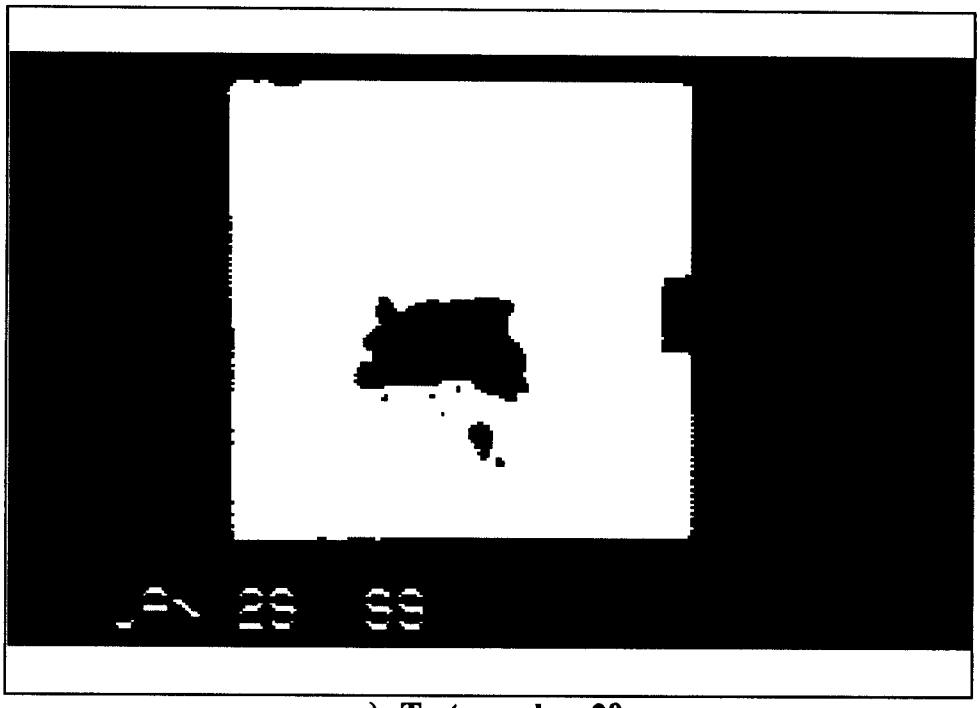

a) Test number 20

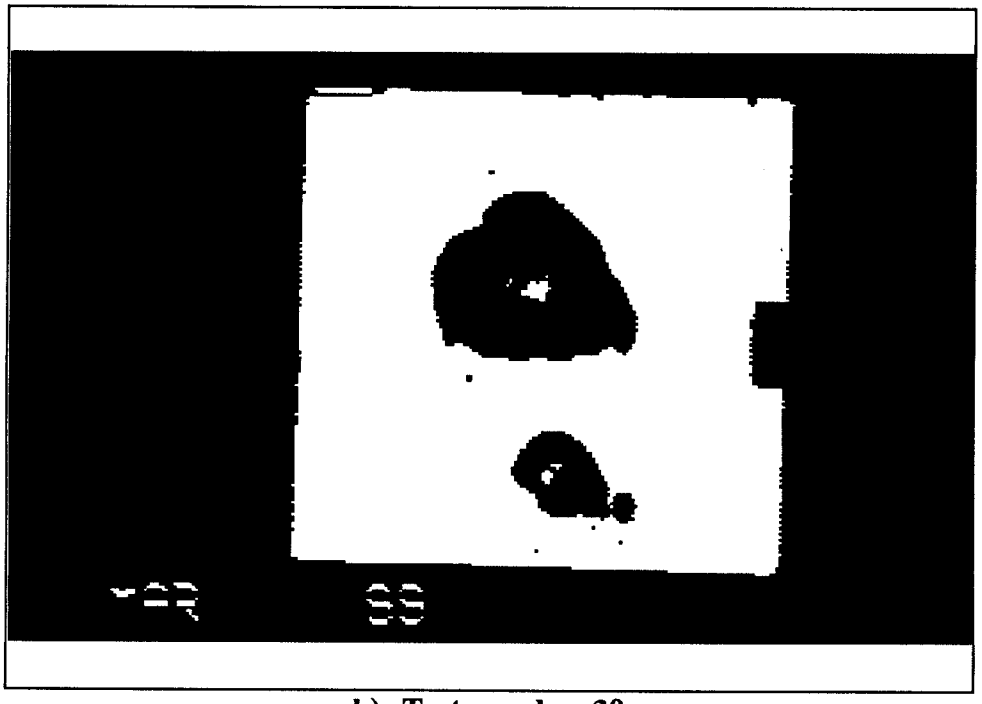

b) Test number 30

Figure 5.8

Pictures of Lithium/Water Reactions: Enhanced Contrast

matter to find the bubble volume. The bubble shape is dependent upon several factors. These include velocity, size, and viscosity (of both bubble and water). Dimensionless groups may be used to characterize gaseous bubbles flowing within a liquid. The relationship between bubble shape and these dimensionless groups is a topic that has received considerable attention [57]. A detailed discussion of this subject is beyond the scope of this study. It is noted though, that two dimensionless groups may be used to characterize bubble flow regimes. These are the Reynolds and Bond numbers:

$$Re = \frac{\rho v D}{\mu} \qquad Bo = \frac{g \Delta \rho d_e^2}{\sigma} \tag{5.11}$$

In these equations, σ refers to the surface tension of water, while the equivalent diameter of the bubble is designated as $\mathbf{d_e}$. These groups represent force ratios, e.g., viscous and inertial forces, surface tension and gravitational forces, and indicate their relative magnitudes. On a plot of Reynolds number versus Bond number, the various bubble shapes may be mapped: spherical, spherical cap, etc. This is shown in Figure 5.9. For conditions observed in our experiments, these dimensionless groups have the following approximate ranges: **Re** ~ 6000-60000; **Bo** ~ 100-500.

From inspection of video-taped reactions, it is found that the bubble can be characterized as either a sphere or a spherical cap. Examples of each shape were chosen for Figure 5.7 to illustrate this. For any given test, the video tape is examined, and a judgement is made whether the bubble shape is closer to a sphere or a spherical cap. Bubble volume is then computed by assuming that the projected area in the picture corresponds to a sphere (for the choice of a spherical bubble) or one-half of a sphere

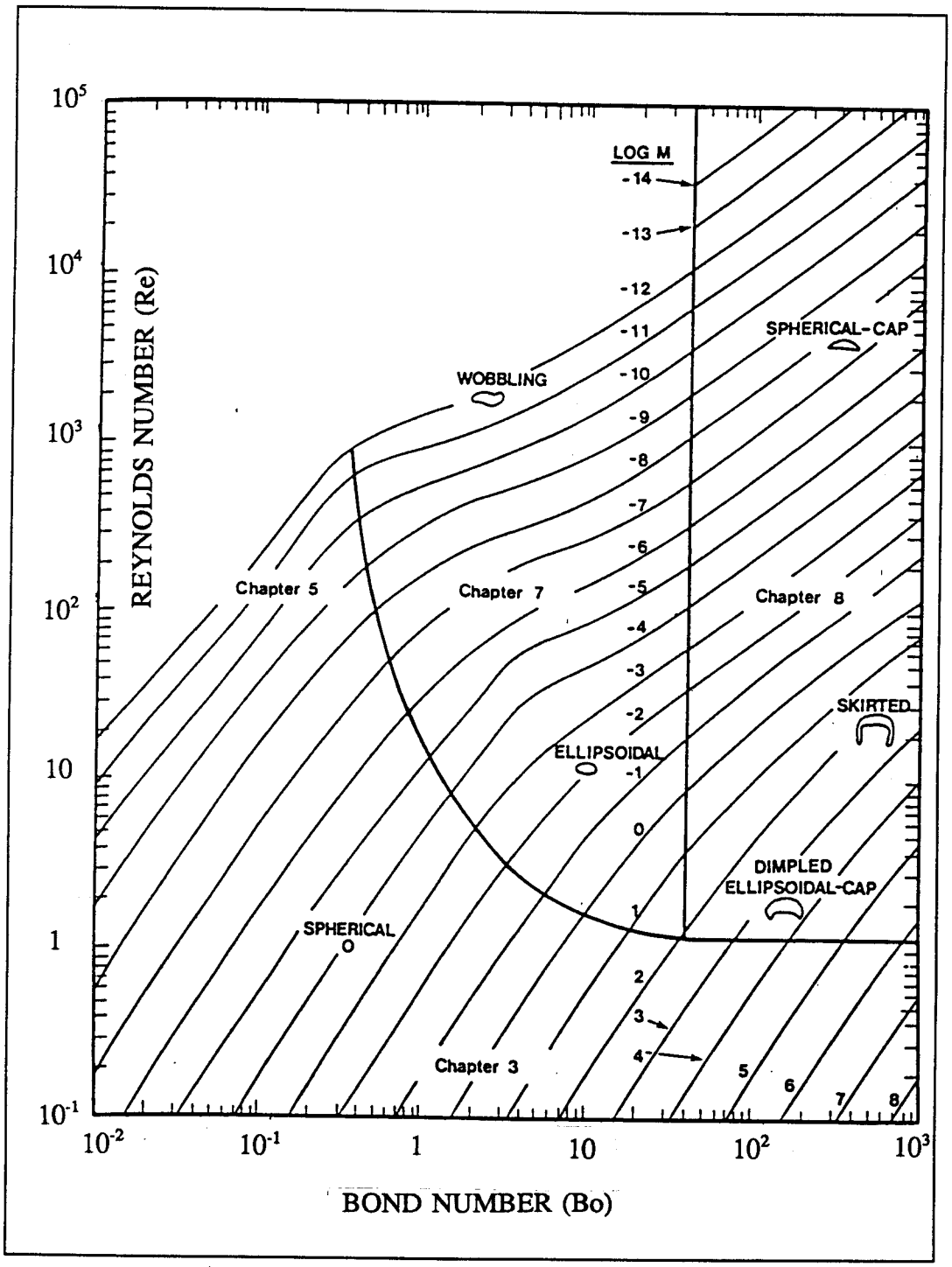

Figure 5.9

Shape Regimes for Bubbles and Drops in Unhindered Gravitational Motion Through Liquids [56]

(for the choice of a spherical cap).

Having found the bubble volume, it is now necessary to find the gas temperature before the mass of hydrogen can be calculated. Also, some relationship between the mass of water vapor and hydrogen in the bubble must be found. Unfortunately, the complex geometry and transient nature of the reaction precludes the possibility of accurately calculating either the bubble temperature or hydrogen concentration distributions. Still, some reasonable assumptions can be made that will provide an upper bound calculation of the hydrogen present, and thus the chemical reaction rate.

The bubble temperature is considered first. It is clear that the gas temperature can be no less than the bulk water temperature, and no higher than the lithium drop surface temperature. For these calculations, the gas temperature is set equal to the bulk water temperature. This assumption is based on the conceptual picture from chapter 4, which envisions a small lithium drop at the bottom of a relatively large gas bubble. There is circulation within the bubble, which cools the gases to a temperature near the bulk water temperature.

Now that a gas temperature has been established, it is a simple matter to decide how to compute the hydrogen concentration. First, it is assumed that the bubble is at atmospheric pressure. This should be a good assumption because a moderate bubble growth rate is observed. For these conditions, the pressure gradient across the bubble and into surrounding water is quite small, much less than one atmosphere. The partial pressure of hydrogen is taken to be the difference between atmospheric pressure and the partial pressure of water vapor at the bulk temperature. The reaction rate **K** is now

written in terms of the bulk water temperature T, and the time interval for reaction $\Delta\theta$:

$$K = \frac{2(P_g - P_v)V_{bub}}{\Re T_{bub}} \frac{1}{A_{drop}\Delta\theta} \tag{5.12}$$

Where the factor of two in the numerator is included because two moles of lithium are required to make a single mole of molecular hydrogen.

V.IV-II Reaction Rate Determination II - Energy Balance

An alternate method for finding the reaction rate involves the use of an energy balance on the lithium droplet. The lithium/water reaction generates a considerable amount of heat, and so the droplet temperature change between injection and measurement by the 3-color pyrometer may be used as an indication of the total amount of lithium reacted. We are unable find an instantaneous reaction rate but, instead, will calculate a rate that is an average over the interval between time of injection and time of temperature measurement.

The energy gained by the drop is the difference between the thermal input from the reaction and energy lost to the surroundings. An energy balance over the interval $\Delta\theta$ takes the following form:

$$\rho c V_{drop}\Delta T = KE\Delta\theta\, A_{drop} - A_{drop}\int_0^{\Delta\theta} [h(\theta)(T_s(\theta) - T_{bulk}) + \sigma\varepsilon(T_s^4(\theta) - T_i^4)]\, d\theta \tag{5.13}$$

Calculations with the numerical model indicate that an approximately uniform temperature distribution may be assumed for the drop when $\Delta\theta \sim 0.5$ s. The lithium droplets formed in these tests are small, about 6 mm in diameter. In addition, the

reaction rate should be less than that calculated with the film boiling model. This indicates that the temperature profile across the drop will be reasonably flat. Consequently, the temperature change of the drop, ΔT, will be set equal to the difference between injection temperature, T_0, and measured surface temperature, T_s.

Convection and radiation losses are written as functions of time because the surface temperature and heat transfer coefficient vary over the interval. Radiation losses are small compared to convection losses because peak drop temperatures are usually no more than about 1000 C, and can be neglected. The integral in Equation 5.13 is approximated by dividing $\Delta\theta$ into five temperature intervals, assuming a linear temperature change with time, and calculating the losses in each interval. Since the temperature change is assumed to be linear with time, the main benefit of dividing $\Delta\theta$ into intervals is the ability to account for changes in the heat transfer coefficient as the film temperature increases. The overall effect is small, and the particular choice of the number of intervals is not important.

Canceling common terms for the area and volume of the drop, Equation 5.13 is rewritten to give an expression for the reaction rate:

$$K = \frac{\frac{1}{3}\rho c R(T_s - T_0) + \frac{1}{5}\sum_{j=1}^{5} h_j(T_{sj} - T_{bulk})\Delta\theta}{E\,\Delta\theta} \qquad (5.14)$$

The heat transfer coefficient is calculated with the expression given in Equation 4.24. The velocity needed to calculate a Reynolds number is simply the distance from the injection point to the elevation where the temperature measurement is made, divided by the elapsed time $\Delta\theta$. Physical properties of the film are evaluated at the film

temperature, and properties of liquid water are evaluated at the bulk water temperature, just as in previous calculations.

The drop surface temperature is found using pyrometer readings from channels one and three. Channel two was not used because of inconsistencies discovered after the calibration process, which were explained at the end of section 5.2-3. The calibration with water would have been repeated, but it was decided that even if this problem were solved, the temperature readings added with this channel are of marginal value. This is because voltage ratios that include channel two (i.e., **V1/V2** and **V2/V3**) fluctuate more than **V1/V3**. The absorption term $\mathbf{a_i}$-$\mathbf{a_j}$ is much greater with channel two, and so changes in water path length result in greater fluctuations of voltage ratio. These ratios are more sensitive to water path length than **V1/V3** (note the relative slopes of water calibration curves in Fig. 5.6). Consequently, if channel two behaved properly, it is likely that we would still choose to use only channels one and three in reaction rate calculations. This is because these two channels will give the most accurate temperature measurements.

Samples of pyrometer traces from tests 20 and 30 are shown in Figure 5.10. These are typical examples of pyrometer outputs. Included in each graph is the signal ratio **V1/V3**. Figure 5.10b shows that even if the individual channel outputs are fluctuating, the ratio is fairly constant. For each test, the voltage ratio used to find drop temperatures is calculated by using the peak value for each channel.

It is believed that little would be gained (in the way of accuracy) by averaging the signal ratios over some interval. As the water path length increases and absorbs the

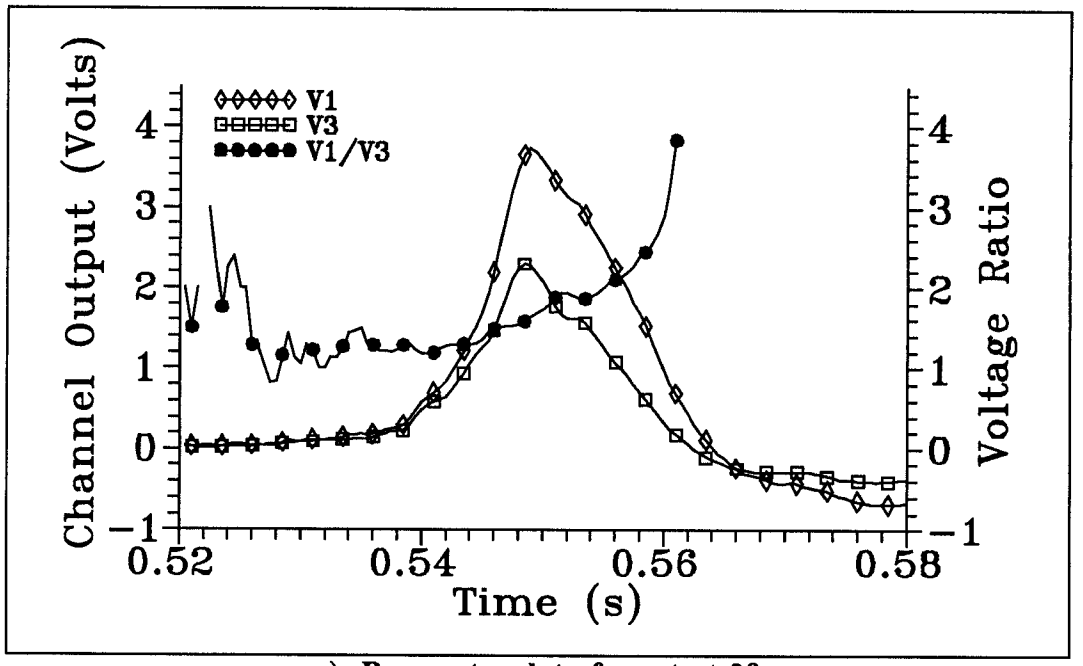

a) Pyrometer data from test 20

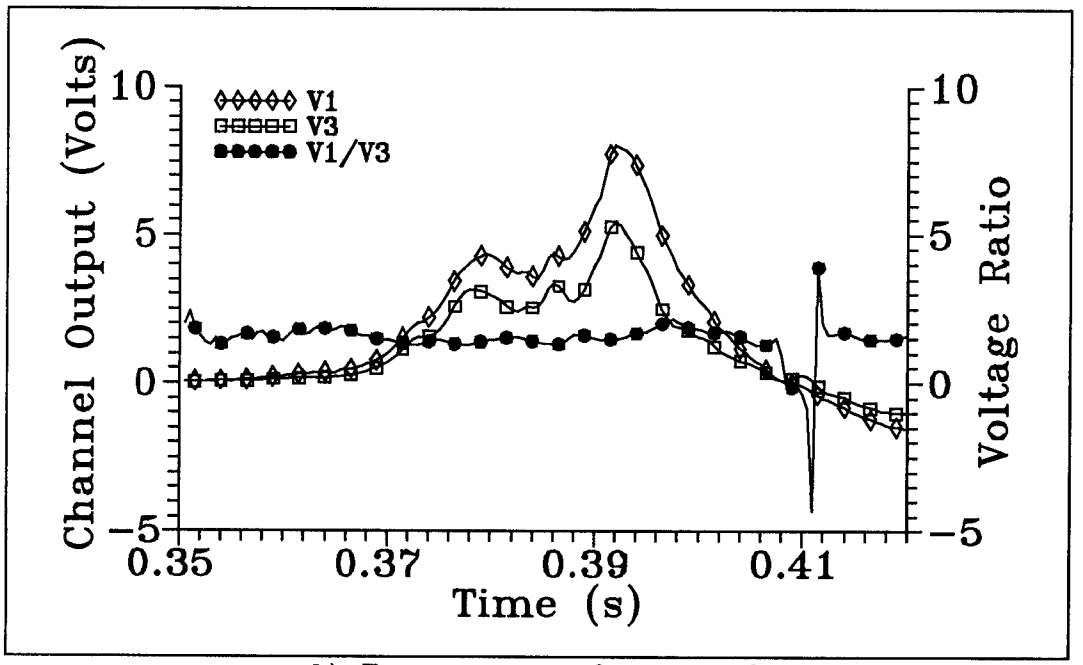

b) Pyrometer data from test 30

Figure 5.10

Pyrometer Signals and Signal Ratio versus Time for Selected Tests

radiation signal, the voltage ratio changes, as illustrated in Figure 5.10a. It is typical for this ratio to rise rapidly at the back end of the voltage peaks because radiation absorption is lower at 900 nm (channel 1) than for 1060 nm (channel 2). Figure 5.10a is an extreme example of this effect. Figure 5.10b is a more typical example, where the voltage ratio is fairly constant while the signal is strong. The change in voltage ratio over time cannot be taken into account because a single value of water path length is used in the temperature calculation. This is described below.

Calculation of temperature from pyrometer readings requires that the water path length between the drop and fiber optic cable input be known. This distance is determined by measuring pictures of the reaction. It is reasonable to assume that the peak in pyrometer voltage output occurs when the water path length between the lithium and pyrometer input is at a minimum. This should occur when the distance between the bubble and pyrometer input is also at a minimum. Basically, this is when the bubble is horizontally level with the pyrometer input.

Several pictures of the reaction are printed for each test to determine the water path length. These are similar to the ones shown in Figure 5.8. For each picture, a caliper is used to measure the minimum distance from pyrometer input to the closest edge of the bubble. The distance across the window is also measured and used as a length scale since this is a known quantity.

V.V Results and Discussion

For this test series, the bulk water temperature was varied between 20 C and 60 C, while the initial lithium temperature was varied between 200 C and 500 C. Reactant temperature combinations used in these experiments correspond to the nonexplosive region mapped during scoping tests (see Fig. 3.3).

Pyrometer measurements indicate that for each test, the drop surface temperature rises to around 1000 C. Typically, this measurement is made 0.5 s after injection. There is no correlation between reactant temperatures and measured drop temperature. This is because the reaction time for each test could not be controlled, and drop temperature increases with reaction time. However, plotting the average time rate of change in drop temperature **(dT/dθ)** as a function of initial lithium or bulk water temperature is meaningful. This is shown in Figures 5.11 and 5.12. Referring to Figure 5.12, the rate of temperature change does not have any clear dependence on water temperature. Computations with the film boiling model suggested that reaction rates should increase with water temperature (see Fig. 4.6a). This was evidenced by the increasing slope of the temperature-time traces as water temperature was increased. The increase in slope is small though, and it is doubtful that changes of this magnitude would be apparent in Figure 5.12 since uncertainties in temperature measurement are fairly large.

Figure 5.11 shows a significant increase in **dT/dθ** as the injection temperature decreases. The data suggests that, generally speaking, the drops are heating rapidly in early stages of the reaction, and then temperatures stabilize around 1000 C. This

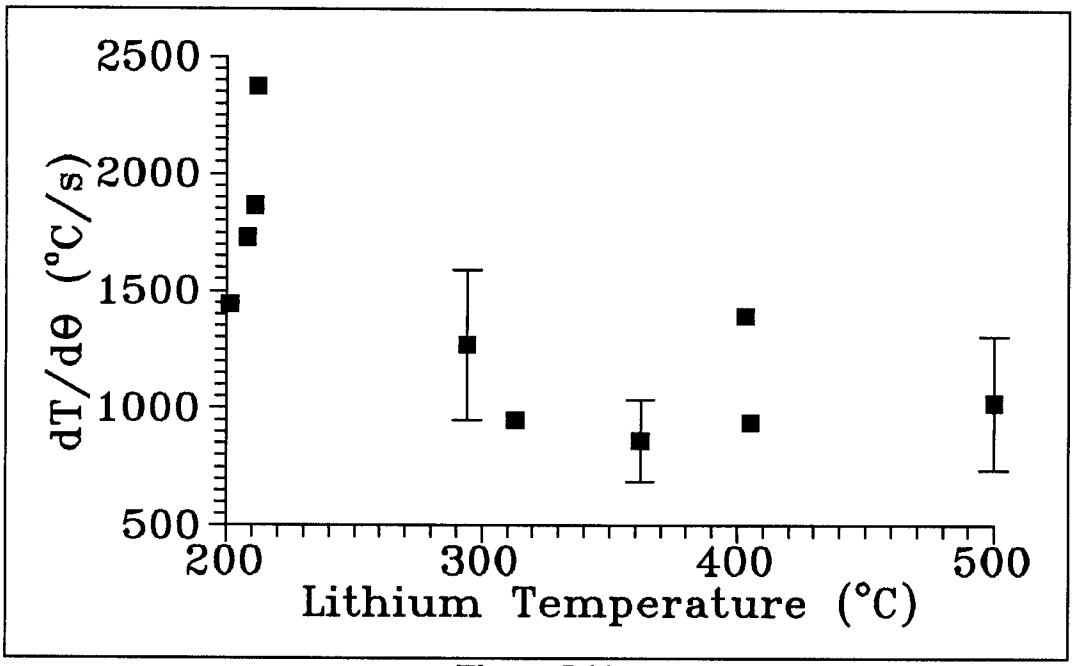

Figure 5.11

Average Rate of Drop Temperature Change versus Initial Metal Temperature

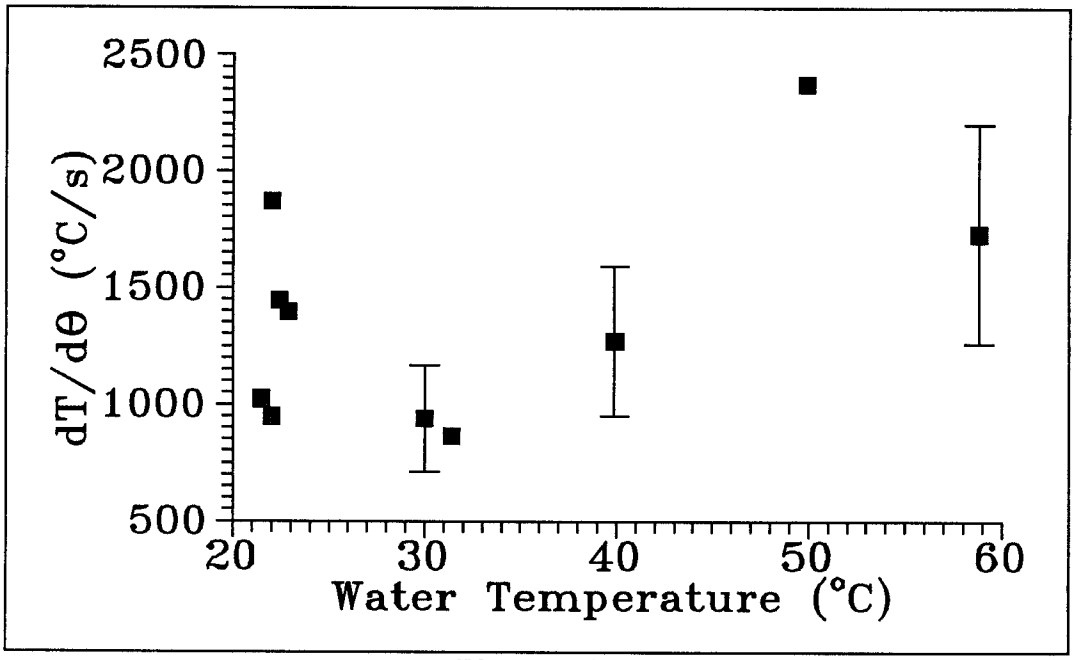

Figure 5.12

Average Rate of Drop Temperature Change versus Bulk Water Temperature

implies that an equilibrium has been reached between energy generated by the reaction, and energy lost from the drop. If this is the case, then a plot of average rate of temperature change over the interval will be higher for drops injected at lower temperatures. This could account for the trend observed in Figure 5.11.

Typical values of uncertainty in $\mathbf{dT/d\theta}$ are included in each figure. These have been computed using uncertainty in the temperature measurements (~15% of the measured temperature), and assuming the reaction time is relatively well known.

Test results are now plotted in various fashions to examine the influence of specific parameters. Figure 5.13 is a plot of reaction rate versus initial metal temperature, with water temperature near 20 C. This first plot is intended to show the influence of injection temperature on reaction rate. A triangle represents a reaction rate measurement from determination of integral hydrogen production. Reaction rate values derived with the energy balance are represented by solid circles. Our first observation is that good agreement exists between the two methods of determining reaction rate. This adds credence to the assumptions made to find these rates. It is also noted that the data in Figure 5.13 does not display any strong trends. This is consistent with conclusions in the previous chapter, which indicated that reaction rates should not be a function of initial metal temperature.

Figure 5.14 shows the reaction rate of lithium, injected at temperatures near 200 C, as a function of water temperature. There is no clear trend in reaction rate versus water temperature. It was expected that the rate would increase with water temperature, but this is not observed. It can be shown that when the film boiling model

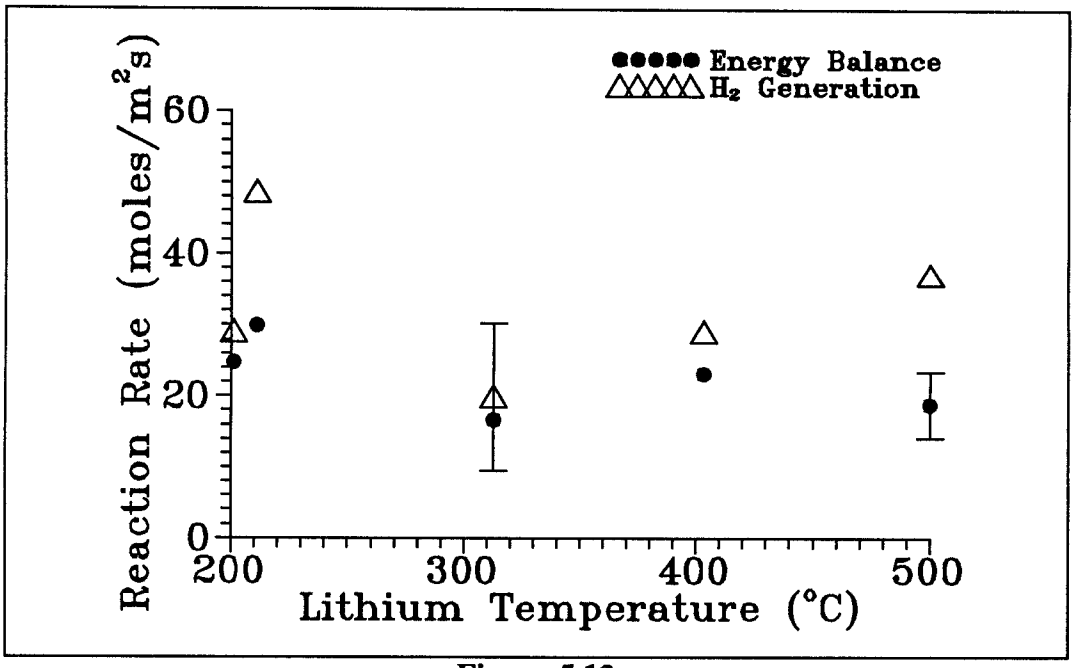

Figure 5.13

Reaction Rate of Lithium in 20 C Water vs Initial Lithium Temperature

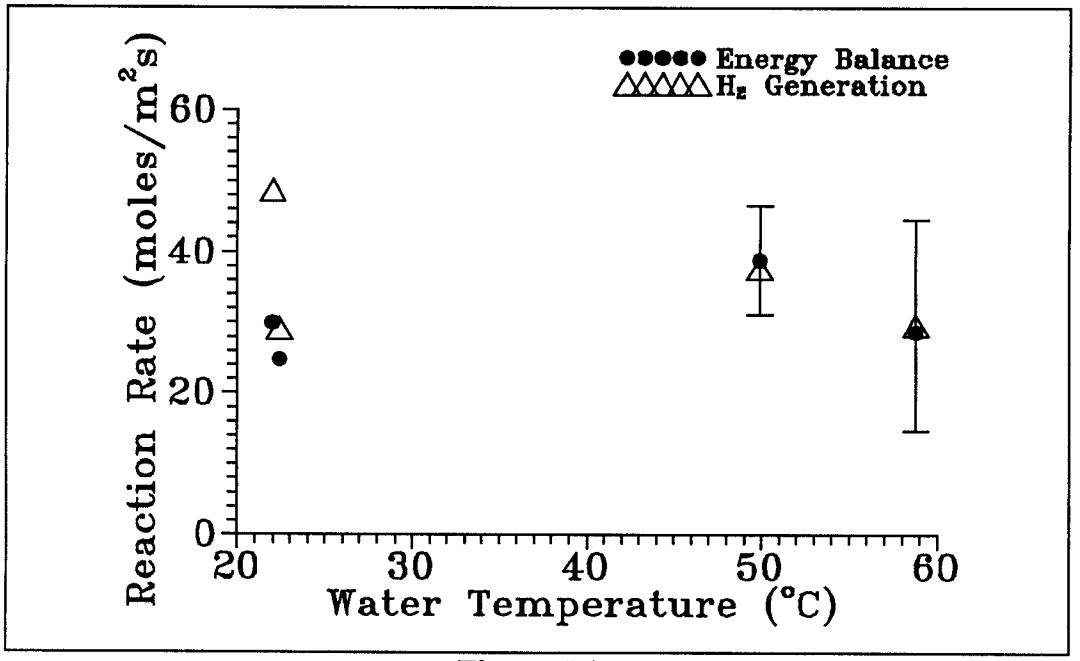

Figure 5.14

Reaction Rate of 200 C Lithium vs Bulk Water Temperature

is used to calculate reaction rates, increasing the water temperature from 20 C to 60 C will increase the reaction rate by about thirty percent. This is a small change when compared to uncertainty in each reaction rate measurement. It is believed that this uncertainty is too large to observe such modest changes in reaction rate.

Error bars have been included in these figures to provide an indication of typical uncertainties associated with these rate measurements. In both Figures 5.13 and 5.14, the smaller error bar corresponds to a reaction rate from an energy balance. Sources of uncertainty with this method are about evenly divided between uncertainty in the temperature measurement, and uncertainty in the lithium drop size. For measurements of hydrogen production, the uncertainties are considerably larger. Most of this originates from uncertainty in bubble volume, which is typically about forty percent of the total volume. The details of how these uncertainties are calculated will be discussed at the end of this chapter.

Figure 5.15 is a plot of reaction rate versus initial metal temperature, and includes all test data. Figure 5.16 also includes all test data, but it is plotted versus water temperature. The smaller error bars are associated with reaction rates from an energy balance, as in the previous two figures. These test results are tabulated in Appendix B for reference.

Two additional figures are included where reaction rate data is plotted versus the average lithium drop temperature (Figs. 5.17 and 5.18). This average is computed by assuming a linear increase in temperature between injection and measurement with the pyrometer. Calculations with the film boiling model suggest that this is a reasonable

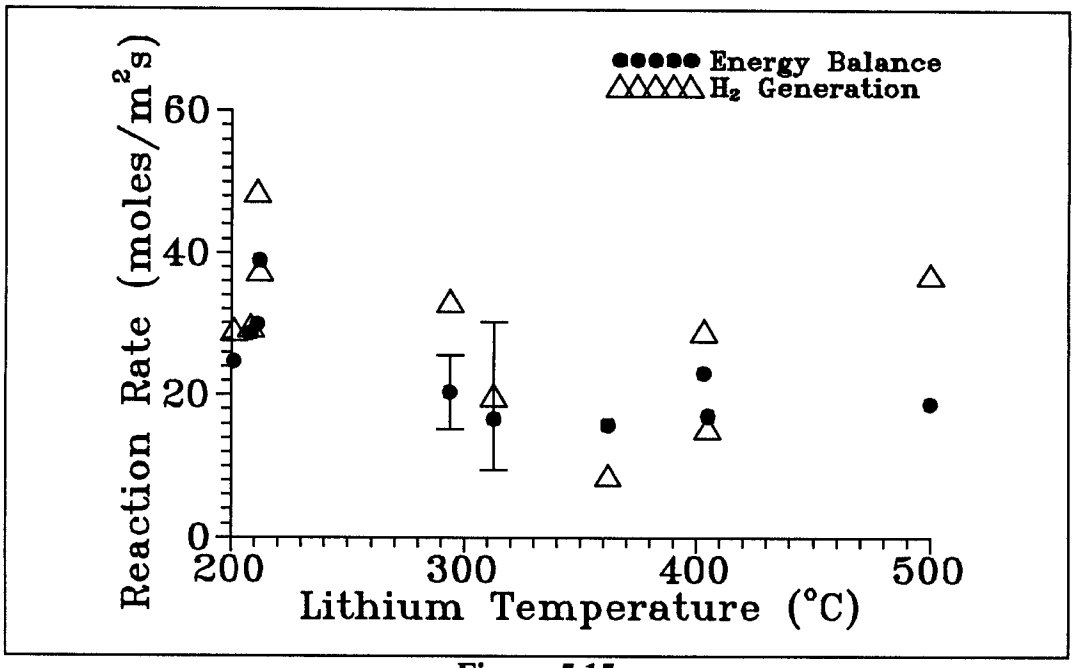

Figure 5.15

Reaction Rate versus Initial Lithium Temperature

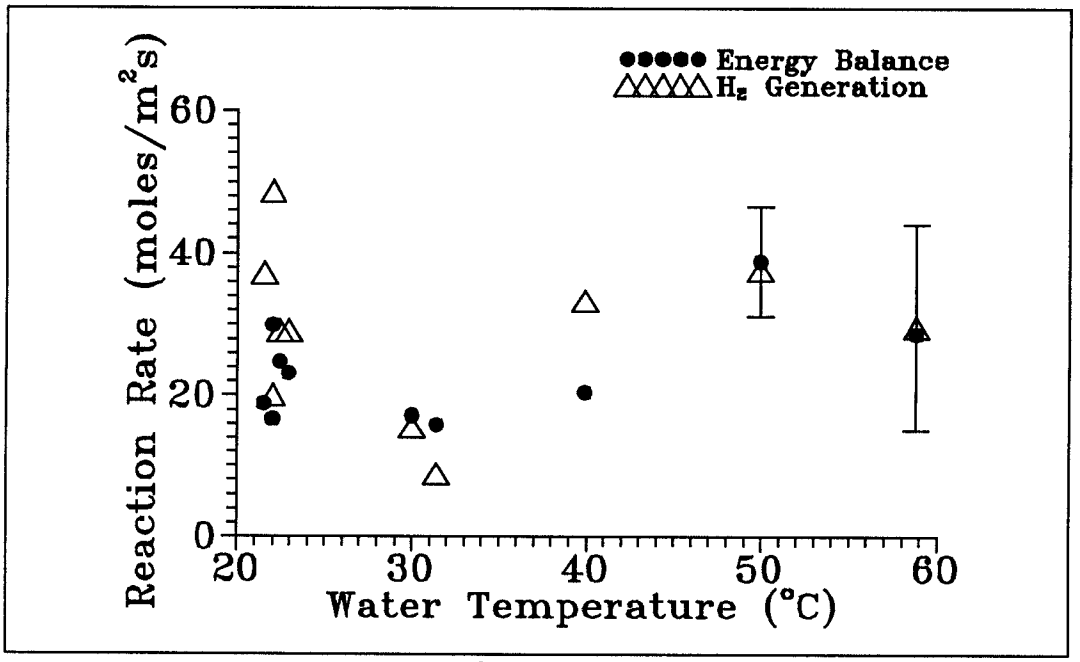

Figure 5.16

Reaction Rate versus Bulk Water Temperature

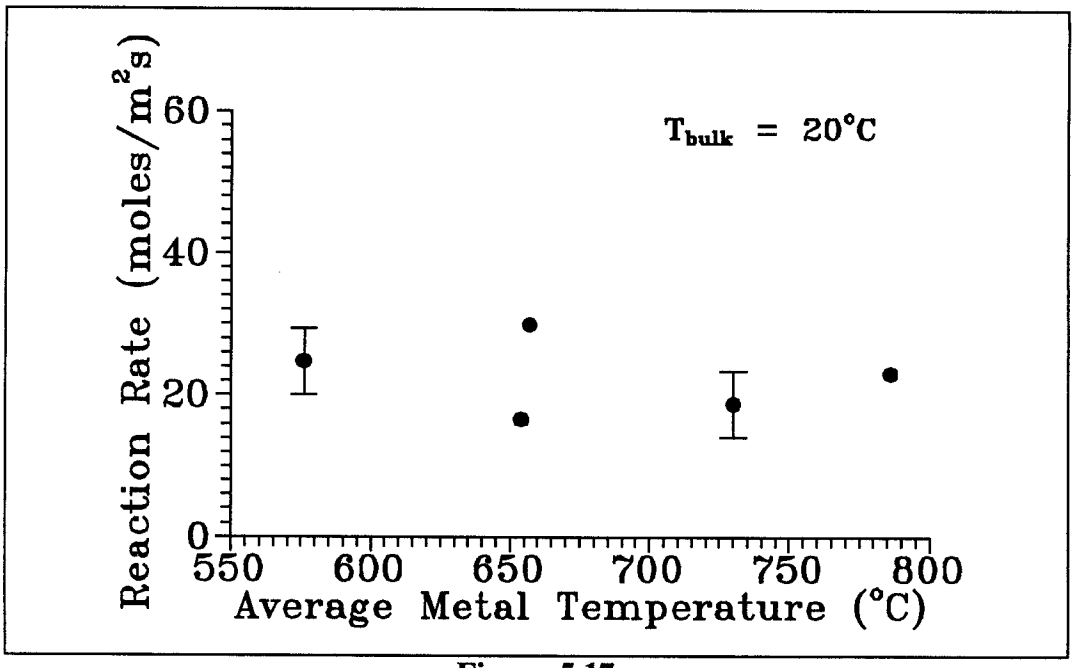

Figure 5.17

Reaction Rate From Energy Balance versus Average Lithium Drop Temperature

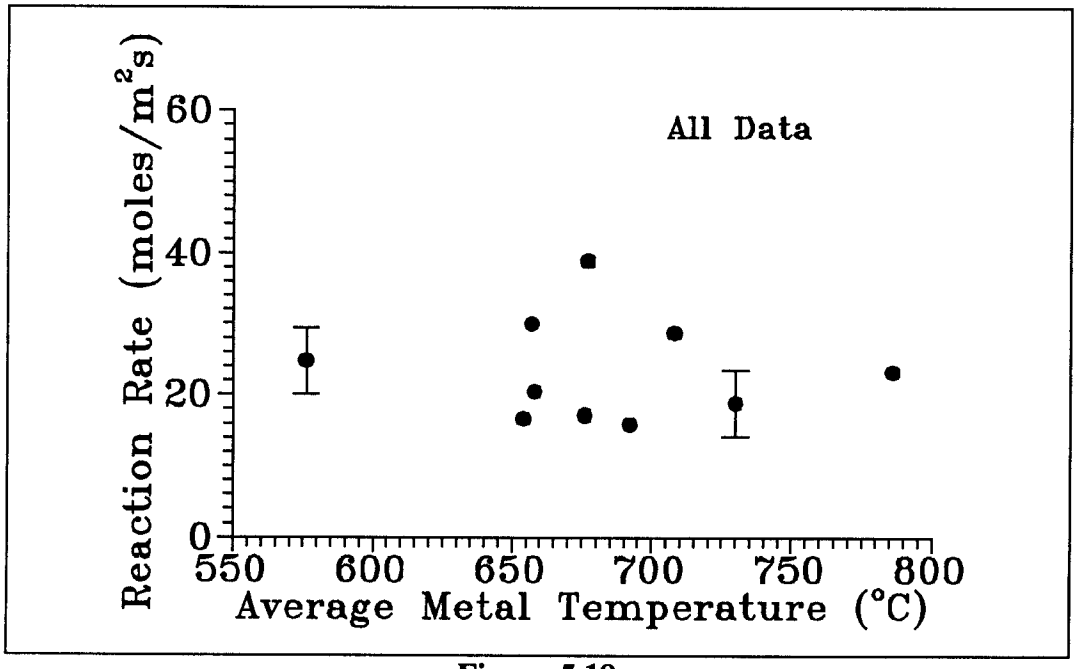

Figure 5.18

Reaction Rate From Energy Balance versus Average Lithium Drop Temperature

assumption. For clarity, only rate measurements from the energy balance have been included in these two plots. Tests with water at a bulk temperature near 20 C are plotted in Figure 5.17. The rate data is seen to be essentially independent of average metal temperature. This is similar to the trend seen for reaction rate as a function of initial metal temperature.

It was shown that the reaction rate is independent of bulk water temperature and so a plot of all test data has been included in Figure 5.18. Again, the reaction rate appears to be independent of the average metal temperature.

Comparison of reaction rate data with previous findings is difficult because quantitative data of this nature is sparse. The reaction rate measurements of steam/nitrogen mixtures with molten lithium, performed at the Massachusetts Institute of Technology (MIT) [23], produced results similar to the measurements made here. The rates measured at MIT were somewhat lower than what has been found here, but both sets of data show the same lack of variation in reaction rate with metal temperature (see Fig. 2.7a). Comparisons between these two works should be made with some caution because the published results from MIT (to date) do not include the use of pure steam. Also, the test geometries are distinctly different. In any event, it is believed that our test geometry, combined with the comparatively short reaction time scale, inherently results in higher reaction rates.

The experimental data compares well to the reaction rate data for sodium acquired at the University of Nottingham [33]. In Figure 5.19, test data for lithium has been plotted along with data for sodium that was shown in Figure 2.14. For clarity,

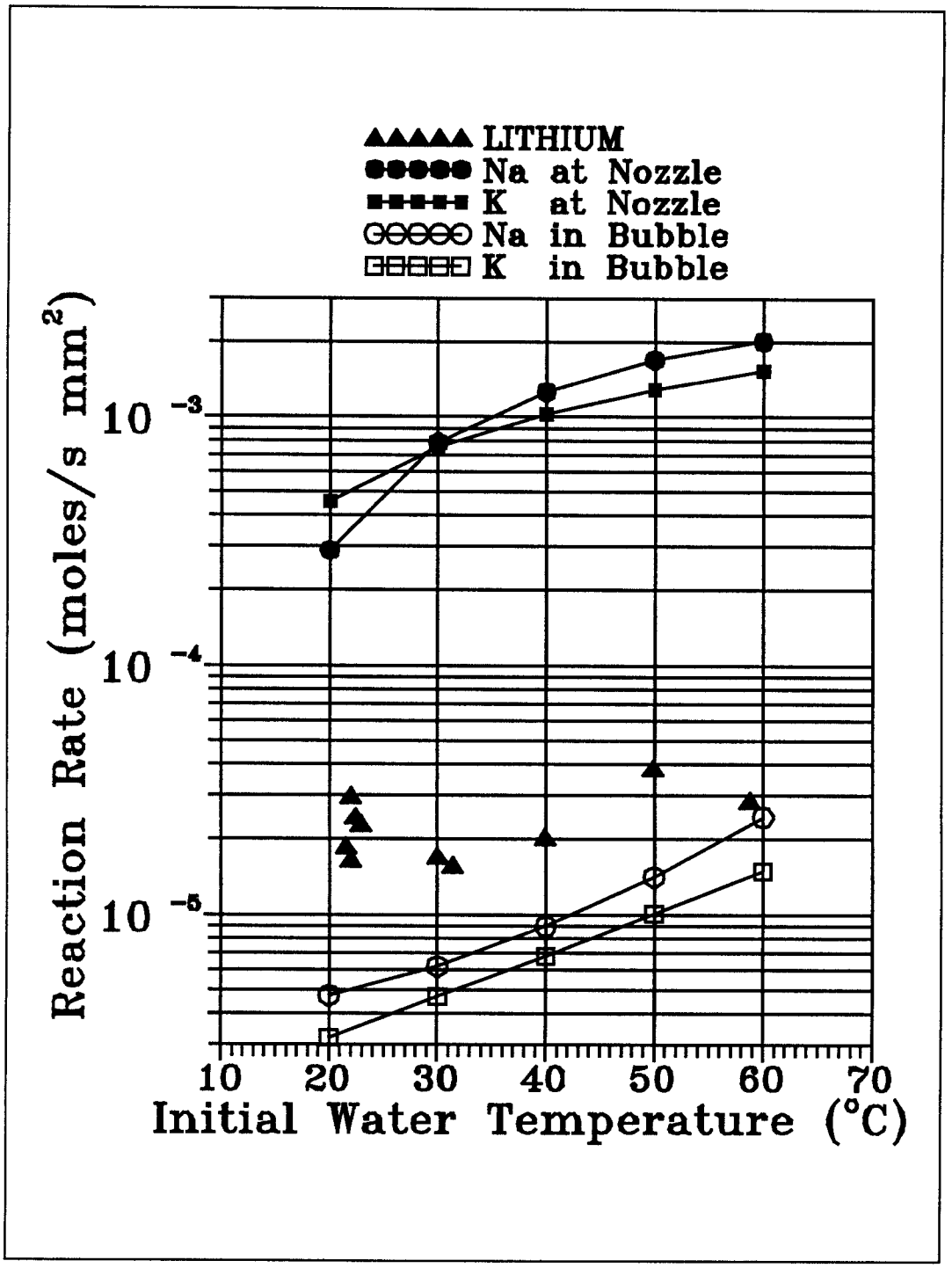

Figure 5.19

Reaction Rates of NaK and Lithium with Water versus Water Temperature

only reaction rates from the energy balance method have been included. The figure shows that lithium reaction rates lie between sodium reaction rates at the nozzle and in the gas bubble. The data from Nottingham show that reaction rates at the nozzle are some 100 times rates in the gas bubble. Our experiments are not able to distinguish between these two rates, but results give average reaction rates that are between the two limits. The sodium data shows an increase with water temperature that we have not observed. As suggested earlier, uncertainty in our data is probably too high to see such an effect. Finally, it is mentioned that injection temperatures for sodium are considerably lower than the tests with lithium, about 130 C.

It must be noted that many tests have been omitted from results shown in the previous plots, and tabulated in Appendix B. The most common reason for omitting a test is because the injector failed to produce a single drop. This mishap becomes evident when checking the wire screen inside the reaction vessel after the test. If multiple drops are found on the screen, the test data is not used to calculate reaction rates. This is because the uncertainty in drop size will be unacceptably large. A second reason for omitting a test is if the pyrometer traces are erratic. When the water path length between the drop and fiber optic cable varies excessively (while the drop is in the field of view of the cable), the pyrometer outputs can be quite noisy. Temperature measurements with these traces require extra interpretation, which is prone to unknown uncertainty. Hence, tests of this nature were also omitted.

V.VI Measurement Error and Uncertainties in Reaction Rates

Each reaction rate data point presented in the previous section is the product of several measurements. These are three or more of the following: bulk water temperature, initial lithium temperature, bubble area, drop surface area and temperature, water path length from pyrometer input to drop, and reaction time. Errors in these measured quantities contribute to error in a calculated reaction rate. In this section, a methodology for calculating the error in each measurement will be given, and such errors will be quantified. These are then used to estimate uncertainty in calculated reaction rates.

Initial water and lithium temperatures are measured with four and eight thermocouples, respectively. The calculation of uncertainty in the initial reactant temperatures has been described in section 3.5. The same procedure will be used here.

V.VI-I Uncertainty in Reaction Rate- I

The first method of calculating a reaction rate uses measurements of integral hydrogen production, and the relation given in Equation 5.12. The major sources of uncertainty come from errors in the lithium drop area and bubble volume. Their influence on uncertainties in calculated reaction rates can be approximated with an error propagation formula [51]:

$$\sigma_K^2 \approx \left(\frac{\partial K}{\partial V_{bub}}\right)^2 \sigma_V^2 + \left(\frac{\partial K}{\partial R_{drop}}\right)^2 \sigma_R^2 \qquad (5.15)$$

Uncertainty contributed by error in measuring the time of reaction is small compared

to the other two sources of uncertainty, and will be neglected.

The measurement of projected bubble area is used to calculate bubble volume, which is then a direct indication of total hydrogen production. The computation requires the assumption of a spherically symmetric bubble shape. Given this assumption, errors are still present when the video and digitization system is used to measure the cross-sectional area of a sphere. Three sources of error are identified for this system. First, error exists because the digitization process has limited accuracy due to finite resolution: 640x400 pixels. Also, the technique of enhancing the contrast to distinguish between bubble and background is an imperfect process. Errors from these sources are deemed to be relatively small.

The third source of error occurs because the bubble is not in the same plane as the reaction vessel window, and so the area scale is incorrect. This is due to the fact that depth perception shrinks the size of the window relative to the sphere, and so the area scale in the digitized pictures is too small. This effect results in a calculated bubble volume that is too large. This third source of error is non-negligible, and must be considered.

Error of this nature could be essentially eliminated by putting the camera at a large distance from the reaction vessel, but this was not a practical option. Instead, a correction factor is obtained by video system calibration. This is done by using the system to measure the cross sectional areas of spheres with known sizes. Three spheres, with diameters of 42, 68, and 98 mm, were used in the calibration tests. These were placed inside the reaction vessel, midway between the front and back window, and

filmed with the video camera. The pictures were digitized, and projected areas were used to calculate the radius and volume of each sphere.

Figure 5.20a shows the radius of each sphere calculated with the video system and digitization software. This is plotted versus the radius measured with a caliper, which will be regarded as the 'true' radius. Uncertainty in caliper measurements are considered to be mostly from asymmetries in the test spheres. This was estimated to be about 0.5 mm for each sphere, and the error bars reflect this. Figure 5.20a shows that the video system always gives a radius that is slightly larger than the measured radius. This enlargement does not vary with sphere radius, and is outside the estimated uncertainty range. This verifies that there is systematic error in the calculated radius. The calculated volume is seen to follow the same pattern (Fig. 5.20b), though the percentage error has increased.

Results of these tests are used to establish a correction factor for re-scaling the bubble radius. For each experimental test, a correction factor of 0.97 will be used to decrease the calculated bubble radius. Finally, note that bubbles observed in experiments range in size from about 30 mm to 60 mm diameter.

Introducing a scaling factor into calculations of bubble volume reduces the systematic error described at the beginning of this section. The fractional error in bubble radius from this effect will be reduced to less than one percent. However, random errors in bubble volume have not been quantified. Given the assumption that the bubble can be calculated by assuming a spherical (or hemispherical) shape, there is still random error associated with assuming a mean radius and using it to calculate

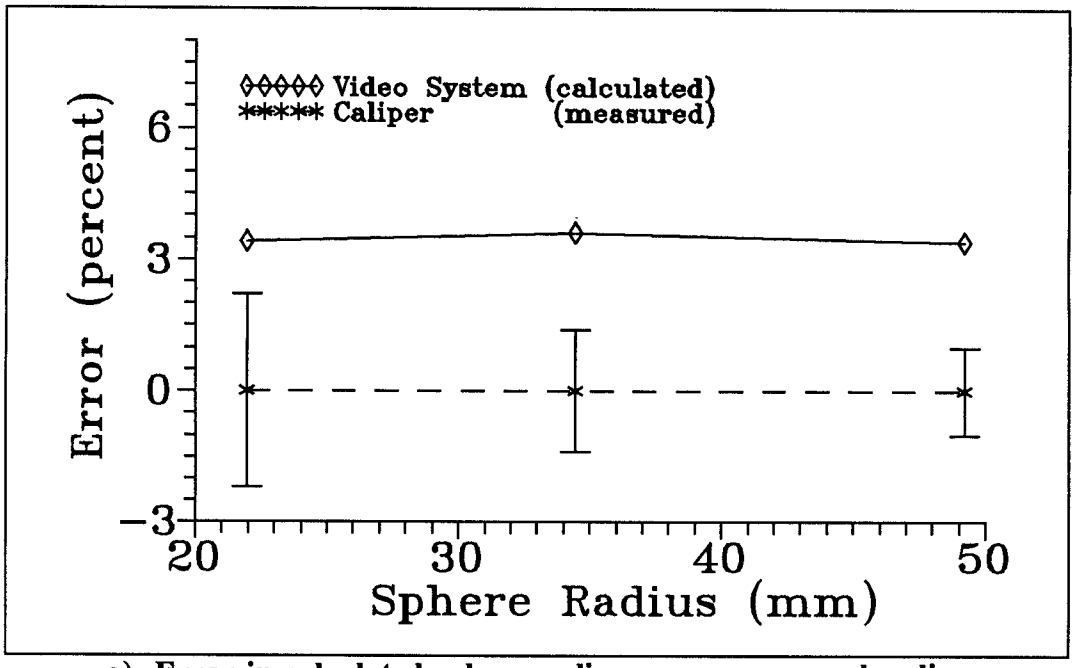

a) Error in calculated sphere radius versus measured radius

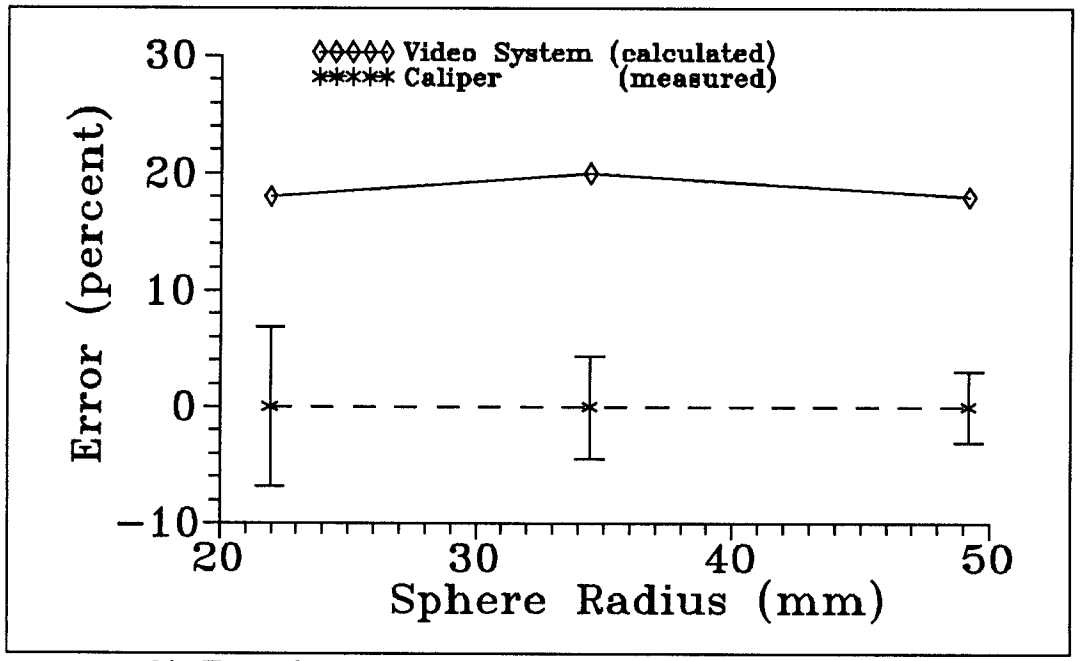

b) Error in calculated volume versus measured radius

Figure 5.20
Error in Radii and Volumes of Test Spheres versus Measured Sphere Radius

bubble volume. Unfortunately, this will be larger than the systematic error, and it is difficult to quantify. This error is certainly greater than the estimated 0.5 mm that was chosen for caliper measurements in the calibration tests. At the same time, it should be considerably less than the bubble radius, which ranges between about 15 mm and 30 mm. It is estimated that the error in bubble radius is four times the error assumed for caliper measurements, or about 2 mm. When uncertainty in hydrogen production is evaluated, the variance in radius is set equal to this value.

The error in drop diameter is difficult to quantify. The injection system designed for these experiments is incapable of injecting the entire amount of lithium stored within the injector. Most of the lithium remains inside the nozzle after injection. Because of this, the drop volume must be calculated by subtracting the free volume in the nozzle from the total volume of lithium present before injection. Since a drop forming at the nozzle exit does not separate from the nozzle in the same manner for every injection, there is error in calculating the drop volume in this fashion. When a drop is created, it may separate from the nozzle with somewhat more (or less) lithium than calculated. The maximum difference is estimated to be equal to an imaginary hemisphere, with a diameter equal to the inner diameter of the nozzle. The volume of this hemisphere is set equal to the error in drop volume. This error is propagated through the formula that relates the volume of a sphere with its radius, resulting in an estimation of variance in drop radius.

V.VI-II Uncertainty in Reaction Rate- II

When reaction rates are calculated from an energy balance on the drop, error arises from three primary sources: the temperature measurement, the assumption of a uniform temperature profile across the drop, and from calculating energy losses from the drop surface. Using the error propagation formula again, uncertainty in the reaction rate is written in terms of these quantities:

$$\sigma_K^2 \approx \left(\frac{\partial K}{\partial T_{drop}}\right)^2 \sigma_T^2 + \left(\frac{\partial K}{\partial R_{drop}}\right)^2 \sigma_R^2 + \left(\frac{\partial K}{\partial h}\right)^2 \sigma_h^2 \qquad (5.16)$$

The uncertainty due to error in measuring the reaction time has again been neglected.

The energy lost by the drop is small in comparison to energy generated by the reaction, which is retained in the drop. In addition, the heat transfer coefficient is fairly well known. Consequently, the uncertainty in reaction rate contributed by error in the calculated energy lost by the drop is small compared to other sources, and will be neglected also.

The second source of error in reaction rate calculations arises when the actual temperature distribution is nonuniform. For conditions in these experiments, the drop temperature is rising because of heat released at the surface, and so the temperature of the drop center is never greater than the surface temperature. The result is that energy gained by the drop is always overestimated by assuming a uniform temperature equal to the surface temperature. This results in an overestimation of the reaction rate.

Considering that all measured drop temperatures are similar, it is likely that the temperature gradient across the drop is greater for lithium injected at lower

temperatures. Thus some systematic error may exist in calculating the reaction rates with a single drop temperature. The error should increase as the injection temperature decreases. This, in fact, may account for the apparent increase in reaction rate as the initial lithium temperature is decreased (see Fig. 5.15). Elimination of this error is beyond the scope of this study. However, an upper bound estimate to the reaction rate is obtained by neglecting non-uniformities in temperature distribution. This is acceptable for this study. Moreover, it is believed that uncertainties related to this effect are small compared to uncertainties from error in measurements of drop temperature and radius. These are now discussed.

Error analysis of the energy balance focuses on temperature measurements. Starting with Equation 5.10, the drop temperature is written in terms of the measured parameters and calibration constant:

$$T = C_2\left[\frac{1}{\lambda_1} - \frac{1}{\lambda_3}\right]\left[\ln\left(\Re\frac{\Psi_3}{\Psi_1}\left(\frac{\lambda_3}{\lambda_1}\right)^{-5}\right) + x(a_3 - a_1)\right]^{-1} \qquad (5.17)$$

Uncertainty in temperature arises from three sources of error: pyrometer calibration, measurement of the water path length, and measurement of the absorption coefficients of water. The signal to noise ratios for pyrometer measurements are large, typically more than 100, and so fractional error in the measured voltage ratio, $\Re$, will be small. This contribution to uncertainty in the temperature measurement is small compared to the other sources, and so it is neglected.

Given the preceding assumptions, the error propagation formula is used to estimate the overall uncertainty in temperature measurements:

$$\sigma_T^2 \approx \left(\frac{\partial T}{\partial x}\right)^2 \sigma_x^2 + \left(\frac{\partial T}{\partial a}\right)^2 \sigma_a^2 + \left(\frac{\partial T}{\partial \Psi}\right)^2 \sigma_\Psi^2 \qquad (5.18)$$

where **a** represents the difference in absorption terms, a_1 - a_3, and Ψ is the calibration constant Ψ_1 / Ψ_3. The methodology for estimating σ_b will be described next.

The purpose of calibrating the pyrometer with a black body was to determine the constants Ψ_i / Ψ_j. Errors in these constants influence the temperature measurements. To obtain the constant Ψ_1 / Ψ_3, a regression equation was fitted to the calibration data using the method of least squares. This equation may be written in the following form:

$$\ln\left[\frac{V_1}{V_3}\right] = \ln\left[\frac{\Psi_1}{\Psi_3}\left(\frac{\lambda_1}{\lambda_3}\right)^{-5}\right] + \frac{m}{T} \qquad (5.19)$$

where **m** is the slope of the line, **T** is temperature in degrees Kelvin, and the logarithmic term on the right-hand side is the y-intercept of the equation. The first step in finding uncertainty in the calibration constant is to estimate the variance in data about the regression equation. This is calculated from the following [51]:

$$\xi_i = -\ln\left[\frac{V_{1i}}{V_{3i}}\right] + \ln\left[\frac{\Psi_1}{\Psi_3}\left(\frac{\lambda_1}{\lambda_3}\right)^{-5}\right] + \frac{m}{T_i} \qquad (5.20)$$

The term ξ_i is the residual remaining between an individual value of the voltage ratio and the regression equation. The sum of the residuals is used to calculate sample variance, σ^2 :

$$\sigma^2 = \frac{1}{N}\sum_i^N \xi_i^2 \qquad (5.21)$$

where **N** is the number of data points used to calculate the regression equation. This

is related to the variance in the y-intercept of the regression equation by the following relation:

$$\sigma_b^2 = \frac{\sigma^2 \sum_i^N \frac{1}{T_i^2}}{N \sum_i^N \frac{1}{T_i^2} - \left(\sum_i^N \frac{1}{T_i} \right)^2} \qquad (5.22)$$

where the subscript **b** refers to the y-intercept of the regression equation. These equations were used with calibration data to determine the uncertainty in Ψ_1 / Ψ_3. It was found that σ_b is approximately one percent. This translated into an uncertainty in Ψ_1/Ψ_3 of about two percent. The uncertainty in Ψ_1/Ψ_3 is a magnified version of the uncertainty in **b**, since the two are related through an exponential term. The value of two percent will be used in the error propagation formula for determining total uncertainty in temperature measurements.

Another source of uncertainty in the temperature measurement comes from error in the measured value of a_1 - a_3, which is referred to by the single symbol **a** in this discussion. The absorption term was obtained by pyrometer calibration with water, as described in section 5.2-3. The best fit lines shown in Figure 5.6 were obtained by the least squares method. The slope of the line plotted for V_1/V_3 is equal to the measured value of **a**. Uncertainty in this slope is found with the same technique used to find uncertainty in **b**. The new regression equation is written as:

$$\ln\left[\frac{V_{1i}}{V_{3i}}\right] = b + a x_i \qquad (5.23)$$

Where x_i corresponds to measured values of the water path length. Now relations

analogous to Equations 5.20 and 5.21 can be used to calculate the sample variance. The variance is related to uncertainty in **a** by the following expression [51]:

$$\sigma_a^2 = \frac{N\sigma^2}{N\sum_i^N x_i^2 - \left(\sum_i^N x_i\right)^2} \tag{5.24}$$

The uncertainty in **a** was calculated with these equations and the data for V_1/V_3 that was shown in Figure 5.6. The uncertainty in **a** is found to be five percent, and this value will be used in calculations of total uncertainty in temperature measurements.

Finally, the major source of uncertainty in temperature measurements is associated with error in the measured path length of water separating the lithium drop and fiber optic cable input. This path length is obtained from measuring pictures of the hydrogen bubble. The major difficulty is that the actual location of the lithium drop can not be found on these pictures. The bubble forms a dark silhouette because of strong back-lighting, and the lithium within the bubble is not visible. However, the drops may (sometimes) be seen on videotape when they are glowing orange. Reviewing these tapes has shown that the geometry does not always correspond to the simple picture of a gas bubble with a lithium drop at the center of the bubble base. The drop may be on the near or far side (from the pyrometer) of the bubble. Also, the base of the bubble may be somewhat concave in shape. This results in a water path length that is dependent upon the location of lithium within the bubble. Intuitively, the upper bound on error in water path length is equal to the bubble diameter. However, it would not be appropriate to use such an upper limit for an estimate of σ_x. Test observations suggest that a

reasonable, though still conservative, estimate of σ_x would be the bubble radius. This is the length scale chosen to calculate error in water path length.

In closing, it is noted that path length through the bubble has not been included in calculations of signal absorption. This implicitly assumes that absorption of the radiation signal in the bubble may be neglected. This is a good assumption because water vapor will produce a much smaller change in signal ratio than liquid water when the path lengths are comparable (as they are here).

VI SUMMARY AND CONCLUSIONS

This study of molten-lithium/water interactions has included both experimental and analytical investigations. Experiments were divided into two series of tests. The first series involved injecting molten lithium droplets into water and making qualitative observations of the reaction. The second test series was used to make reaction rate measurements. Along with these experiments, a mathematical model of the lithium/water reaction was developed to examine and explain experimental findings. This summary is divided into three subsections; the first discusses scoping test results, the second covers conclusions from calculations with the mathematical model, and the last section will summarize findings from reaction rate measurements. Recommendations for future work will follow these summaries.

VI.I Scoping Tests

The first series of experiments consisted of injecting a droplet of lithium into the bottom of a reaction vessel filled with water. A typical diameter for this drop is approximately 10 mm. The lithium temperature at injection ranged from 200 C to 500 C, and water temperature was varied between 20 C and 70 C.

The experiments revealed that the reaction of molten lithium droplets with water can be explosive in nature. On a plot of initial water temperature versus initial lithium temperature, it is seen that a threshold for explosive reactions exists. Occurrence of

these energetic reactions is unlikely below the threshold, but they are common above it. When the initial lithium temperature is near 400 C, explosive reactions arise for water temperatures above about 50 C. For initial metal temperatures approaching 500 C, the explosive reactions are seen for water temperatures near 35 C. The frequency of explosive reactions dwindles as the initial metal temperature falls below 400 C. For the conditions studied, high initial metal temperature is the most important predictor of an explosive lithium/water reaction.

Pressures were measured at the reaction vessel wall during these tests, and peak pressures near 4 MPa were recorded for the most violent reactions. A clear trend in the experimental data showed that peak pressures increased as the initial metal temperature increased. Clearly these explosions are not caused by the ignition of hydrogen and atmospheric oxygen. The event takes place soon after injection, ~ 0.5 s, and the lithium drop is still well below the water surface at this time. The pressure transients are the result of a sudden increase in the overall reaction rate, which causes an explosive generation of hydrogen and water vapor.

VI.II Mathematical Model

A mathematical model of the lithium water reaction was developed to analyze and explain experimental findings. The model numerically calculates transient conduction heat transfer through a spherical drop using a one-dimensional finite-difference method. Convection, conduction, and radiation losses from the drop surface are computed during the transient. In addition, the mass transfer rate of water vapor to

the metal surface is calculated. This is used to compute the chemical reaction rate of lithium and water at the drop surface. Two different mass transfer models were incorporated into this scheme.

The first mass transfer model used stagnant diffusion across a spherically symmetric, gaseous film of hydrogen and water vapor to compute the reaction rate. Calculations with this model showed that reaction rates are much too slow to heat the drop to the boiling point. For this reason, we believe that stagnant diffusion mass transfer cannot explain the ignition phenomenon observed in the scoping tests.

The second mass transfer model uses a film boiling model to find reaction rates. The mass transfer rates computed with this model are much greater than those with stagnant diffusion, ranging from about 40 to 300 times as large. When mass fluxes are this large, the drop can heat to the boiling point in a very short time, less than 0.5 s.

Combining results of the scoping tests and computations with the numerical model, a hypothesis regarding the mechanism responsible for explosive reactions was formed: if a significant portion of the drop can heat to the saturation temperature before the film grows enough to inhibit further mass transfer, ignition occurs. Drops injected at high temperatures will reach the lithium saturation temperature sooner than drops injected at lower temperatures. For an explosive reaction to occur, a 'significant' portion of the drop must reach the saturation temperature before the film has grown too thick and reduced the reaction rate. The mathematical model lacks the sophistication necessary to indicate what constitutes a significant portion of the drop. However, the simple criteria of the drop surface reaching the saturation temperature was used

successfully to predict trends found in the scoping test data. It was shown that our ignition hypothesis is consistent with both experimental data and trends observed from computations with the model.

VI.III Reaction Rate Measurements

A second series of experiments with molten lithium and water were conducted to measure the reaction rate of the metal. These experiments focused on nonexplosive reactions. An approximately 6 mm diameter drop of lithium is injected into water, and the droplet temperature is measured with a pyrometer after about 0.5 s. While temperature is measured, the reaction is photographed to determine the amount of hydrogen evolved. The reaction rate in each test is calculated with two independent methods: the first uses video tape of the reaction to find the amount of hydrogen evolved, and the second finds the amount of lithium reacted by performing an energy balance on the drop. Initial lithium temperatures in these tests ranged from 200 C to 500 C, while the bulk water temperature was varied between 20 C and 60 C. The combinations of initial reactant temperatures were chosen to stay below the explosive reaction threshold discovered in the first test series.

Measured reaction rates ranged from about 10 to 40 moles/m^2s for both the energy balance and hydrogen production methods. Plots of the reaction rates were made versus bulk water and initial metal temperature in search of trends in the data. No significant trends were apparent. The numerical model predicted that reaction rates should not be a function of initial metal temperature, which agrees with experimental

data. However, the model predicted that rates should increase with water temperature, an effect that is not revealed by the experimental data. It is believed that uncertainty in the reaction rate measurements is too large to observe the increase in reaction rate with water temperature (if, in fact, such a trend exists). Uncertainties in the reaction rate measurements from hydrogen production were primarily from uncertainties in determining the bubble volume. For the energy balance method, most of the uncertainty arose from inaccurate measurements of the path length of water between the pyrometer and lithium drop.

There is no quantitative data of the reaction rate of molten lithium and water vapor currently available for comparison with our test data. Instead, our experimental results were related to some studies reviewed in chapter 2. The comparisons are imperfect because of fundamental differences between the studies; in either the reactants used or the experimental configurations. Still, given this qualification, the reaction rate measurements and trends observed in the data obtained in this study showed reasonable agreement with previous work. In particular, reaction rate measurements for sodium, performed at the University of Nottingham, compared well with our findings.

VI.IV Recommendations for Future Research

The discovery of a temperature threshold for explosive lithium/water reactions is an interesting one. This threshold could be mapped in a more complete fashion than we have done for this study. The upper limit of temperature for injecting the lithium was about 500 C. This is acceptable for fusion applications, but a wider temperature

range for the water should be considered.

The reaction rate of lithium and water was measured in this study but additional data is desirable. Measurements could be made over a wider range of initial reactant temperatures. In addition, minor changes in instrumentation, the pyrometer in particular, will reduce uncertainty in the reaction rate measurements. These improvements may make it possible to observe trends that are not apparent in the results of this study.

The mathematical model developed for analysis of experimental results is adequate for this study, but it can be improved. The most significant improvement would be the addition of a new mass transfer model. It should model the film boiling-type mass transfer that occurs soon after injection, yet account for the growing hydrogen film that reduces the reaction rate at later stages. Another significant addition would be a model that considers the vapor pressure of lithium at the metal surface. Evaporation of lithium into the gaseous film will give the chemical reaction a different character than the simple surface reaction that has been modelled here. The new model could consider chemical reaction and energy release in the film, and its effect on water vapor pressure at the film/water interface.

Measuring the metal temperature of a metal/water reaction *after* the reaction has been initiated is a difficult task, and is not often attempted in experiments of this nature. The use of a radiation ratio thermometer for molten-metal temperature measurements through liquid water is uncommon, if not unique. The possibility of incorporating this type of instrumentation into other, similar experiments should be considered. This measurement provides useful information that has not been previously available.

APPENDIX A

TEST NUMBER	INITIAL WATER TEMPERATURE (C)	INITIAL METAL TEMPERATURE (C)	PEAK EXPLOSION PRESSURE (MPa)
11	25.6 ∓2.2	532. ∓4.	-
12	53.4 ∓2.2	403. ∓3.	2.04
13	26.6 ∓2.2	370. ∓4.	-
14	37.0 ∓2.2	400. ∓3.	-
15	52. ∓2.	394.∓11.	UNKNOWN
16	35.9 ∓2.2	318. ∓2.	-
17	60.1 ∓2.2	332. ∓2.	0.20
18	51.9 ∓2.2	331. ∓2.	-
19	54.8 ∓2.2	404. ∓4.	-
20	60.2 ∓2.2	435. ∓3.	3.0
22	41.1 ∓2.2	222. ∓7.	-
23	40.7 ∓2.2	266. ∓4.	-
24	34.2 ∓2.2	267. ∓3.	-
25	31.6 ∓2.2	263. ∓3.	-
27	31.4 ∓2.2	199. ∓3.	-
29	40.6 ∓2.2	292. ∓3.	-

Figure A.1

Tabulated Data: Scoping Tests

TEST NUMBER	INITIAL WATER TEMPERATURE (C)	INITIAL METAL TEMPERATURE (C)	PEAK EXPLOSION PRESSURE (MPa)
30	40.8 ∓2.2	340. ∓2.	-
31	40.8 ∓2.2	384. ∓3.	-
32	42.2 ∓2.2	435. ∓7.	3.9
33	32.2 ∓2.2	296. ∓4.	-
34	30.3 ∓2.2	231. ∓4.	-
35	30.6 ∓2.2	341. ∓4.	-
36	30.6 ∓2.2	424. ∓4.	-
37	31.0 ∓2.2	454.∓10.	-
38	30.2 ∓2.2	506. ∓5.	-
39	37.0 ∓2.2	453. ∓5.	4.1
40	51.5 ∓2.2	263. ∓8.	-
41	60.0 ∓2.2	215. ∓2.	-
42	59.2 ∓2.2	256. ∓3.	-
43	60.9 ∓2.2	305. ∓5.	_
44	70.4 ∓2.2	255. ∓6.	0.33
45	70.8 ∓2.2	309. ∓8.	-
46	69.9 ∓2.2	357. ∓4.	-
47	70.4 ∓2.2	410. ∓8.	-

Figure A.2

Tabulated Data: Scoping Tests

TEST NUMBER	INITIAL WATER TEMPERATURE (C)	INITIAL METAL TEMPERATURE (C)	PEAK EXPLOSION PRESSURE (MPa)
48	36.8 ∓2.2	469.∓12.	0.24
49	41.2 ∓2.2	522.∓10.	-
50	50.9 ∓2.2	444. ∓6.	-
51	47.0 ∓2.2	442. ∓7.	-
52	51.2 ∓2.2	441. ∓8.	-
5*	26.7 ∓2.2	449. ∓8.	UNKNOWN
14*	29.4 ∓2.2	202. ∓8.	1.2

Figure A.3

Tabulated Data: Scoping Tests

Tests 11-25 are with the stainless steel bellows. All subsequent tests are with the injector shown in Figure 3.2. Test numbers 11-15 are with the acrylic reaction vessel. Tests 16-52 are with the aluminum reaction vessel. The test numbers written with an asterisk superscript denote tests with the reaction vessel described in chapter 4.

Pressures are labelled 'UNKNOWN' when an explosion occurs but equipment failure caused a loss of pressure recordings (test 15) or the pressure transducer failed to operate properly (test 5*). Uncertainty for all pressure readings is approximately ∓2%.

APPENDIX B

TEST #	INITIAL WATER TEMP. (C)	INITIAL METAL TEMP.(C)	MEASURED DROP TEMP.(C)	RATE OF TEMP. CHANGE (C/s)	LENGTH OF TRANSIENT(s)
9	39.9 ∓2.2	294. ∓2.	1021. ∓183.	1268.∓397.	0.574
18	22.0 ∓2.2	313. ∓2.	994. ∓159.	948. ∓211.	0.718
19	22.0 ∓2.2	211. ∓2.	1103. ∓176.	1866. ∓624.	0.478
20	22.9 ∓2.2	403. ∓4.	1168. ∓210.	1394. ∓457.	0.549
22	30.0 ∓2.2	405. ∓3.	948. ∓132.	937. ∓226.	0.580
25	22.4 ∓2.2	201. ∓2.	952. ∓123.	1445. ∓361.	0.520
27	31.4 ∓2.2	362. ∓3.	1021. ∓133.	861. ∓146.	0.766
30	49.9 ∓2.2	212. ∓5.	1142. ∓171.	2374. ∓908.	0.392
31	58.8 ∓2.2	208. ∓2.	1207. ∓229.	1729. ∓568.	0.578
34	21.5 ∓2.2	500. ∓4.	961. ∓134.	1022. ∓284.	0.474

Figure B.1

Tabulated Data: Reaction Rate Measurement Tests

TEST #	Li DROP RADIUS (mm)	BUBBLE VOLUME (ml)	REACTION RATE1 (ENERGY BALANCE) MOLES/M³ S	REACTION RATE2 (H_2 PRODUCTION) MOLES/M³ S
9	3.8 ∓.6	48. ∓20.	20.4 ∓5.2	33. ∓18.
18	4.1 ∓.5	38. ∓17.	16.6 ∓3.8	20. ∓10.
19	4.0 ∓.6	58. ∓14.	29.9 ∓6.5	49. ∓18.
20	3.9 ∓.5	40. ∓18.	23.1 ∓6.1	29. ∓16.
22	4.2 ∓.5	26. ∓13.	17.1 ∓3.8	15. ∓8.7
25	4.2 ∓.5	42. ∓11.	24.7 ∓4.6	29. ∓10.
27	4.2 ∓.5	20. ∓11.	15.8 ∓3.0	8.8 ∓5.4
30	4.0 ∓.5	46. ∓12.	38.8 ∓8.0	37. ∓14.
31	4.0 ∓.6	56. ∓23.	28.6 ∓6.8	29. ∓15.
34	4.3 ∓.5	52. ∓14.	18.8 ∓4.6	37. ∓12.

Figure B.2

Tabulated Data: Reaction Rate Measurement Tests

APPENDIX C

$\Psi_1/\Psi_2 = 1.190$

$\Psi_1/\Psi_3 = 2.574 \mp 2\%$

$\Psi_2/\Psi_3 = 2.155$

$C_2(1/\lambda_1 - 1/\lambda_2) =$ 1.595e3 K (within $\mp 3.6\%$ of theoretical value)

$C_2(1/\lambda_1 - 1/\lambda_3) =$ 2.420e3 K (within $\mp 2.0\%$ of theoretical value)

$C_2(1/\lambda_2 - 1/\lambda_3) =$ 0.8245e3 K (within $\mp 0.16\%$ of theoretical value)

$a_1 - a_2 = -0.3299\ cm^{-1}$

$a_1 - a_3 = -0.0916\ cm^{-1} \mp 5\%$

$a_2 - a_3 = 0.2383\ cm^{-1}$

Error analysis performed for data pertinent to V_1/V_3 only.

Figure C.1

Pyrometer Calibration Constants

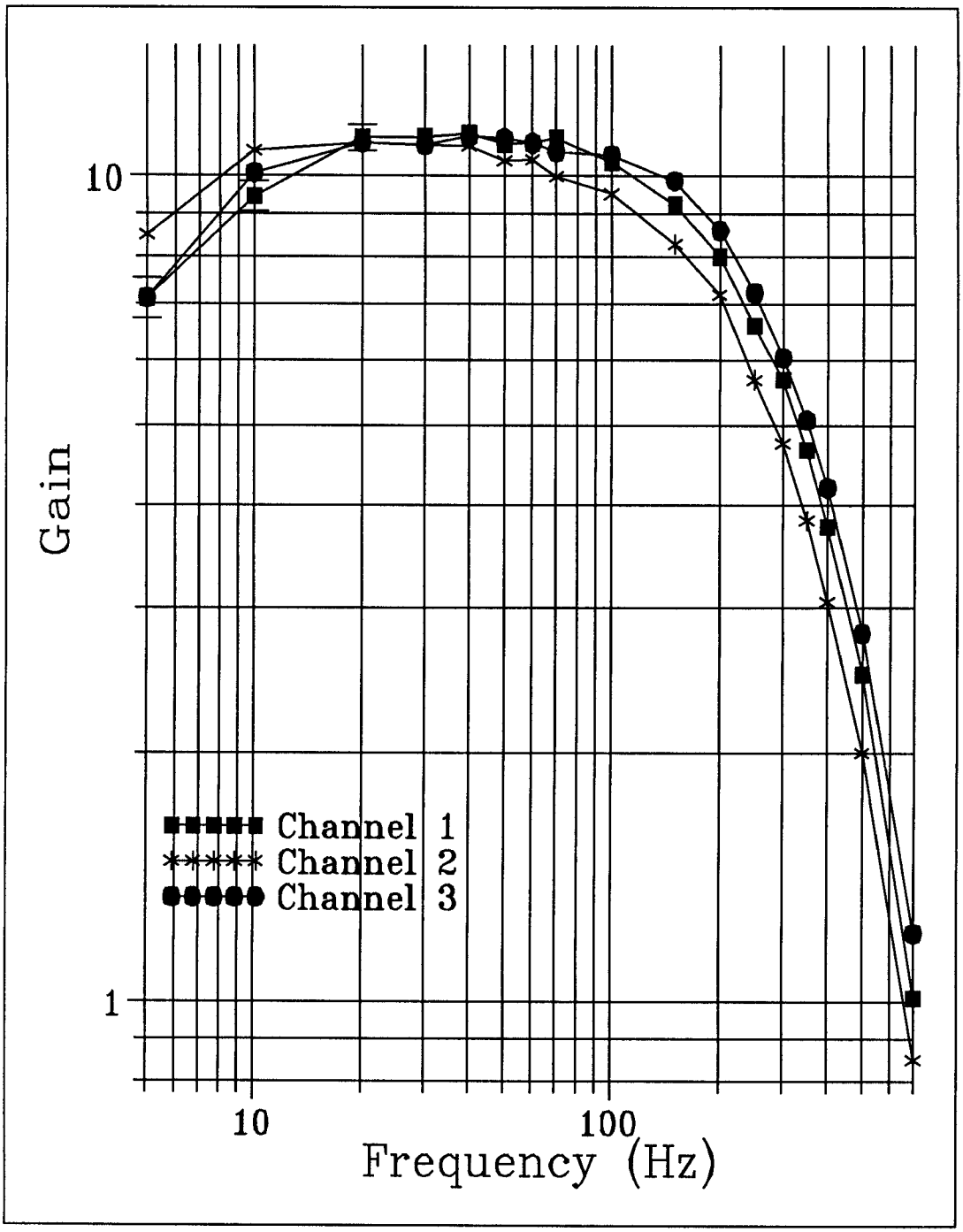

Figure C.2

Relative Gain of Each Pyrometer Channel versus Signal Frequency
(Feedback Resistance = 100k ohms)
(Monolithic Amplifiers and Low-Pass Filters Included in Test)

Component Description	Nominal Performance Characteristics	Manufacturer
Silicon Photodiode Detector (Photovoltaic)	Photosensitive Area- 5 mm^2 Spectral Range- 300-1100 nm Responsivity at peak- 0.5 A/W Rise Time- 75 ns Noise Equivalent Power at Peak- 1.7 $x10^{-14}$ $W/Hz^{1/2}$	Oriel Corp. 250 Long Beach Blvd. P.O. BOX 872 Stratford CT. 06496
Trifurcated Fiber Optic Cable	Numerical Aperture- 0.55 Transmittance Band- 400-1500 nm Peak Transmittance- 60% Fiber Material- glass	
Narrow Band Pass Filters	Central Wavelengths- 900, 1000, 1060 nm Full Width at Half Maximum Transmission- 10 nm Percentage Transmission at Peak- 50 %	Esco Products 171 Oak Ridge Rd. Oak Ridge, NJ 07438
Monolithic Amplifiers	(Gain has been hard-wired to 1000) CMRR @ 30 Hz- 100 dB Input Impedance- 10^{10} ohms	Brown Burr Inc. 6370 S. Tuscon Blvd. Tuscon, AZ 85706

Figure C.3

Supplementary Information for Major Pyrometer Components

REFERENCES

[1] WELLS W. M., *ORNL Fusion Power Demonstration Study: Lithium as a Blanket Coolant*, Oak Ridge National Laboratory Report ORNL/TM-6214 (April 1978).

[2] FRAAS A. P., *Analysis of a Recirculating Lithium Blanket Designed to Give a Low Magnetohydrodynamic Pumping Power Requirement*, Oak Ridge National Laboratory Report ORNL/TM 3756 (Sept. 1972).

[3] JEPPSON D. W. et al., *Fusion Reactor Breeder Material Safety Compatibility Studies*," Nuclear Technology/Fusion, Vol. 4 (Sept. 1983): pp. 277-87.

[4] HOLROYD R. J., MITCHELL J. T. D., *Liquid Lithium as a Coolant for Tokamak Fusion Reactors*, Nuclear Engineering and Design/Fusion, Vol. 1, No. 1 (Jan. 1984): pp. 17-38.

[5] LEE J. D. et al., TIBER II/ETR Final Design Report, Vol. 3 (Sept. 1987).

[6] *A Demonstration Tokamak Power Plant Study*, Argonne National Laboratory ANL/FPP/82-1 (Sept. 1982).

[7] ABDOU M. et al., *Blanket Comparison and Selection Study*, Argonne National Laboratory Report ANL/FPP-83-1 (Oct. 1983).

[8] *Proceedings of the Magnetic Fusion Energy Blanket and Shield Workshop*, ERDA-76/117/2 Conf.-760343, Vol. 1-2, (August 1975).

[9] GREINER L., *Selection of High Performing Propellants for Torpedoes*, ARS Journal,30 (1960): p. 1161.

[10] WHITE W.D., *Lithium and Sodium for Underwater Propulsion*, Astronautics, 6(April 1961): p. 38.

[11] EL-GENK S. M., HOOVER M. D., Space Nuclear Power Systems, Vol. 2, Orbit Book Co. (1985).

[12] JEPPSON D. W. et al., *Lithium Literature Review: Lithium's Properties and Interactions*, Hanford Engineering Development Laboratory Report HEDL-TME 78-15 UC-20 (April 1978).

[13] MARKOWITZ M. M., *Alkali Metal-Water Reactions*, Journal of Chemical Education, Vol 40,No. 12. (Dec 1963): pp. 633-6.

[14] EPSTEIN L. F., *Recent Developments in the study of Metal-Water Reactions*, Progress in Nuclear Energy, 4th Ser. 4 (1961): p. 462.

[15] LONG C., *Explosions of Molten Aluminum in Water: Cause and Prevention*, Metal Progress, 71, pp. 107-112 (1957).

[16] CORRADINI M. L., KIM B. J., OH M. D., *Vapor Explosions in Light Water Reactors: a Review of Theory and Modeling*, Progress in Nuclear Energy, Vol. 22 No. 1 (1988): pp. 1-117.

[17] BLINK J. A., HOFFMAN N. J., *Lithium Safety Considerations*, 1981 Laser Program Annual Report, Lawrence Livermore National Laboratory Report UCRL-50021-81 (August 1981).

[18] HERZOG J. P., *Lithium-Lead/Water Reaction Experiments and Analysis*, PhD Thesis, University of Wisconsin - Madison, (1987): pp. 35-6.

[19] FINN P. A. et al., *The Reactions of Li-Pb Alloys with Water*, Transactions of the American Nuclear Society, 34, (1984): p. 55.

[20] ARMSTRONG D. R., Private Communication (1988).

[21] JEPPSON D. W., KEOUGH R. F., *Fusion Reactor Blanket and Coolant Material Compatibility*, Proceedings of the Second Topical Meeting on Fusion Reactor Materials, Seattle, Washington (August 9-12, 1981).

[22] JEPPSON D. W., MUHLESTEIN L. D., *Some Safety Considerations of Liquid Lithium as a Fusion Breeder Material*, Fusion Technology, Vol. 10 (Nov. 1986): pp. 1211-15.

[23] BARNETT D. S., GIL T. K., KAZIMI M. S., *Lithium-Mixed Gas Reactions*, Fusion Technology, Vol. 15, No. 2 (March 1989): pp. 967-72.

[24] HERZOG J. P., CORRADINI M. L., *Lithium-Lead/Water Reaction Experiments and Analysis*, Fusion Technology, Vol. 15, No. 2 (March 1989): pp. 979-83.

[25] LOMPERSKI S. W., Nuclear Engineering and Engineering Physics Department, University of Wisconsin, EG&G Fusion Safety Annual Report, (1988).

[26] DEAL B. E., SVEC H. J., *Metal-Water Reactions. II. Kinetics of the Reaction Between Lithium and Water Vapor*, Journal of the American Chemical Society 75, (Dec. 20, 1953): pp. 6173-75.

[27] IRVINE W. R., LUND J. A., *The Reaction of Lithium With Water Vapor*, Journal of the Electrochemical Society, 110, No. 2 (Feb. 1963): pp. 141-44.

[28] NEWMAN R. N., PUGH A. R., SMITH C. A., *Explosive Interaction Between Sodium and Water, and Material Wastage in the Vicinity of leaks in Sodium Water Heat Exchangers*, Liquid Alkali Metals, The British Nuclear Energy Society, London England (1973): pp. 85-91.

[29] BOARD, S. J., FARMER, C. L., POOLE, D. H., *Fragmentation in Thermal Explosions*, CEGB Report RD/B/N2423 (1972).

[30] KIM B., CORRADINI M. L., *Modelling of Small-Scale Single Droplet Fuel/Coolant Interactions*, Nuclear Science and Engineering 98, (1988):pp.16-28.

[31] NEWMAN R. N., PUGH A. R., SMITH C. A., *On Sodium/Water Reactions*, Journal of the British Nuclear Energy Society, No. 12 (1973): pp. 261-3.

[32] NEWMAN R. N., SMITH C. A., *Sodium/Water Combustion and the Chemistry of Wastage at Sodium/Water Leak Sites*, Journal of Nuclear Materials 52 (1974): pp. 173-83.

[33] ASHWORTH A. B., et al., *Novel Study of the Reactions of Molten Sodium-Potassium and Sodium With Water*, Liquid Metal Engineering and Technology, British Nuclear Engineering and Science, (1984) pp. 1-6.

[34] BAKER L., JUST L. C., *Studies of Metal-Water Reactions at High Temperatures: III Experimental and Theoretical Studies of the Zirconium-Water Reaction*, Argonne National Laboratory Report ANL-6548 (May 1962).

[35] BRADLEY R. H., WITTE L. C., COX J. E., *The Vapor Explosion- Heat Transfer and Fragmentation; V. Investigation of the Vapor Explosion Phenomenon using a Molten-Metal Jet Injected Into Distilled Water*, University of Houston Dept. of Mech. Engr. Technical Report ORO-3936-7, (October 1971).

[36] WITTE L. C., et al., *The Vapor Explosion- Heat Transfer and Fragmentation; IV. Rapid Quenching of Molten Metal*, University of Houston Dept. of Mech. Engr. Technical Report ORO-3936-6, (August 1971).

[37] MEYERS G.E., Analytical Methods in Conduction Heat Transfer, Genium Publishing Corp., Schenectady, NY (1987).

[38] OMEGA Complete Temperature Measurement Handbook and Encyclopedia, Vol. 27, OMEGA Engineering Inc., Stamford, CT (1989).

[39] BINEY P.O., et al, *Mass Transfer Modelling of Liquid Metal/Water Interactions*, Proceedings of the Ninth Topical Meeting on the Technology of Fusion Energy, October 1990, Oak Brook, IL.

[40] OHSE R.W., Handbook of Thermodynamic Properties of Alkali Metals, Blackwell Scientific Publications, Oxford (1985).

[41] BIRD B.R., STEWART W.E., LIGHTFOOT E.N., Transport Phenomena, John Wiley & Sons, New York, NY (1960).

[42] WASHBURN E.W., International Critical Tables of Numerical Data, Physics, Chemistry and Technology, Volume 5, McGraw-Hill Inc. New York, NY (1929)

[43] DHIR V.K., PUROHIT G. P., *Subcooled Film-Boiling Heat Transfer From Spheres*, Nuclear Engineering and Design, 47 (1978) pp. 49-66.

[44] COLLIER J.G., Convective Boiling and Heat Transfer, McGraw-Hill Inc., United Kingdom (1981).

[45] DREW D. A., *Analysis of the Natural Initiation of Vapor Explosions*, Sandia National Laboratory Report SAND84-1732 (Oct. 1984).

[46] OCHIAI M., BANKOFF S. G., *Liquid-Liquid Contact in Vapor Explosions*, Proceedings of the International Meeting on Fast Reactor Safety, (USERDA) Conf. No. 7610001 pp. 1843-51 (Oct. 5, 1976).

[47] SIEGEL R., HOWELL, J.R., Thermal Radiation Heat Transfer, McGraw-Hill Inc., New York, NY (1981).

[48] MARK H. F., et al., Encyclopedia of Polymer Science and Engineering, Vol. 10, John Wiley & Sons, New York, NY (1987).

[49] SHVAREV K. M., BAUM B. A., *Estimation of Radiative Characteristics of Metals in the Framework of Classical Electronic Theory*, Soviet Physics Journal, Vol. 21, pp. 1-4 (1978).

[50] YAN JINGDE, *Analyses and In-Cylinder Measurements of Local and Hemispherical Particulate Radiant Emissions and Temperatures in a Direct Injection Diesel Engine*, PhD Thesis, University of Wisconsin-Madison, (1988).

[51] YOUNG H. D., Statistical Treatment of Experimental Data, McGraw-Hill Inc., New York, NY (1962).

[52] CURCIO J. A., PETTY C. C., *The Near Infrared Absorption Spectrum of Liquid Water*, Journal of the Optical Society of America, Vol. 41, No. 5 (May, 1951).

[53] HALE G. M., QUERRY M. R., *Optical Constants of Water in the 200-nm to 200 um Wavelength Region*, Applied Optics, Vol. 12, No. 3 (March 1973).

[54] Publishers' VGA, Willow Peripherals Inc., 190 Willow Avenue, Bronx, NY 10454 (1988).

[55] Publisher's Paintbrush, ZSoft Corp., 450 Franklin Road, Suite 100, Marietta, GA 30067 (1987).

[56] CASAS J.C., *Investigation of the Mixing Zone Between Two Immiscible Liquids in a Pool Configuration due to an Upward Gas Flow*, PhD Thesis, University of Wisconsin - Madison, (1990): Appendix D.

[57] CLIFT R., GRACE J. R., WEBER M. E., Bubbles, Drops, and Particles, Academic Press, Inc., New York, NY (1978): pp. 23-29.

[58] TOULOUKIAN Y.S., et al., Thermophysical Properties of Matter , Volumes 3,9, and 11, Plenum Publishing Corp., New York, NY (1970).

[59] DIXON, J., *Radiation Thermometry*, Journal of Physics E: Scientific Instruments 21 pp.425-36 (1988).

[60] DeWITT D. P., NUTTER G. D., Theory and Practice of Radiation Thermometry, John Wiley & Sons, Inc., New York, NY (1988).